FORMATION AND DEVELOPMENT OF TROPICAL TEMPERATE TROUGHS ACROSS SOUTHERN AFRICA AS SIMULATED BY A STATE-OF-THE-ART COUPLED MODEL

by

Magdel Erasmus

A Thesis Submitted in Partial Fulfilment of the Requirements for the Degree of Magister Scientiae (Meteorology)

DEPARTMENT OF GEOGRAPHY, GEOINFORMATICS AND METEOROLOGY
FACULTY OF NATURAL AND AGRICULTURAL SCIENCES
UNIVERSITY OF PRETORIA
SOUTH AFRICA

UNIVERSITEIT VAN PRETORIA
UNIVERSITY OF PRETORIA
YUNIBESITHI YA PRETORIA

November 2019

If you can dream it, you can do it.

– Walt Disney

Success is not final; failure is not fatal: it is the courage to continue that counts.

– Winston S. Churchill

Declaration

This is to declare that this thesis, which I submit for the degree MSc in Meteorology at the University of Pretoria, is my own work, unless or otherwise explicitly acknowledged by citation of published and unpublished sources. This research has not previously been submitted for a degree at this or any other tertiary institution.

Magdel Erasmus (04415132)

SIGNATURE: .....

DATE: 06-12-2019

Supervisor

Prof. W.A. Landman
Department of Geography, Geoinformatics and Meteorology, University of Pretoria, Lynnwood Road, Pretoria 0002, South Africa

Co-supervisor

Dr. C.J. Engelbrecht
Long-range forecasting unit, South African Weather Service, Eco-Park Estate, Eco Glades 1 Block B, Highveld, Centurion, South Africa

Acknowledgements

This project was an amazing journey and it would not have been possible without the support and assistance of a few people. Many thanks and appreciation for the following persons and entities:

- Prof. W.A. Landman (University of Pretoria) for guiding me and giving the necessary direction
- Dr. C.J. Engelbrecht for getting the data in a workable format and for her assistance, especially towards the end of this journey
- The UK Met Office for providing the GloSea5 model data
- Dr. N. Hart for supplying his Meteorological Robot (MetBot)
- Bernard for his patience, support and guidance, as well as his assistance with Python in order to be able to use the MetBot

Contents

Declaration i
Supervisor iii
Co-supervisor iii
Acknowledgements iii
List of Abbreviations and Acronyms viii
PREFACE x
CHAPTER 1: Introduction 1
1.1 Tropical Temperate Troughs 1
1.1.1. General structure of a TTT 2
1.1.2. Location of TTTs 2
1.1.3. Development of TTT events over southern Africa 4
1.1.4. Effects of TTT events on southern Africa 5
1.1.5. Relation between TTT events and planetary (Rossby) waves 6
1.1.6. Relation of TTT events with SSTs around southern Africa 7
1.1.7. Changes in the intertropical convergence zone before, during and after a TTT 8
1.1.8. Correlation of TTTs with ENSO 9
1.1.9. Statistical Analysis in previous studies on TTT events 10
1.1.10. Case studies on TTT events 10
1.1.11. Importance of modelling and understanding TTT events 11
1.2 Numerical Meteorological Models 12
1.2.1 History of Numerical Weather Prediction 12
1.2.2 Current Models 13
1.3 Study description 15
1.3.1 The need to investigate TTT events 15
1.3.2 The benefits to investigate TTT events 15
1.3.3 Research problem 15
1.3.4 Research Question and Objectives 16
1.3.5 Challenges and limitations 16
1.4 Thesis Layout 16
CHAPTER 2: Methodology 18
2.1 Introduction 18
2.2 Identification of TTT events 18
2.3 The GloSea5 model 19

2.3.1 Resolution of the GloSea5 20
2.3.2 Configuration of the GloSea5 20
2.3.3 Initialization 21
2.3.4 Ensemble prediction system 21
2.3.5 Performance of the GloSea5 22
2.4 The OLR-data 22
2.4.1 OLR 22
2.4.2 Observed data 25
2.4.3 Model data 26
2.5 The Geographical Domain 27
2.6 The MetBot 28
2.7 Attending to the research question and the research objectives 29
2.8 Model evaluation procedure 30
2.8.1 Number of candidate cloud bands and percentage deviation 31
2.8.2 Root Mean Square Error 31
2.8.3 Percentage error 32
2.8.4 Bias-adjustment 32
2.9 Synopsis 33
CHAPTER 3: Introduction to the Results 34
3.1 General guidelines for the results chapters to follow 34
3.2 MetBot results 35
3.3 Synopsis 36
CHAPTER 4: Frequency of TTTs 37
4.1 Total and average number of cloud bands 37
4.2 Percentage deviation 41
4.3 Root-Mean-Square-Error 44
4.4 Synopsis 46
CHAPTER 5: Intensity of TTTs 47
5.1 Area 47
5.1.1 Average area 47
5.1.2 Root-mean square error 53
5.2 Outgoing longwave radiation 57
5.2.1 Minimum OLR 58
5.2.2 Maximum OLR 65
5.3 Synopsis 71
CHAPTER 6: Location of TTTs 72

6.1 Cloud band anchor point 72
6.2 Position of the centroid 80
6.3 Tilt 84
6.3.1 Negative tilts only 86
6.3.2 Positive and negative tilts combined 90
6.4 Synopsis 92
CHAPTER 7: Discussion 94
7.1 Identifying modelled cloud bands 95
7.2 Frequency of the modelled cloud bands 95
7.3 Intensity of the modelled cloud bands 97
7.3.1 Area 97
7.3.2 Outgoing Longwave Radiation 98
7.4 Location of TTT events 101
7.4.1 Anchor points of the cloud bands 101
7.4.2 Position of the centroid 102
7.4.3 Tilt of the cloud bands 104
7.5 The Ensemble Members 106
7.6 The Model 107
7.6.1 The model: Frequency of TTT events 109
7.6.2 The model: Intensity of TTT events 109
7.6.3 The model: Location of TTT events 111
7.6.4 The model: a short summary 112
7.7 ENSO and modelled TTT events 112
CHAPTER 8: Conclusion and Future Work 117
Future work 118
Final remarks 120
REFERENCES 121
APPENDIX A: Average area of the modelled cloud bands 125
APPENDIX B: Anchor points and centroids of the cloud bands 133

List of Abbreviations and Acronyms

AGCM	Atmosphere-only General Circulation Model
CC	Candidate Cloud Band/Cloud Band
CGCM	Coupled Ocean-atmosphere General Circulation Model
CICE	Los Alamos Sea-Ice Model
ECMWF	European Centre for Medium-Range Weather Forecasts
EM	Ensemble Member
ENSO	El Niño Southern Oscillation
ESKOM	Electricity Supply Commission of South Africa
GCM	General Circulation Model
GloSea5	Global Seasonal Forecasting System version 5
HadGEM3	Hadley Centre Global Environmental Model version 3
ITCZ	Intertropical Convergence Zone
JNWPU	Joint Numerical Weather Prediction Unit
JULES	Joint UK Land Environmental Simulator
MAE	Mean Absolute Error
MBE	Mean Bias Error
MetBot	Meteorological Robot
MSE	Mean Square Error
NASA	National Astronomical and Space Association
NE	Northeast
NEMO	Nucleus for European Modelling of the Ocean
NESDIS	National Environmental Satellite Data and Information Service
NOAA	National Oceanic and Atmospheric Administration
NW	Northwest
NWP	Numerical Weather Prediction
Obs	Observations/Observational data
OLR	Outgoing Longwave Radiation
PD	Percentage Deviation
PE	Percentage Error
RMSE	Root Mean Square Error
SE	Southeast
SST	Sea Surface Temperature
SW	Southwest
TTT	Tropical Temperate Troughs

For the abbreviations used for the different ensemble members, please refer to table 3.1.

PREFACE

A short background and introduction

Weather and the study thereof (Meteorology) have been a part of the everyday human life for a very long time, and as is the case with many different scientific fields that intrigue us, we constantly strive to advance in what is already known by improving the technology or by developing a new theory. In Meteorology we continuously strive to refine forecasts of atmospheric behaviour. To accomplish the latter, we develop enhanced numerical models to create these forecasts.

In any situation where you want to improve something, you need to test the outcome of a new "experiment". That is the case with this study on Tropical Temperate Troughs (TTTs): to test the ability of a state-of-the-art seasonal forecast model to predict these weather phenomena on a seasonal timescale. This study therefore forms part of the development of the field of meteorology, because it focusses on the predictability of a specific weather phenomenon, namely TTT events over southern Africa. This study is also a novelty, as it is the first time that the predictability of these tropical-extratropical interactions is investigated on a seasonal timescale.

In this study these TTT events are investigated using a state-of-the-art ensemble prediction system, the Global Seasonal Forecasting System version 5 (GloSea5) of the UK Met Office. The UK Met Office bought their first computer in 1959, which was able to do 30000 calculations per second (UK Met Office, 2012). Since then the weather models of the UK Met Office have improved significantly (as has any other weather model of other meteorological institutions). Nowadays, they use various ensemble predicting systems to produce extremely detailed short-range forecasts, as well as complicated seasonal and climatological (long-range) forecasts.

More on TTT events and this study

A TTT is a type of weather system that links the tropics and the extra-tropics across southern Africa. TTT events have been studied statistically quite comprehensively, in particular with reference to the frequency of occurrence during the austral summer season and its contribution to rainfall. However, whether these rain-producing weather systems can be captured and predicted has not received much attention. This study focuses on the predictability of the characteristics of TTTs across southern Africa on a seasonal timescale, by using the GloSea5 seasonal forecasting model developed by the UK Met Office. Gridded hindcast data for the months of November, December, January and February from 1996/1997 to 2009/2010 are compared to observed data. The different ensemble members of the GloSea5 model (with lead-times of 1 week up to 2 months) are first compared separately to the observed

data, after which the model average, with a 0-month, a 1-month and a 2-month lead-time, is calculated and also compared to the observed dataset.

TTT events have distinctive characteristics during the formation and the development phases. Most prominent of these characteristics are the cloud bands associated with these weather systems, which have in most cases a north-west to south-east orientation and move from west to east across southern Africa. To identify the TTTs, daily outgoing long-wave radiation values are processed by a Meteorological Robot (MetBot), with a strict criterion to identify the cloud bands that characterise these weather systems. The MetBot's algorithm produces the information needed to further investigate the different characteristics of TTTs, such as the frequency, the location and the intensity thereof. Analysis of the MetBot output includes calculating the Root Mean Square Error, the percentage error and in some cases the percentage deviation of the different characteristics, namely the number of cloud bands, as well as the anchor point, the centroid position, the area, the tilt and the minimum and maximum OLR values of the cloud bands.

The outcome

This investigation revealed that the characteristics of TTT events can to some extent be predicted on a seasonal timescale for the summer rainfall season of southern Africa. The model used in this study fared particularly well with a 1-month lead-time forecast (compared to a 0-month and a 2-month lead-time forecast). The intensity and the location of the cloud bands associated with TTT events are forecast with a smaller percentage error than the frequency of these systems, as the frequency of TTTs tend to be significantly under-predicted by the model. For some predicted quantities, such as the area of the cloud bands, a bias-adjustment is necessary which produces significantly better results with smaller percentage errors. In the conclusions, suggestions are made on possible future studies, and how to develop this study further to create seasonal forecasts with higher skill, with special regard to TTT events.

Part of the research done in this study was already presented at the annual conference of the South African Society for Atmospheric Sciences (SASAS) in 2016. One of the characteristics of TTT events, namely the frequency of TTT events during the summer rainfall season, was discussed during a presentation. This part of the research was also included in the Conference Proceedings, which can be found via the website of SASAS (www.sasas.org).

The layout

This thesis is compiled as follows: First an introductory chapter will explain what a TTT event is, what the characteristics of such an event are and why it is important to gain a better understanding of these events. Information will also be given on previous studies on TTT events. The reader will also find in

this chapter a motivation as to why the GloSea5 model was chosen and the reasoning behind choosing the specific geographical domain. A chapter on the methodology of the study follows thereafter, in which the reader will be informed about the procedure that is followed to identify a TTT event, which variables are focused on in this study and why these variables are chosen. A brief description of the software used in this study is given, as well as a description of the data and the observations. Chapter three to six show the results obtained in this study. It focuses on the modelled TTT events and how these events correlate with the observed TTT events. Each of these result-chapters considers the different objectives and subobjectives separately. Hereafter follows an in-depth discussion of the results in chapter seven and lastly, chapter eight will give concluding remarks and what future work may entail. After the final chapter on this study, the references used during this study can be found, as well as an appendix with some of the figures of each ensemble member not included within the different results chapters.

The author of this dissertation sincerely hopes that the reader finds this study on TTT events intriguing and enjoyable.

CHAPTER 1: Introduction

1.1 Tropical Temperate Troughs

In various parts of the world, there exist a significant type of weather system that creates a link between the tropics and the extratropics (Harangoza & Harrison, 1983; Streten, 1973). This type of weather system is associated with tropical-extratropical interactions, and can be referred to as tropical plumes (Hart et al, 2010; Knippertz, 2007). In southern Africa, however these systems are known as Tropical Temperate Troughs (TTTs) (Harrison, 1984; Hart et al, 2010) and hereafter these tropical-extratropical interactions will be referred to as such. TTTs represent an important mechanism for the poleward transportation of energy (heat), moisture and momentum, and consist of an area of enhanced convergence that can normally be identified by cloud bands (Harrison, 1984; Hart et al, 2010; Macron et al, 2014; Ratna et al, 2013; Todd and Washington, 1999; Todd et al, 2004; Vigaud et al, 2012; Washington and Todd, 1999). These cloud bands can be recognized on satellite imagery as regions of elongated bands of clouds, stretching from the tropics south-eastward (north-eastward) towards the South Pole (North Pole) (Hart et al, 2010; Harangozo and Harrison, 1983; Macron et al, 2014) (Fig. 1.1).

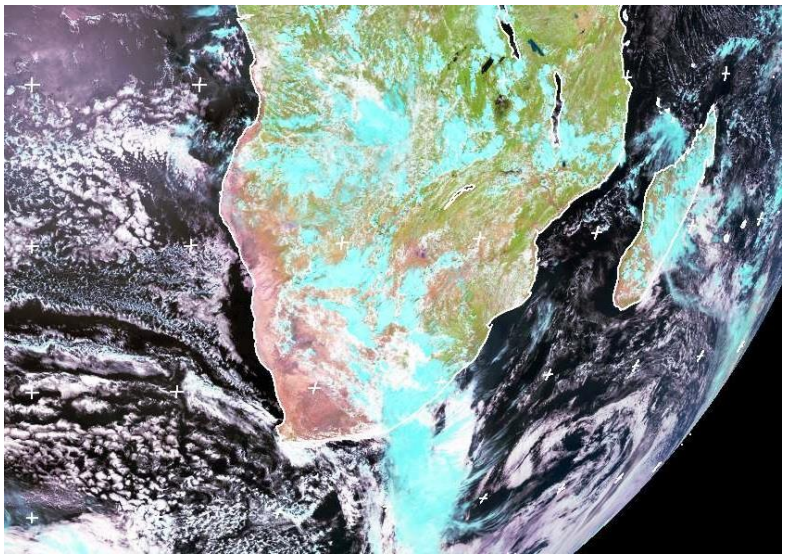

Figure 1.1: A satellite image showing a typical TTT cloud band across southern Africa. This image was taken at 12:00 UTC 19 January 2010 (*Meteosat SEVIRI RGB composite 3,2,1; Courtesy:* NERC Satellite Receiving Station, Dundee University, Scotland, http://www.sat.dundee.ac.uk/*)*

TTTs usually last several days and can be tracked on satellite imagery as the associated cloud bands move eastwards. Due to their longevity, these systems usually produce large amounts of rainfall and can contribute greatly towards a season's accumulative rainfall. These systems are one of the major contributors to summer rainfall over southern Africa (Harrison, 1984). In the summer rainfall region even up to 39% of the mean annual rainfall could be attributed to TTT events (Crimp et al, 1997). Although the physical and dynamic characteristics of these systems are not fully understood at the synoptic scale (Hart et al, 2010; Ratna et al, 2013; Vigaud et al, 2012), a substantial amount of work has been done describing these significant rain-producing systems.

1.1.1. General structure of a TTT

TTTs are characterised by a cloud band stretching from the tropics to the mid-latitudes (Harrison, 1984), indicating an area of enhanced convection. On either side of the cloud band there are areas of suppressed convection (Macron et al, 2014), forming a ridge-trough-ridge-like synoptic pattern (Ratna et al, 2013), that can contribute to focus the inflow of moisture into the TTT (e.g. Lindesay and Jury, 1991). These ridge-trough-ridge patterns can either form over a landmass or over the ocean. Normally a TTT forming over the ocean only exhibits mid- to upper-level clouds through the subtropics, but when a TTT forms over a landmass, for example southern Africa, deep convection and heavy rainfall can be supported by continental heating (Hart et al, 2010). Another difference is that when a TTT forms over a landmass, it usually produces heavy rainfall along the full length of the TTT, whereas it is not necessarily the case for a TTT forming over the ocean (Hart et al, 2010).

Adiabatic temperature advection, positive vorticity advection and land-based convection play an important role in producing uplift in TTTs (Hart et al, 2010). Adiabatic temperature advection is usually stronger in the lower troposphere, while positive vorticity advection primarily occurs in the upper-tropospheric troughs in a quasi-geostrophic context (Hart et al, 2010). It was also found that local land-based convection is especially important in the subtropical section of the cloud band (Hart et al, 2010).

1.1.2. Location of TTTs

TTTs can occur in the Northern and the Southern Hemisphere, as they are occurrences where tropical moist air stretches either northwards or southwards respectively. These types of weather phenomena have been studied for both hemispheres; one such example was done on

the Northern Hemisphere Atlantic Ocean (Knippertz, 2005). A few factors were found that can possibly explain why the three areas (the east and central Pacific Ocean and the northern Atlantic Ocean) are preferred locations for tropical plume development, namely: wave disturbances are generated by the cool-season semi-permanent baroclinic zones along the continents to the northwest, which eventually penetrate into the tropics at the eastern ends of the basins; and convergent forcing situations can sometimes be produced by upper-level ridges, forced by the maxima of tropical convection over the western Pacific, as well as the Amazon basin (Knippertz, 2005). An important difference was found between tropical plumes developing over the Pacific Ocean basin and the Atlantic Ocean basin: a deeper layer of tropical moisture over the African continent have an effect on the precipitation under the extratropical end of the tropical plume (Knippertz et al, 2003; Knippertz, 2005). It was also found that sometimes tropical plumes do not show the typical slow evolution, east-west orientation and predominant cloud generation (Knippertz, 2005).

In the Southern Hemisphere, TTT events can form in three possible locations of which the southern Africa-southwest Indian Ocean region is one of the preferred regions (Fauchereau et al, 2009; Pohl et al, 2009; Ratna et al, 2013; Vigaud et al, 2012). So far most previous studies that focused on TTTs over the southern African region were based on statistical analysis (Fauchereau et al, 2009; Harrison, 1984; Todd and Washington, 1999; Todd et al, 2004) and therefore did not capture any connections between the local rain-producing systems and large-scale tropical-temperate atmospheric interactions over southern Africa (Vigaud et al, 2012). Later studies focused more on a simulation approach towards TTT prediction (Fauchereau et al, 2009; Vigaud et al, 2012).

Three preferred regimes where TTTs tend to develop across southern Africa were discovered (Fauchereau et al, 2009), which was confirmed by a later study (Vigaud et al, 2012). These three regimes are bands of maximum convection that are rooted over the north-eastern parts of South Africa, Mozambique and Madagascar, stretching in a NW/SE direction and ends at longitudes between 40°E and 65°E (Fauchereau et al, 2009). A precursory signal of simulated zonal stretching deformation at about 5 days prior to a TTT event at the 200hPa level was also discovered (Vigaud et al, 2012). This suggests that the mid-latitude westerly waves play an important role and especially their phasing during a TTT event (Vigaud et al, 2012). The area where TTTs develop most often lies in the southwest Indian Ocean and this is also where these

weather phenomena develop the strongest (Cook, 2000; Hart et al, 2010; Todd and Washington, 1999).

1.1.3. Development of TTT events over southern Africa

Several atmospheric circulation features of the southern African summer season play an important role in TTT formation and development over the region (Hart et al, 2010). Upper westerly waves are important for TTT formation over southern Africa (Harangoza and Harrison, 1983) and play a role in the southward moisture transport (Todd et al, 2004). Other atmospheric features which play a role in the development of TTT events include the Angola Low, a surface high over southern Mozambique and the south-western Indian Ocean, continental heat lows over the central Kalahari Desert, the South Atlantic High and the South Indian High (Hart et al, 2010; Macron et al, 2014) (Fig. 1.2).

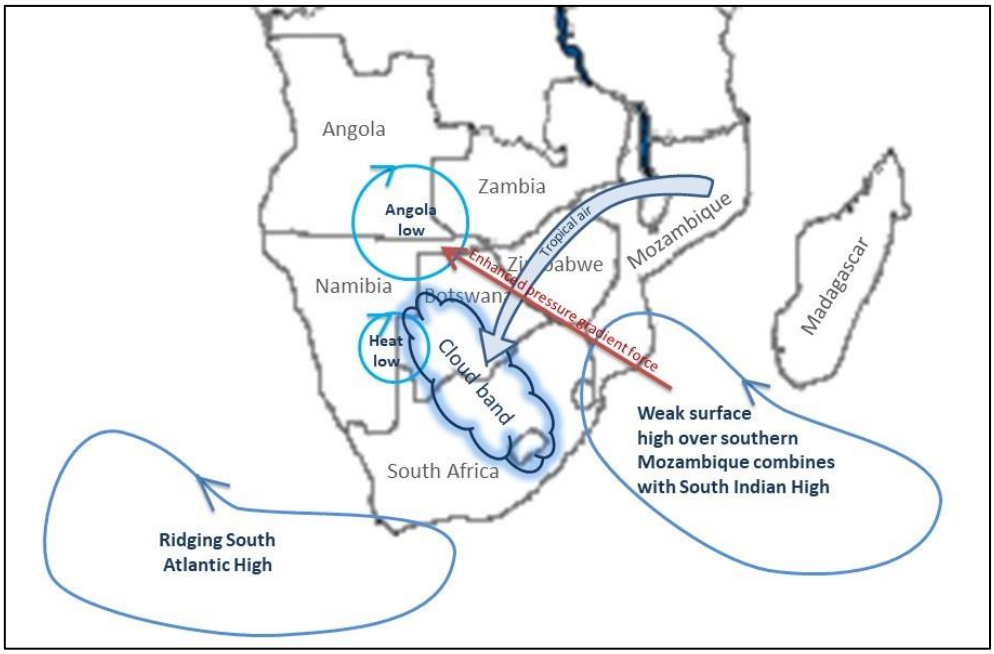

Figure 1.2: A schematic illustration of the various atmospheric circulation features playing a role during the development of TTTs across southern Africa. The red arrow indicates the enhanced pressure gradient force between the weak surface high over southern Mozambique and the low pressure above Angola (the Angola Low), and the blue arrow indicates the influx of tropical moist air.

When a weak surface high-pressure develops over southern Mozambique and the adjacent ocean, it enhances the pressure gradient across Botswana and Zimbabwe towards the semi-permanent Angola Low (Hart et al, 2010). A greater pressure gradient leads to stronger low-

level north-easterly flow across the central parts, bringing tropical air north of Madagascar towards central southern Africa (Hart et al, 2010; Reason et al, 2006; Todd and Washington, 1999). When a continental heat low forms over the Kalahari Desert, a weak cyclonic circulation is induced, diverting the low-level north-easterlies further south (Hart et al, 2010).

The scenario for TTT development is further established by the ridging of the South Atlantic High-pressure system to the east of South Africa, which induces onshore flow and therefore also possible coastal showers (Hart et al, 2010; Ratna et al, 2013). When the South Indian High extends north-westward and combines with a surface high over Mozambique and the adjacent ocean, an easterly wave is established over Mozambique and eastern South Africa (Hart et al, 2010; Ratna et al, 2013). According to Manhique et al (2011) the strengthening of the South Indian High and the shifting thereof to the northwest are important mechanisms for generating TTT events.

The combination of these atmospheric circulation features may then lead to the development of a TTT across southern Africa (Hart et al, 2010), which propagates eastward towards Mozambique and Madagascar (Fauchereau et al, 2009; Ratna et al, 2013). This propagation causes moisture to be transported off the continent along the cloud band, rising from around 800hPa over the continent to the mid-atmosphere (700-650hPa) in the mid-latitudes, during the mature stages of the TTT (D'Aberton and Tyson, 1996; Ratna et al, 2013; Todd et al, 2004). A TTT developing under these atmospheric circumstances will typically extend from the Angola Low, south-eastwards to an area in the southern Indian Ocean, just east of the ridging South Atlantic High (Hart et al, 2010).

1.1.4. Effects of TTT events on southern Africa

Due to the geographic location of southern Africa, the weather and climate are mostly affected by tropical and mid-latitudinal weather systems and dynamics (Vigaud et al, 2012). Therefore, rainfall normally occurs during late spring and the summer months (November to February), except for the south-western coast of South Africa to the Namib Desert where rainfall occurs during winter. Part of the south coast and southeast coast of South Africa fall within both rainfall regions and receive therefore rain all-year-round. Winter rainfall is driven by the passing of frontal systems, while summer rainfall is more of tropical origin. Especially during the summer months, frontal systems can link up with a tropical system, which in general leads to a TTT event.

Subsequent analysis suggested that the mean frequency of the cloud bands moving across South Africa during the summer months is once every seven days, due to the occurrence of TTT events and the passing of a surface cold front (Harrison, 1984). TTT events have a great influence on rainfall over specific regions, but across southern Africa it specifically plays a significant role during the summer rainfall season (November to February) (Harrison, 1984; Hart et al, 2010; Ratna et al, 2013; Vigaud et al, 2012). Normally heavy rainfall is associated with TTT events (Harrison, 1984; Macron et al, 2014; Ratna et al, 2013) and it can therefore cause major flooding, especially in cases where a TTT and a cut-off low occur at the same time. Such was the case during the extreme rainfall event of 16-22 April 2006 across the southern Namib Desert when an anomalously northward located cut-off low occurred in combination with an anomalously westward located TTT (Muller et al, 2007). During this period, Lüderitz (a coastal town in Namibia) received a record-breaking 101.8mm of rain, compared to the long-term annual average rainfall of only 16.7mm (Muller et al, 2007).

In addition, it is also possible for phenomena such as mesoscale convective systems to be embedded within the cloud bands associated with TTTs (Hart et al, 2010; Blamey and Reason, 2009). A study of the 12-14 February 1996 rainfall event found that during the first 24-hours of rainfall a mesoscale convective system developed, bringing nocturnal convective activity which died out during the daytime (De Coning et al, 1998). It appeared that this mesoscale convective system was part of a larger scale subtropical trough, which moved slowly eastward (De Coning et al, 1998).

Recent studies suggest that there is a relation between the rainfall inter-annual variability over southern Africa and the frequency, position and intensity of weather events like TTTs (Ratna et al, 2013). For the wet spell of 1 - 7 January 1998, two consecutive TTTs contributed more than 40% of the summer rainfall of South Africa for that specific season (Hart et al, 2010; Ratna et al, 2013).

1.1.5. Relation between TTT events and planetary (Rossby) waves

Planetary or Rossby waves play an important role in large-scale meteorological processes (Holton & Hakim, 2013). It can in general be defined as a potential vorticity-conserving motion that exists because of the gradient of potential vorticity in a baroclinic atmosphere (Holton & Hakim, 2013).

TTT events are closely related to mid-latitude perturbations (Rossby waves), for instance the Rossby waves and the eastward propagation of the TTT events are in phase (Hart et al, 2010; Macron et al, 2014; Ratna et al, 2013; Vigaud et al, 2012). It was found that 41% of mid-latitude perturbations can be associated with a TTT (Macron et al, 2014). In another study, mid-latitude perturbations were associated with significant anomalies of uplift over southern Africa and it was found that abnormally strong Rossby waves, which favour large-scale atmospheric instability over southern Africa, were a necessary condition for the development of TTTs (Vigaud et al, 2012; Macron et al, 2014). It was also shown that Southern Hemisphere planetary waves play an important role in the inter-annual variability of TTT events (Manhique et al, 2011). Another necessary condition is positive latent energy anomalies over the Agulhas Current, for the supply of lower-layer moisture, which in combination with the Rossby wave, can form favourable conditions for atmospheric convection development (Macron et al, 2014).

Rainfall across South America is linked to that across southern Africa by Atlantic moisture fluxes that are embedded in a large-scale circulation pattern, however these teleconnections are not yet fully understood (Grimm & Reason, 2011, Macron et al, 2014). The fact that these moisture fluxes occur about two to three days prior to TTTs can play an important role in the real-time prediction of these systems (Macron et al, 2014). According to another study, a surface low initiated the transport of tropical moisture poleward, because of a low potential vorticity trough across southern Africa that developed due to anti-cyclonic wave breaking a few days before a TTT occurred (Hart et al, 2010). It was further stated that as soon as the leading edge of this low potential vorticity trough neared the western regions, convection and cloud band formation are triggered (Hart et al, 2010). This effect is supported by upstream deformation as low potential vorticity air is advected poleward and by baroclinic wave growth near the subcontinent (Hart et al, 2010).

1.1.6. **Relation of TTT events with SSTs around southern Africa**

Previous studies found that sea-surface temperatures (SST) off the southern African coasts can also play a role in the development and frequency of TTT events (Crimp et al, 1998, Macron et al, 2014, Manhique et al, 2011 and Ratna et al, 2013). The forcing of low-level pressure anomalies in the Mascarene area (the region around the islands of Mauritius, Réunion and Rodriques) was found to contribute to the increased frequency of TTT events over southern Africa (Manhique et al, 2011). Cool SST to the east of Madagascar, along with large-scale

planetary waves play an important role in the development of these low-level pressure anomalies (Manhique et al, 2011).

It was found that the occurrences and/or persistence of TTT events are increased by moisture fluxes associated with warm temperature anomalies over the Agulhas Current, south of Madagascar (Macron et al, 2014; Manhique et al, 2011; Vigaud et al, 2012; Williams et al, 2007). At a few days' lead, continental TTTs are characterised by a significant warming in the Agulhas Current region (Vigaud et al, 2012). This warming in association with latent heat-release supports increased baroclinic instabilities and therefore also local enhanced convection (Vigaud et al, 2012). Low-level humidity convergence was favoured by increased moisture advection from the Agulhas Current region onto the adjacent continent, which further contributed to the persistence of TTT events (Vigaud et al, 2012).

The main source of moisture for the development of a TTT comes from the Indian Ocean, because of the easterly winds that pushes the moisture across southern Africa (Ratna et al, 2013). This is due to anomalously warm SST close to the African coast in the Indian Ocean (Ratna et al, 2013). It was suggested by previous studies that there is a relationship between a TTT that develops over the Mozambique Channel and the positive phase of the subtropical Indian Ocean dipole (Fauchereau et al, 2009; Macron et al, 2014).

During a case study, it was found that the general formation and dissipation of the TTT event of 21-24 January 1981 was not affected by anomalous SST in the Agulhas Current retroflection region, however it showed significant increases in convective precipitation (Crimp et al, 1998). These precipitation increases can be ascribed to modifications in the near-surface layers of the atmosphere, such as strengthened ocean-atmosphere heat fluxes that reduced the static stability over the SST anomaly (Crimp et al, 1998).

1.1.7. **Changes in the intertropical convergence zone before, during and after a TTT**

The intertropical convergence zone (ITCZ) is a band of tropical circulation in the vicinity of the equator where the north-easterly and south-easterly trade winds converge (Wallace & Hobbs: 15,16, 2006).

In 1987 a study was conducted on moisture bursts, which are essentially bands of upper (or middle and upper) cloud bands that extend from the tropics poleward (McGuirk et al, 1987). It

was found that in the eastern tropical Pacific Ocean moisture bursts are rare during an active ITCZ mode, which usually occurs during summer or during a strong ENSO event (McGuirk et al, 1987). The time mean behaviour of the local Hadley cell should be composed, or at least partly composed, by the time mean behaviour of an ample amount of brief, synoptic moisture bursts during a weak ITCZ mode (McGuirk et al, 1987). It was then concluded that moisture bursts can be connected to the tropical Hadley cell in a similar way that frontal cyclones are connected to the mid-latitude Ferrell cell (McGuirk et al, 1987). Moisture bursts also resemble local amplifications of a thermally direct overturning in their zonal average, which relates to a temporary Hadley cell (McGuirk et al, 1987). These moisture bursts are usually associated with tropospheric-wide increases in the mean westerlies, and momentum flux from the tropics and subtropics to the mid-latitudes is largely increased (McGuirk et al, 1987).

It was also found that the ITCZ changes over southern Africa and Madagascar during the occurrence of a TTT, but remains climatologically unchanged over other regions (Ratna et al, 2013). Instead of changing its positions over southern Africa, it breaks down (Ratna et al, 2013). Prior to a TTT, the continental part of the ITCZ intensifies over southern Africa after which it spreads southward to follow the mid-latitude influence during and after the event (Ratna et al, 2013).

1.1.8. Correlation of TTTs with ENSO

In previous studies, it was found that TTT events are more associated with La Niña events than with El Niño events (Manhique et al, 2011; Ratna et al, 2013). The apparent reason for this is that during La Niña events there is enhanced tropospheric convection around the Sumatra region in the Pacific Ocean, which in turn modifies the Walker circulation, causing upper level convergence over the western equatorial Indian Ocean (Ratna et al, 2013). In another study, it was found that La Niña events influence the intensity of TTTs, the suggested reason for this being through the enhancement of the pressure gradient over the southwest Indian Ocean between the tropical and subtropical regions, as well as through the strengthening of the Angola Low (Manhique et al, 2011).

During El Niño events, the rainfall patterns across the globe shift eastward due to the shift in the Walker Circulation. It was found that an anomalous upper-level convergence and an anomalous lower-level divergence exist over southern Africa during El Niño (Ratna et al, 2013). Seasonal rainfall is reduced due to the lower-level divergence over the subcontinent that

prevents moisture transport from the southwest Indian Ocean to southern Africa (Ratna et al, 2013).

1.1.9. Statistical Analysis in previous studies on TTT events

In earlier studies the characteristics of TTTs were investigated using objective methods such as principal component analysis and cluster analysis (Fauchereau et al, 2009; Manhique et al, 2011; Ratna et al, 2013; Washington and Todd, 1999; Williams et al, 2007). In the study by Ratna et al (2013) an index for TTTs was formulated, which is based on two facts: over southern Africa convection exhibits a dipolar structure; and TTTs exhibit a ridge-trough-ridge synoptic pattern that extends from the southern Atlantic Ocean to Madagascar. This TTT index was created using a thirty-year daily dataset for the summer season of 1980-1981 to 2009-2010 and for which a TTT event is defined with the conditions that the standard deviations of outgoing long wave radiation (OLR) must exceed 1.5 and that of wind must exceed 0.5 (Ratna et al, 2013).

1.1.10. Case studies on TTT events

Three events of heavy summer rainfall were identified that were associated with TTTs, namely: 31 December 1997 – 2 January 1998, 5 – 7 January 1998 and 15 – 17 December 2007 (Hart et al, 2010). The first two (in the summer of 1997 and 1998) fell within a strong El Niño season and the last one (in 2007) was during a strong La Niña season. During the study of these three events it was found that TTTs are related to planetary wave structures, because a few days before each event, anti-cyclonic wave breaking left a weak potential vorticity streamer across southern Africa (Hart et al, 2010). The low potential vorticity air in the upper atmosphere encouraged a surface low to transport moisture southwards into subtropical southern Africa, which in turn triggered convection and cloud band formation (Hart et al, 2010). It was also found that the primary role of the Angola Low during these case studies were to enable moisture transport into subtropical southern Africa (Hart et al, 2010). A low-level low-pressure feature, which probably developed due to upper-level divergence downstream of an upper-tropospheric trough, developed two days prior to the extreme rainfall days in two of the cases (Hart et al, 2010). This low-level disturbance diverted the moisture deeper into the subtropics, which could have led to higher amounts of rainfall (Hart et al, 2010). In conclusion, it was found that in all three cases the appearance of an upper-level trough over southern Africa, associated with a band of divergence to the east thereof, triggered TTT cloud band formation (Hart et al, 2010).

As mentioned earlier in this chapter, upper level waves have been identified as a very important ingredient in the formation of TTT events (Harangoza and Harrison, 1983; Todd et al, 2004).

Another study focused on the heavy rain producing system of 12 – 14 February 1996 (De Coning et al, 1998). During this time two cloud bands occurred, one associated with a subtropical moist conveyor belt or tropical plume and the other associated with a mid-latitude cyclone and frontal system (De Coning et al, 1998). The tropical plume was the instigator of this event and in combination with several different triggering mechanisms the heavy rainfall event occurred (De Coning et al, 1998). On the first and second day of the event heavy rainfall was due to deep convection; on the first day, it was triggered by a short-wave trough in the mid-latitude westerlies and on the second day it was triggered by enhanced, moist northerly flow that resulted from an approaching mesoscale convective vortex (De Coning et al, 1998). During this study, orographic ascent appeared to be a contributing factor to the convection initiation, because much of the heavy rainfall occurred on upwind slopes (De Coning et al, 1998). Heavy rainfall on the last day of the event seemed to be rather from the lifting of the western edge of the moist plume by the passing cold front and mid-latitude trough (De Coning et al, 1998).

1.1.11. **Importance of modelling and understanding TTT events**

Due to the great influence TTTs has on southern African rainfall, it is important to gain a better understanding as to how accurately models capture these systems. In many occasions, severe flooding from extreme rainfall events associated with TTTs not only leads to severe property damage, but also to loss of cattle and in some cases fatalities. Informal settlements in lower-lying areas can suffer severely from such events, because of the lack of a trustworthy early warning system.

Confidence in model simulations of TTTs may possibly be gained from this study over southern Africa and the south-western Indian Ocean, which may lead to more skilful operational seasonal forecasts. Forecasting TTTs more skilfully can in turn assist with an improved early warning system to inform inhabitants of low-lying areas, as well as warn farmers of possible flooding. More skilful operational seasonal forecasts can also assist farmers in their decision making of which crops to plant in a specific season.

Other entities like the Electricity Supply Commission of South Africa (Eskom) can benefit from this study. Early warning of long periods of constant rain, where the coal supply may be insufficient due to a lack of dry coal, will help them to be better prepared for such situations.

For all the reasons mentioned above, it is important to see how accurate numerical models can see TTT events and their characteristics, especially on a seasonal scale. A positive outcome of this study can improve the confidence of current medium and long-range forecasts.

1.2 Numerical Meteorological Models

Meteorology and weather forecasting have come a long way. The study of meteorology itself dates back as far as 500BC! Since then meteorology and weather forecasting have developed in such a way that clusters of computers are used not only for day-to-day forecasts, but also for seasonal forecasts and even longer-range forecasts. Nowadays human forecasting is combined with numerical models, which are based on the basic laws of physics, i.e. the conservation of mass, momentum and energy, to create weather forecasts (Wallace & Hobbs: 1, 2006). In situ data is more easily obtainable across the continents as well as the oceans, and in combination with satellite imagery these data sets give forecasters a good indication of the current atmospheric conditions.

1.2.1 History of Numerical Weather Prediction

The basis for numerical weather prediction was set by Vilhelm Bjerknes when he stated in a paper that the laws of physics can be used to predict weather (Bjerknes, 1904). Lewis Fry Richardson developed the concept of modern-day numerical modelling in 1922 (Richardson, 1922), but due to the large amount of calculations needed, real progress on this subject matter was only possible after the development of computers, which happened in the mid-1940s (Schuman, 1989). In 1946 John von Neumann started a project, named the Electronic Computer Project, to build and design a computer that has more power than the earlier computers (Shuman, 1989). In 1954 the Joint Numerical Weather Prediction Unit (JNWPU) was established in the United States of America and by March 1955 the unit issued numerical weather predictions twice daily (Schuman, 1989). Edward Lorenz also played a role in the development of numerical weather prediction. He described the chaotic properties of the atmosphere in a paper he wrote in 1963 (Lorenz, 1963). The first attempt of numerical weather prediction used the two-dimensional barotropic model for various reasons, but the main reason

is because of the simplicity of the barotropic model and how this model posed as a good starting point to explore the dynamics of the atmosphere (Bolin, 1955).

Modern day numerical modelling has developed significantly since then. There are various computer models simulating the state of the climate system. Coupled models also exist in which various types of models are combined, for example an atmospheric and oceanic model. Before December 1992 numerical weather prediction had more a "deterministic" approach and consisted of computer resources that were devoted to produce the most accurate possible single global forecast for up to 10 days (Tracton & Kalnay, 1993). Nowadays a "probabilistic" approach is taken using the same computer resources but to provide various sets of forecasts, which are usually of lower resolution (Tracton & Kalnay, 1993). Due to the nature of the ensemble approach, medium and longer-range forecasts are considered stochastic and not deterministic in nature, which is because of the inevitable growth of differences in forecasts when using only slightly different initial conditions (Lorenz, 1963; Tracton & Kalnay, 1993). It can be deduced that the ensemble mean will in general produce a better forecast than most of the individual ensemble members (Tracton & Kalnay, 1993).

The UK Met Office bought their first computer in 1959, which was able to do 30000 calculations per second (UK Met Office 2012). They started producing routine computer forecasts in 1965 (UK Met Office 2015). Since the 1970s the global exchange of observational data grew immensely and this is also the time when different meteorological centres started to exchange satellite data (UK Met Office 2015). Since the IBM 360/195 computer the UK Met Office used in 1971, their forecasting systems have improved significantly (UK Met Office 2015). In 1990 they implemented the Unified Model, which has now been upgraded a few times and currently uses an ensemble to provide information on the model first guess error structure (UK Met Office 2015).

1.2.2 Current Models

The development of current numerical models does not solely depend on a specific individual or a specific company, but rather the cooperation between various teams (Coiffier, 2011). This led to the development of unified models or community models, specifically in Europe, that were designed for several categories of users in different meteorological services (Coiffier, 2011). Examples of such international cooperation are listed below (Coiffier, 2011):

- ALADIN/LACE (developed by Météo France and scientists from central and eastern Europe)
- ARPEGE/IFS (developed by Météo France and ECMWF)
- The model developed by the Deutcher Wetterdienst and used by members of the COSMO consortium
- HIRLAM (developed by the Scandinavian countries, Estonia, Lithuania, Ireland, the Netherlands and Spain)
- The Unified Model (developed by the UK MetOffice)
- WRF (developed by various agencies in the USA)

The skill of current numerical models is constantly improving, not just because of the growing field of technology, but also because of the ongoing research in this field. Various meteorological centres are producing seasonal forecasts as part of the ongoing routine by using long integrations of general circulation models (GCM; Graham et al, 2005). Useful skill for specific regions and specific seasons were shown by the seasonal forecasts of these different GCMs (Arribas et al, 2011). When comparing coupled ocean-atmosphere GCM (CGCM) with two-tier atmosphere-only GCM (AGCM) forced with an independent prediction of SST evolution, it was found that the CGCM provide more substantial benefits for seasonal forecasts than the AGCM, not only in the tropics but also in the extra-tropics (Arribas et al, 2011; Graham et al, 2005). This result has also been found for southern Africa (Landman et al, 2012a). However, CGCMs are significantly costlier to develop and to operate than two-tier AGCMs (Graham et al, 2005).

In 2015 the UK Met Office received the first part of their latest supercomputer (UK Met Office 2015). When this supercomputer is fully operational, it will have the memory of more than half a billion numbers, and it will be able to do 23 000 trillion arithmetic operations per second, which will enable higher resolution forecasts (UK Met Office 2015). This is where current numerical weather prediction stands and it can only be improved in the future. This study will also be using hindcast data from one of the coupled ocean-atmosphere global circulation models developed by the UK Met Office, namely the Global Seasonal Forecast System version 5 (GloSea5).

1.3 Study description

1.3.1 The need to investigate TTT events

There is a need to understand TTT events better at the synoptic scale (Ratna et al, 2013; Vigaud et al, 2012) and also to understand how models see TTT events. Therefore, this study will investigate this weather phenomenon by using the GloSea5, a high-resolution seasonal forecasting system, which has not yet been used for TTT investigative application. Analysing TTT events will provide insight into how models simulate these weather phenomena and in turn this can help predict these events better in the future, providing a better early warning system for low-lying areas and informal settlements that are easily affected by floods.

It is important to determine whether the forecasting models predict wet seasons for the right reasons, i.e. is the reason for a specific wet season due to more TTT events that produce fewer wet days, but with more rainfall per day or is the reason that there are lots of wet days producing small amounts of rainfall due to various weather systems.

1.3.2 The benefits to investigate TTT events

Confidence in model simulations of TTT events may possibly be gained from this study over southern Africa and the south-western Indian Ocean, which may provide more skilful operational seasonal forecasts. Forecasting TTT's more skilfully can in turn assist with an improved early warning system to inform inhabitants of low-lying areas and farmers of possible flooding and it can also assist farmers in planning better for a specific season's crop.

Other entities like Eskom (Electricity Supply Commission of South Africa) can also benefit from this study. Early warning of long periods of constant rain, where the coal supply may be insufficient due to a lack of dry coal, will assist them to be prepared for such a situation.

1.3.3 Research problem

Evidently, there exists the need to better understand TTT events across southern Africa. It is also beneficial to be able to predict the occurrence of these events on a seasonal scale for the summer rainfall season, which will help for example farmers to better prepare for the amount of seasonal rainfall that can be expected.

1.3.4 Research Question and Objectives

To address the research problem mentioned above, the following question needs to be answered: what is the ability of a state-of-the-art seasonal forecast model to simulate TTT characteristics over southern Africa on a seasonal scale? In order to address this research question there are a few objectives:

1. Identify the distinctive cloud bands associated with TTT events using gridded data
2. Investigate the characteristics of modelled TTT events using the gridded data:
    a. Frequency of TTT occurrences
    b. Location of TTT events across southern Africa
    c. Intensity of TTT events over southern Africa

1.3.5 Challenges and limitations

Challenges can arise from retrieving observational data for an extended period due to incomplete data at some stations across southern Africa. The modelled data with the chosen parameters and variables may not correctly indicate the occurrence of TTT events, which means more data, with additional parameters, will have to be generated. The spatial resolution of the GloSea5 (or the observed data) may not be small enough to pick up on specific characteristic of TTT events. The area selected for this investigation may be too small or too large.

1.4 Thesis Layout

The principle of ensemble forecasting has been quite successfully used on medium range forecasts (Coiffier, 2011). This principle can be extended to all the different forecasting ranges, including seasonal forecasts (Coiffier, 2011). For this study the GloSea5 of the UK MetOffice has been chosen to evaluate the characteristics of TTT events across southern Africa during the summer rainfall period. The GloSea5 model is a state-of-the-art seasonal forecast model that has been recently developed by the UK MetOffice.

In the next chapter, the methodology to investigate the characteristics of TTT events will be discussed in detail, including the model, the “meteorological robot” and the datasets used. Thereafter four chapters on the results will follow (chapter 3 to 6). Chapter 7 consists of a detailed discussion of the results. The final chapter of this thesis, chapter 8, entails a conclusion,

possible future studies on the formation and development of TTT events, and a few final remarks.

CHAPTER 2: Methodology

2.1 Introduction

TTT events are important weather phenomena that play a major role in rainfall across southern Africa, especially during the summer rainfall season (e.g. Taljaard, 1996; Hart et al, 2013). These events can be identified by various characteristics such as the typical cloud bands (e.g. Hart et al, 2012), the eastward progression of the cloud bands and the geographical span of the event (Fauchereau et al, 2009; Pohl et al, 2009). In this study, hindcast data from a state-of-the-art coupled atmosphere-ocean general circulation model (CGCM) is compared to reanalysis data in order to establish whether the characteristics of TTT events can be relayed by a numerical model on a seasonal scale. A statistical approach is considered to compare the results of the modelled data and the observed data, and to establish whether the CGCM has skill in forecasting the characteristics of TTT events across southern Africa during the summer rainfall season. Hereafter will follow a discussion on how TTT events can be identified. Then a detailed description of the CGCM will follow, after which the observed and modelled datasets used in this study, are discussed. The domain and software used to analyse the data will also be described, and finally the statistical processes used will be explained.

2.2 Identification of TTT events

One of the key characteristics of TTTs is the typical cloud bands that develop as a result of tropical-extratropical interactions. The cloud bands associated with TTTs are usually orientated in a NW-SE direction in the southern hemisphere and in a SW-NE direction in the northern hemisphere. The cloud bands typically stretch from the tropics to the mid-latitudes. Within these cloud bands, areas of enhanced tropical convection can be found which is clearly identifiable on satellite imagery. These areas are usually where heavy rainfall occurs during a TTT event. To identify a TTT within the observed and modelled data, the focus during this study is on the cloud bands and the structure and position thereof. A Meteorological Robot (MetBot) (Hart et al, 2012) is used to identify these cloud bands by applying a certain criterion

to the data. This criterion, as well as an in-depth discussion on the MetBot will follow in section 2.6.

The progression of the cloud bands is also important. Usually a TTT event lasts three to five days, but the duration can be longer. During a TTT event, the cloud band moves eastwards (Fauchereau et al, 2009; Pohl et al, 2009), during which heavy rainfall can occur for consecutive days. The Metbot used in this study identifies the cloud bands and therefore also the days on which cloud bands were present. Consecutive days on which cloud bands occur, could potentially represent a TTT event.

The precursors to a TTT event and the development of such an event were discussed in section 1.1.3. One can therefore possibly forecast the occurrence of a TTT event by looking at the different atmospheric circulation features that play a role during the development of a TTT. However, the presence of these atmospheric circulation features does not necessarily indicate that a TTT event is imminent. To identify TTT events, atmospheric flow associated with these circulation features should first be identified, which leads to various atmospheric variables that can be considered when attempting to model TTT events, such as wind vectors and atmospheric pressure. For this study, however, only outgoing long-wave radiation (OLR) is considered, since OLR values represent TTTs the best as they relate directly to the characteristic cloud bands, which are associated with TTT events. Ultimately, observed rainfall may also be considered to verify whether a cloud band event was indeed a TTT, by evaluating periods of heavy rainfall.

2.3 The GloSea5 model

The Global Seasonal Forecast System version 5 (GloSea5) is a high resolution coupled ocean-atmosphere seasonal forecast model that was developed and is currently used by the UK Met Office (Graham et al, 2005). Since the first version was developed, there have been a number of changes and improvements. The previous version, the GloSea4 was found to have the ability to predict seasonal to inter-annual variability over southern Africa (Landman et al, 2012b). In this study hindcast data from the GloSea5 will be used.

The GloSea forecasting system, but specifically the GloSea4 system, was designed with the idea in mind to rapidly improve the skill of long-range forecasts of the current models and systems used for seasonal forecasting (Arribas et al, 2011). It is also a flexible and easy-to-upgrade system that is fully integrated within the UK Met Office model development infrastructure (Arribas et al, 2011). Since 2009 the UK Met Office was able to introduce improvements to their forecasting systems, which has been reflected in the skill of their forecasts (MacLachlan et al, 2014). There are various advantages in using the GloSea forecasting system, one of them is that hindcast and forecast components run simultaneously, which avoids the need to complete all the hindcast runs in advance (MacLachlan et al, 2014). A few notes on the finer details of the GloSea5 will follow in the next sections, however for a full and detailed description, please refer to the paper by MacLachlan et al (2014).

2.3.1 Resolution of the GloSea5

One of the major differences between the GloSea4 and the GloSea5 is the higher horizontal resolution in the GloSea5 (MacLachlan et al, 2014). The GloSea5 runs on a horizontal resolution of 0.833º x 0.566º for the atmosphere and land surface, which relays to approximately 50km in the mid-latitudes, and for the ocean and sea-ice models the horizontal resolution is 0.25º x 0.25º (MacLachlan et al, 2014; Scaife et al, 2014). The vertical resolution of the GloSea5 is 85 quasi-horizontal atmospheric levels, with an upper boundary of 85km near the mesopause, and 75 quasi-horizontal levels for the ocean (Scaife et al, 2014).

2.3.2 Configuration of the GloSea5

The coupled Hadley Centre Global Environmental Model version 3 (HadGEM3) is used within the GloSea5 and consists of the following components: for the atmosphere the Unified Model of the UK Met Office is used, for land surface the Joint UK Land Environmental Simulator (JULES) is used, the ocean model is initialised using the Nucleus for European Modelling of the Ocean (NEMO) and for the sea-ice component the Los Alamos Sea-Ice Model (CICE) is used (Arribas et al, 2011; MacLachlan et al, 2014). The previous NEMO version had a refinement in resolution (from 1º to 0.33º) between 20ºN and 20ºS, which lead to a better representation of tropical waves. This was eluded in the newer, higher resolution version, which has a global resolution with a grid space of 0.25º, the equivalent of 27km on the equator (MacLachlan et al, 2014).

2.3.3 Initialization

For the GloSea5, ensemble members were at first initialized on Mondays, and forecasts of three consecutive weeks were used in a lagged ensemble (MacLachlan et al, 2014). Fourteen forecasts were completed each week with the HadGEM3 coupled model with the members initialised from analyses valid for 0000UTC on the Monday of each week (MacLachlan et al, 2014). Analyses valid for that specific day have now been used since March 2011 to initialize the forecast members (MacLachlan et al, 2014). To achieve a spread between different ensemble members that are initialized on the same date, a stochastic physics scheme (SKEB2, Bowler et al, 2009) is utilized (MacLachlan *et al*, 2015). The initial conditions are generated as follows for the different model components (MacLachlan et al, 2014):

- Atmospheric initial conditions: Met Office operational numerical weather prediction 4D-Var data assimilation system (Rawlins et al, 2007)
- Ocean and sea-ice initial conditions: Forecast Ocean Assimilation Model (FOAM)
- Ocean and sea-ice hindcast initial conditions: Reanalysis data from the GloSea5 Ocean and Sea-Ice analysis
- Atmosphere and land surface (in the hindcast members): Reanalysis from the European Centre for Medium-Range Weather Forecasts (ECMWF) ERA-Interim project
- Soil moisture initial conditions: from land surface reanalysis using JULES land surface model forced with the Integrated Project Water and Global Change (WATCH) Forcing Data methodology applied to ERA-Interim data (WFDEI; Weedon et al, 2011)

Both the forecast system and the hindcast system of the GloSea5's ocean and sea-ice components use three-dimensional variational ocean data assimilation of NEMO, which is based on the multi-institution NEMOVAR-project (MacLachlan et al, 2014; Mogensen et al, 2009, 2012).

2.3.4 Ensemble prediction system

GloSea5 is a monthly to seasonal forecast system that comprises of three parts: an intra-seasonal forecast part, a seasonal forecast part and a hindcast part. For the operational forecast system four ensemble members are initialised each day with the 00:00UTC run analyses from the Numerical Weather Prediction (NWP) global data assimilation and the ocean-sea-ice data assimilation system (MacLachlan et al, 2014). For the hindcast data set, the model is initialized on the 1st, 9th, 17th and 25th of each month with three ensemble members per start date per year (MacLachlan et al, 2014). Each week a new set of hindcast data is completed for a period of

14 years, which is used to bias correct all the forecast ensemble members (MacLachlan et al, 2014). In order to achieve a spread between the three ensemble members initialized on the same date for the hindcast data set, the same stochastic physics scheme mentioned in section 2.3.4 is utilized (MacLachlan et al, 2015).

2.3.5 Performance of the GloSea5

It was found that the various upgrades performed from the GloSea4 to the GloSea5 forecast system improved ENSO patterns, the prediction of the Western North Pacific Subtropical High and the presenting of tropical cyclones (MacLachlan et al, 2014). Useful skill was also shown for predicting the Arctic Oscillation and the North Atlantic Oscillation, and statistically the GloSea5 showed significant prediction skill for tropical cyclone number, accumulated cyclone energy index and landfall frequency of tropical cyclones (MacLachlan et al, 2014).

During this study, the GloSea5 forecast system's ability to predict characteristics of TTT events will be put to the test by comparing the hindcast data set to reanalysis data by using a "meteorological robot" to identify TTT events, followed by a statistical analysis (as discussed in sections 2.6 and 2.8).

2.4 The OLR-data

Several atmospheric parameters can be considered for a study of TTT events, such as daily OLR, specific humidity, as well as zonal and meridional wind velocity, but only the results of daily OLR are considered in this study. The reason for this (as mentioned in section 2.2) is that OLR represents cloud bands the most accurately as it relates directly to enhanced tropical convection, and therefore the characteristic cloud bands associated with TTT events. The modelled daily OLR data is compared to observed daily OLR values from the National Environmental Satellite Data and Information Service (NESDIS) of the National Oceanic and Atmospheric Administration (NOAA).

2.4.1 OLR

All objects emit radiation. In terms of the sun, most of its radiation (solar radiation) is emitted at short wavelengths (majority of wavelengths are less than 2μm), while the earth's radiation

(terrestrial radiation) falls mostly in the longer wavelength section (between about 5 and 25μm) (Ahrens:35-38, 2007; Wallace & Hobbs: 113-114, 2006). Within the atmosphere there are molecules such as water vapour, carbon dioxide and other gases, which tend to absorb the outgoing longwave terrestrial radiation more than the shortwave solar radiation, because of electric dipole moments within the molecules (Wallace & Hobbs: 120-121, 2006). As a result, incoming solar radiation passes more freely through the atmosphere than outgoing terrestrial radiation. Figure 2.1 depicts a diagram of the incoming solar radiation, how much of it is absorbed by the atmosphere and the Earth's surface, as well as the outgoing radiation emitted by the Earth's surface, atmosphere and clouds.

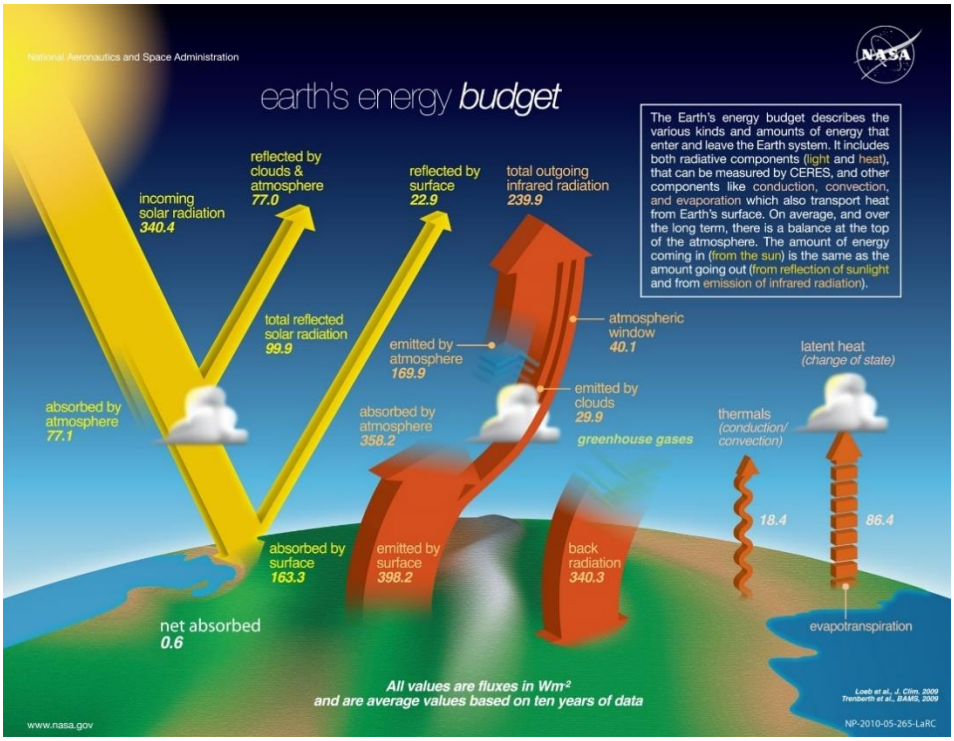

Figure 2.1: A diagram illustrating Earth's Radiation (Energy) Budget. It shows incoming shortwave solar radiation, how much of it is absorbed and by what means, as well as outgoing radiation (the values are in $W.m^{-2}$). Yellow arrows portray radiation from the sun or reflection of sunlight and orange indicates emission of infrared radiation. (Source: NASA, 2014)

The relationship between temperature and radiation is given by the Stefan-Boltzmann Law (eq. 2.1) and is written as:

$$E = \sigma T^4 \tag{2.1}$$

where E is the energy emitted by each square meter of surface area of the object or flux radiance, σ is the Stefan-Boltzmann constant ($\sigma = 5.67 \times 10^{-8}$ W.m^{-2}K^{-4}) and T is the object's temperature in Kelvin (Ahrens: 450, 2007). As a result, the unit for flux radiation is W.m^{-2} (Ahrens: 450, 2007).

Monitoring and measuring the radiation emitted by and reflected from the Earth is done by satellite-borne radiometers (Wallace & Hobbs: 139, 2006). Figure 2.2 shows the global distribution of the annual mean OLR as measured at the top of the atmosphere. There is a gradual change in OLR between the equator and the poles, and more regional variability in the tropics, whereas absorbed solar radiation varies greatly between the equator and the poles (Wallace & Hobbs: 144, 2006). In general, there is approximately a 2:1 difference in OLR values between the equator and the Polar Regions, partially due to the contrast in surface air temperature, but also by the fact that convective cloud tops and the top of the moist layer is higher in the tropics (Wallace & Hobbs: 144, 2006). The highest annual mean OLR is found over desserts, for example the Sahara, and equatorial dry zones over the tropical Pacific Ocean (Wallace & Hobbs: 144, 2006).

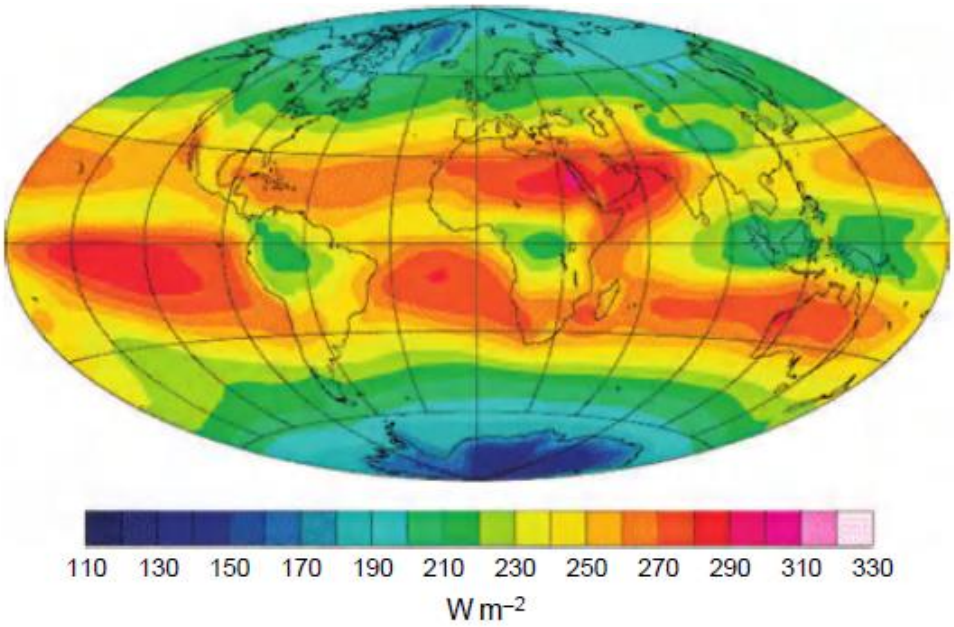

Figure 2.2: Annual mean global OLR measured at the top of the atmosphere. (Based on data from the NASA Earth Radiation Budget Experiment, source: Wallace & Hobbs: 144, 2006)

The amount of incoming solar radiation and OLR is not only dependent on the time of year, but also on the time of day and the weather conditions. It goes without saying that on a clear

day the amount of incoming solar radiation will be much more than on a cloudy day. The same applies for OLR – it will be less during an overcast night than during a cloudless night. Another point of note is that OLR values are in general higher during the night-time hours than during the day. In order to overcome these diurnal and nocturnal variances of very small OLR values during the day and large OLR values at night, daily OLR is used, which is an average value per day (24 hours). As was found in previous studies, the frequency distribution of daily OLR is bimodal with a peak for cold cloud tops and one for clear skies (Hart et al, 2012). This bimodal nature of OLR makes the choice for a threshold easier. Figure 2.3 shows an example of the probability distribution of the daily OLR, where the bimodal characteristic of OLR is clear. Therefore, the threshold for the daily OLR is chosen at 240 $W.m^{-2}$. In the area between 30˚N and 30 ˚S, low OLR values (in this case, lower than 240 $W.m^{-2}$) are generally considered to indicate convection (Liebmann & Smith, 1996).

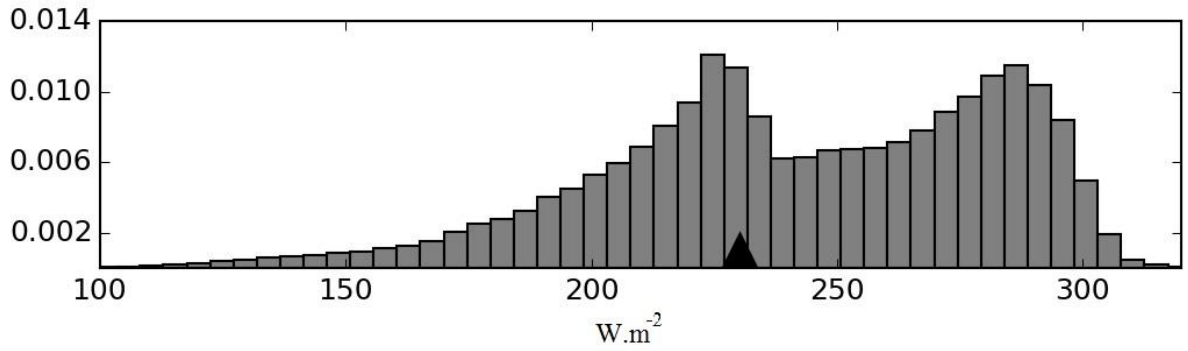

Figure 2.3: An example of the probability distribution of daily OLR values, which shows the bimodal characteristic of OLR. The black arrow between 200 and 250 $W.m^{-2}$ indicates the threshold value, in this case 240 $W.m^{-2}$.

2.4.2 Observed data

Observed daily OLR values from NESDIS of NOAA is used to establish the skill of the GloSea5 to forecast TTT events. This observed daily OLR data is archived onto a 2.5° x 2.5° grid (Liebmann & Smith, 1996). Temporal and spatial interpolation has been used to overcome the problem of missing values (Liebmann & Smith, 1996). A daily average is calculated from the two OLR data sets (day-time and night-time) (Liebmann & Smith, 1996). For a detailed description of the interpolation process, please refer to Liebmann and Smith (1996). This observational dataset is the same dataset used in previous studies regarding the use of the MetBot (Hart et al, 2012).

2.4.3 Model data

Daily OLR hindcasts from the UK's GloSea5 is used in this study. The hindcast data is obtained from three ensemble members, which are initiated at 0000UTC on the 1st, 9th, 17th and 25th of each month from 1 September until 1 November. This amounts to a total number of 27 ensemble members for each rainfall season (November, December, January and February, hereafter NDJF) of the years 1996/1997 to 2009/2010 (the study period considered for this study). As mentioned before, a spread between different ensemble members that are initialized on the same date is achieved by using a stochastic physics scheme (MacLachlan *et al*, 2015). There are several sections of modelled data missing during the considered study period of this study. To overcome missing modelled data issues, the observed data corresponding to the same time period or season was omitted during the analysis of the results. Therefore, the average value for the considered variables will differ for some of the ensemble members. The time periods with missing data are given in Table 2.1. In total for the period from 1996/1997 to 2009/2010 (14 years' rainfall season) a number of 378 ensemble members are available with complete (or semi-complete) datasets. The seasons with missing data do not have an effect on the efficiency of the MetBot and these seasons can easily be omitted during the analysis process of each ensemble member.

Table 2.1: Missing hindcast datasets and the periods of the missing data. M1, M2 and M3 indicate ensemble members 1, 2 and 3 respectively, which are initiated on the various dates (column 1).

Ensemble Member	**Date of missing data**		
Sept 1st M1	1-28 Feb '10		
Sept 1st M2	15 Jan-28 Feb '01	15 Jan-28 Feb '06	1 Nov '08-28 Feb '09
Sept 1st M3	1 Nov '99-29 Feb '00	1 Nov '02-28 Feb'03	1 Nov '05-28 Feb '06
Sept 9th M1	1 Nov '09-28 Feb'10		
Sept 9th M2	1 Nov '99-29 Feb'00	8 Jan-28 Feb'03	
Sept 17th M2	15-28 Feb '05		
Sept 17th M3	1 Nov '99-29 Feb '00	1 Nov '00-28 Feb '01	1 Nov '01-28 Feb '02
Sept 25th M1	1 Nov '02-28 Feb'03	24 Jan-28 Feb'05	
Sept 25th M3	1 Nov '01-28 Feb '02		
Oct 1st M1	1 Dec '04-28 Feb '05		
Oct 9th M3	23 Jan-28 Feb '99	22-29 Feb '00	
Oct 17th M1	17 Dec '01-28 Feb '02		
Oct 25th M2	10-24 Dec '05		
Oct 25th M3	25 Dec '98-28 Feb '99		
Nov 1st M2	1 Jan-28 Feb '99	15-28 Feb '06	

2.5 The Geographical Domain

The geographical domain for this investigation extends from 5°S to 50°S and 5°E to 80°E in order to capture all aspects and characteristics associated with TTT events over southern Africa. This domain is consistent with previous studies on TTT's over southern Africa (e.g. Fauchereau *et al*, 2009; Vigaud *et al*, 2012). This area includes the three preferred regions where TTTs tend to develop across southern Africa as previously discovered (Fauchereau et al, 2009) and confirmed (Vigaud et al, 2012). The span of the geographical domain can be observed in Figure 2.3. These three preferred regions where cloud bands tend to occur have their starting positions (anchor points/roots) above Namibia, Mozambique and Madagascar (this is where they originate and start to develop, marked by an X in figure 2.4), and stretch south-eastwards from there (Fauchereau et al, 2009; Vigaud et al, 2012).

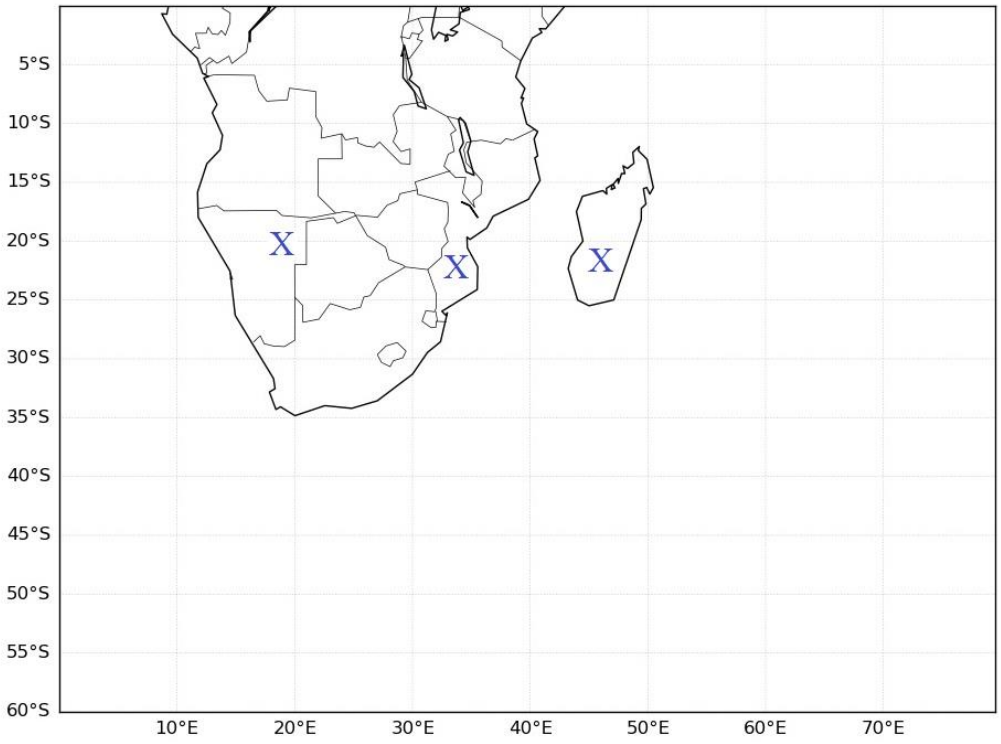

Figure 2.4: The geographical domain of this study, which spans from 5˚S to 50˚S and 5˚E to 80˚E. The three preferred regions where TTTs tend to develop across southern Africa are marked with a blue 'X'.

2.6 The MetBot

The methodology developed by Hart et al (2012) is used to identify TTT events in both the observed and hindcast data. The methodology was developed to use gridded data sets such as reanalysis and general circulation model outputs, to automate the synthesis of the cloud band meteorology associated with TTT events (Hart et al, 2012). This methodology consists of a meteorological robot (MetBot) that identifies cloud band systems by plotting daily OLR data with the maximum threshold at 240 $W.m^{-2}$ and running it through a blob detection algorithm (Hart et al, 2013). The blob detection algorithm is a procedure within the MetBot that detects areas with certain OLR values ("blobs") that essentially represent the cloud bands. The OLR values within these blobs adheres to the criteria of the MetBot. When OLR blobs extend from the tropics south-eastward into the sub-tropics, the cloud bands are flagged (Hart et al, 2013). OLR data values are then selected 48 hours before and after the flagged cloud bands, on which the process, with lower criteria, is repeated in order to establish a track for the cloud bands (Hart et al, 2013). From this analysis arises a data object for each event describing the development of the cloud band (Hart et al, 2013).

The Metbot uses Python as the analysis platform. Various libraries are used in order to identify the cloud bands and to produce plots (Hart et al, 2012). Once the cloud bands are flagged, the image analysis process can start. Images are analysed through the following steps, as laid out in Hart et al (2012):

1. Raw OLR data is stretched onto the grayscale image range [0,255].
2. A chosen threshold for the raw variable is translated into grayscale.
3. The image is plotted and fetched from a buffer to obtain a visual interpolation of the data.
4. A threshold is applied to this image array, which produces a binary image and performs connected component labelling to identify the cloud blobs.
5. An appropriate filter is run through the blobs to keep the relevant blobs, i.e. the "metblobs".
6. Information is retained that describes blob contour, the centroid position and the blob area.
7. The process is repeated at each time step.

The MetBot has been tested by using dates on which known TTT events were observed, and it has been found that the methodology captures the characteristic features of the formation and

development of TTT events over southern Africa, as well as the rainfall produced by these events (Hart et al, 2012).

2.7 Attending to the research question and the research objectives

In Sections 1.3.3. and 1.3.4. the research problem and the research question are stated, and a few objectives are identified in order to address the research problem. To accomplish the first objective, gridded data is processed using the MetBot to flag cloud bands. Both modelled and observed gridded data is processed using the same software and criteria. By processing the data using the MetBot, the cloud bands are flagged, therefore identified, by which the first objective is met. For all the calculations and comparisons of the different variables, ensemble members are considered separately, as well as combined. Equal weighting is used when combining the ensemble members.

Some of the subobjectives of the second objective derive directly from the output of the MetBot, but others need a somewhat more calculative approach. The frequency of TTT occurrences is calculated by comparing the modelled number of cloud bands with the observed number of cloud bands on a seasonal scale. This calculation is done using a statistical evaluation, which will be discussed in section 2.8. The location of the modelled TTT events is obtained from the output file of the MetBot. This file contains the coordinates of the start and end points, of each candidate cloud band, among others. There are different ways to investigate the intensity of TTT events. In this study, the intensity is investigated by looking at the area covered by each candidate cloud band and comparing it to the observed cloud band areas. The lowest and highest OLR (minimum and maximum OLR) values within the modelled cloud bands are also compared to that of the observed cloud bands. The lowest (or minimum) OLR value of a cloud band also gives an insight into the severity of the cloud band – the colder the cloud tops, the greater the instability within the convective cloud, therefore the greater the effects of the TTT event are. The highest (or maximum) OLR value on the other hand indicates the thinnest part of the cloud band, i.e. the section of the cloud band which allows the most OLR to pass through and reach the outer atmosphere.

2.8 Model evaluation procedure

Model development has played a large role in the atmospheric sciences over the last few decades and it currently still does. It is therefore important to evaluate models and improve them. When considering the evaluation of a model, it is significant to establish the difference between the following concepts: verification refers to the proof of the accuracy, reality or truth of a model; evaluation refers to the process of examining and assessing the model's performance by comparing modelled and observed data; and validation takes place when a conclusion of formal acknowledgment is established which may include various evaluations (Fox, 1981). During this study, the focus will be on evaluating the GloSea5 hindcast data with specific reference to TTT simulation.

In previous work, two types of performance measures were identified, namely, difference or residuals measures and correlation measures (Fox, 1981). A quantitative estimate of the size of the differences between the modelled and observed data is represented by difference measures, while correlation measures refer to the quantitative measure of agreement between the modelled and observed data (Fox, 1981). Difference measures include the mean bias error (MBE) which can be used to describe bias, the variability of the predicted minus the observed variable (P-O) about the MBE (s_d^2) (also the variance of the distribution of differences), Root Mean Square Error (RMSE) and its square (the Mean Square Error or MSE), and lastly the Mean Absolute Error (MAE) (Fox, 1981; Willmott, 1982). RMSE, MSE and MAE basically describe the average difference between the modelled and observed data (Willmott, 1982). There are various correlation measures that can be considered when evaluating atmospheric models. Examples of these correlation measures are Pearson's product-moment correlation coefficient (r) and the square thereof, called the coefficient of determination (r^2). Whether these two examples (r and r^2) should be used to evaluate atmospheric models has been questioned before (Willmott, 1982). One of the problems is that the magnitudes of r and r^2 do not always correlate consistently with the accuracy of the prediction; accuracy in this case being the degree to which model-predicted observations approach the magnitudes of their observed counterparts (Willmott, 1982). It seems that difference measures can give more appropriate and insightful information than correlation measures (Willmott, 1982).

In this study, various measures will be used, such as the RMSE, as well as the percentage deviation. In cases where the modelled data follows in general the same behaviour as the observed data, but significantly under or over estimates, a normalisation is applied. In extreme cases where no conclusion can be derived from the RMSE and the percentage error, as well as the average behaviour, it might be necessary to revert to a visual display of the results. In such cases the longitude and latitude of the variables (as calculated by the MetBot) will be used to be able to draw conclusions as to the performance of the model.

2.8.1 Number of candidate cloud bands and percentage deviation

By using the MetBot, candidate cloud bands are identified in both the modelled and observed data sets. The total number of modelled candidate cloud bands per season, per ensemble member and per group ensemble is calculated and compared to the number of observed candidate cloud bands per season. The percentage deviation of the number of modelled cloud bands from the number of observed cloud bands is calculated by using equation 2.2, where PD is the percentage deviation, CC_m is the number of modelled cloud bands and CC_{obs} is the number of observed cloud bands:

$$PD = \frac{CC_m - CC_{obs}}{CC_{obs}} \times 100 \tag{2.2}$$

2.8.2 Root Mean Square Error

Mean Square Error (MSE) is a common measure of accuracy for forecasts (Wilks: 359, 2011). The MSE averages spatially the individual squared differences between the gridded forecast and observed fields at each of the M grid points (Wilks: 359, 2011). This can also be written as:

$$MSE = \frac{1}{M}\sum_{m=1}^{M}(y_m - o_m)^2 \tag{2.3}$$

where M is the number of years, y_m is the number of candidate cloud bands per ensemble member and o_m is the number of observed candidate cloud bands. A perfect forecast will yield an MSE of 0, while larger MSE values indicate a decrease in forecast accuracy (Wilks: 359, 2011).

Another measure that can be used for accuracy is Root Mean Square Error (RMSE) (eq. 2.4), which has the advantage that the unit of the forecast variable is retained, which makes it easier to interpret (Wilks: 357, 2011).

$$RMSE = \sqrt{MSE} = \sqrt{\frac{1}{M}\sum_{m=1}^{M}\left(y_m - o_m\right)^2} \tag{2.4}$$

The same as with MSE, when the RMSE approaches 0, the accuracy of the forecast increases. In this study RMSE will be used rather than MSE.

2.8.3 Percentage error

After the RMSE is obtained, the percentage error is calculated using equation 2.5, where PE is the percentage error, RMSE is the calculated root-mean square error, M is the total number of years and o_m is the number of observed cloud bands. The denominator in the equation is the calculation of the average observed number of cloud bands.

$$PE = \frac{RMSE}{\frac{1}{M}\sum_{m=1}^{M} o_m} \tag{2.5}$$

The percentage error is calculated in order to put the RMSE values in perspective. For example, when using values as large as a few thousand square kilometres, as in the case of the area of a cloud band, an RMSE value of 8000 km^2 seems extremely large. However, by calculating the percentage error, it yields an error of only 2%. Therefore, the model performance can be better established by calculating the percentage error.

2.8.4 Bias-adjustment

As mentioned previously in this chapter, a normalisation is applied in the cases where the result of the model data follows the same year-to-year variability as the observed data, but where the model extremely under- or over-predicts the variable. In such cases the normalisation is applied to each ensemble member, before calculating the model average.

To apply the normalisation (bias-adjustment), equations 2.6 and 2.7 are used, where f is the difference between the average number of cloud bands of the observations (o_{avg}) and that of the ensemble member (EM_{avg}), EM_{un} is the bias-adjusted number of cloud bands of the ensemble member and EM_n is the number of cloud bands of the ensemble member before the bias adjustment was applied. After the bias is adjusted, the new RMSE values are calculated

for the newly calculated set of number of cloud bands (EM_{un}) using equation 2.4 and replacing y_m with EM_{unm}.

$$f = o_{avg} - EM_{avg} \tag{2.6}$$

$$EM_{un} = EM_n - f \tag{2.7}$$

2.9 Synopsis

This section concludes the chapter on the methodology used in this study. To summarise, observed and modelled OLR data is used as input in the MetBot developed by Neil Hart (2012). This MetBot flags cloud bands associated with TTT events. The output file containing the flagged cloud bands, also contains information about these cloud bands, namely the area, the minimum and maximum OLR values, the anchor points, the centroid position and the tilt of the cloud bands, and of course the number of cloud bands as well. This information is used to investigate whether a state-of-the-art seasonal forecast model, the GloSea5 of the UK Met Office, can forecast the characteristics of TTT events on a seasonal scale, as set out in the objectives and subobjectives of this study. These characteristics are investigated using various statistical calculations and, in some cases, visual representations, and comparing the observed characteristics with the modelled characteristics. In the following four chapters (chapter 3 to 6) the results are presented.

CHAPTER 3: Introduction to the Results

3.1 General guidelines for the results chapters to follow

OLR data is analysed using the MetBot (described in Section 2.6), which identifies candidate cloud bands by plotting the OLR data with a maximum threshold of 240 $W.m^{-2}$ and running it through a cloud band detection algorithm. The results obtained will be discussed in detail in the three chapters to follow (Chapter 4, 5 and 6). Both the hindcast and model datasets are run through the same detection algorithm, with the same criteria and maximum threshold.

In all the graphs and tables following in this chapter and the rest of this study, that concerns the ensemble members, abbreviations will be used for each ensemble member. One of the reasons for using abbreviations is to simplify the labelling of the x-axes. Table 3.1 indicates the abbreviation and the ensemble member it represents.

Table 3.1: A list of the abbreviation used for each ensemble member in this chapter and the following results chapters. The date in the second and forth column is the date on which the ensemble member is initiated. Ensemble member is abbreviated as EM.

Abbreviation	Ensemble member (EM)	Abbreviation	EM
1S1	1 September EM 1	1O3	1 October EM 3
1S2	1 September EM 2	9O1	9 October EM 1
1S3	1 September EM 3	9O2	9 October EM 2
9S1	9 September EM 1	9O3	9 October EM 3
9S2	9 September EM 2	17O1	17 October EM 1
9S3	9 September EM 3	17O2	17 October EM 2
17S1	17 September EM 1	17O3	17 October EM 3
17S2	17 September EM 2	25O1	25 October EM 1
17S3	17 September EM 3	25O2	25 October EM 2
25S1	25 September EM 1	25O3	25 October EM 3
25S2	25 September EM 2	1N1	1 November EM 1
25S3	25 September EM 3	1N2	1 November EM 2
1O1	1 October EM 1	1N3	1 November EM 3
1O2	1 October EM 2		

The season consisting of the months November, December, January and February (NDJF) is considered for all 27 ensemble members. Every season of the years 1996/1997 to 2009/2010 is averaged and then compared to the hindcast data. The aim of this project is to assess the performance of the GloSea5 model on a seasonal time-scale, not on a monthly or a daily scale. Therefore, the averages of a season are considered instead of the monthly averages. Take note that in this chapter and the following results-chapters, reference to only one year is used most of the time, instead of two years to indicate the entire season, for example 2004 is used instead of 2004/2005 to indicate the season from 1 November 2004 to 28 February 2005. This shortened version is used to simplify the labelling of the x-axes on the graphs. The year will always indicate the year in which the referred season starts, for example 1999 indicates the season starting November 1999 and ending February 2000.

3.2 MetBot results

For each candidate cloud band that is identified by the algorithm, two figures are produced and the information regarding the cloud band is saved in a file. This detail consists of the coordinates of the anchor point, the longitude and latitude of the centroid, the tilt and the area of the cloud band. The anchor point is the root of the cloud band in the tropics. From the anchor point, the cloud band stretches southeast to higher latitudes. A centroid is the arithmetic mean position of all the points in the shape, i.e. the centre of all the points in every coordinate direction. Other terms for the centroid, which are perhaps more familiar, are the centre of mass and the geographical centre. Occasionally two candidate cloud bands are flagged on the same day. Both cloud bands are considered as separate events and are therefore regarded as two separate cloud bands in the calculations.

Even though additional results, such as seasonal records, can be produced by the MetBot by using different input data, only OLR data is used, because OLR data is sufficient to address the problem statement and research question on TTTs. Therefore, the results are limited to what is mentioned in this chapter and the following three chapters.

An example of the two figures produced as output is presented in Figure 3.1 (a and b) for the cloud band flagged on 12 November 1996 in the observed dataset. The top one of these figures (Figure 3.1.a) displays the raw OLR data with an outline of the cloud band, as well as the tilt

thereof (usually a number between 0 degrees and -90 degrees). The bottom figure shows the blob of the cloud band, a blob being a geometrical figure with a random shape (Figure 3.1.b).

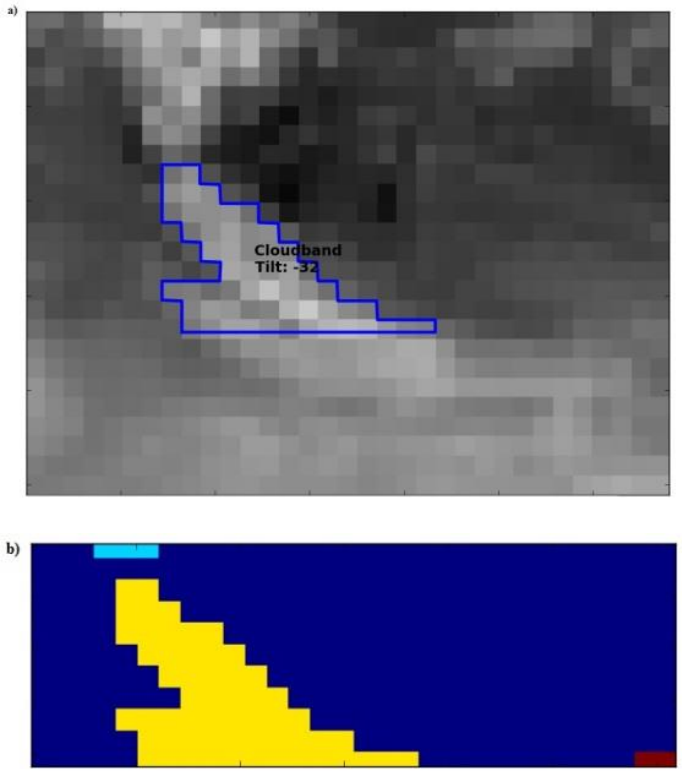

Figure 3.1: An example of the figures produced by the MetBot. This specific figure is produced by using the observed OLR on 12 November 1996. Raw OLR showing the cloud band (within the blue line) and the NW/SE tilt thereof is displayed in (a). The yellow OLR blob in (b) shows the candidate cloud band.

3.3 Synopsis

In this chapter general guidelines are given on information that will be needed for the rest of the results chapters of this study. Thereafter, it was proven that cloud bands can be identified by the model by running the data through a cloud band detection algorithm. By this means, the first objective of this study is achieved.

In the following chapter, the results to address first subobjective of the second objective will be presented, namely the frequency of TTT events. These results include the anchor point and the area of the cloud bands and results concerning both the modelled and the observed datasets will be provided.

CHAPTER 4: Frequency of TTTs

Cloud bands are flagged using the MetBot software. The results are compiled in an output file, from which different features of the cloud bands can be analysed. One of these features is the number of cloud bands. The number of cloud bands is an indication of the frequency of tropical temperate trough (TTT) events within the NDJF rainfall season and therefore addresses one of the objectives of this study. In this chapter the number of cloud bands of the model data will be compared to that of the observed data. First the total number of cloud bands and the averages over the seasons and study period are presented for the observed dataset and the 27 ensemble members. Thereafter a section on the percentage deviation will follow. This chapter concludes with a section on the root-mean square error and the corresponding percentage error. As mentioned in Chapter 3, abbreviations are used for the ensemble members. These abbreviations can be found in Table 3.1.

4.1 Total and average number of cloud bands

The total number of candidate cloud bands is considered on a seasonal time-scale for the months November to February of the study period ranging from 1996/1997 to 2009/2010. Where there are periods of model data missing, the observed data is omitted for the same period. This study is focused on the capability of a coupled model to predict TTT's on a seasonal scale, not a daily scale. Therefore, omitting these periods of data is necessary for consistency between the modelled and the observed datasets. This is also the reason why the average value of the observed variable will differ for some of the ensemble members.

Candidate cloud bands are sometimes identified by the MetBot for a few consecutive days. Instead of considering these consecutive occurrences as one TTT event, candidate cloud bands are considered separately for both the observed and the model datasets. By considering the cloud bands per day, the same rules apply for every cloud band in both the observed and the model dataset. Sometimes more than one candidate cloud band are identified for one specific day in which the one cloud band will lie in the eastern end (around Madagascar) of the geographical domain and the other one on the western side (around Namibia). In such a case both of the candidate cloud bands are considered, because this section (and the rest of this

study) focuses on the total number of cloud bands per season and per study period, not the specific days on which cloud bands are flagged. In both the modelled and the observed datasets there are days on which two cloud bands are flagged. The fact that the model also simulates two cloud bands on specific days, indicates that the model is performing well regarding the prediction of cloud bands, and therefore possible TTT events.

The number of cloud bands flagged by the MetBot in the observed dataset can be seen in Figure 4.1.1. The least number of cloud bands are observed in the season of 2006/2007 (25 cloud bands) and the most are observed in the season of 1998/1999 (50 cloud bands). On average, there are 37.36 observed cloud bands per season. This number only indicates the characteristic cloud bands associated with TTT events, not the actual TTT events. Therefore, this number is larger than one would expect for the number of TTT events in one NDJF season across southern Africa.

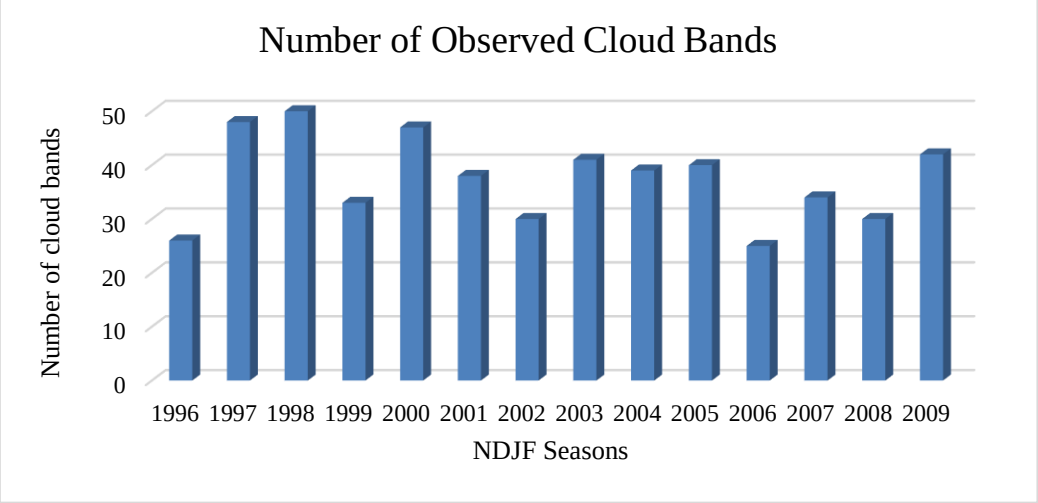

Figure 4.1.1: A graph showing the number of cloud bands flagged in the observed dataset for every season (November to February) in the period 1996/1997 to 2009/2010.

Due to the fact that there is data missing for parts of the study period for some ensemble members, the number of observed cloud bands used in the comparison between the ensemble members and the observed dataset will differ for some of the seasons. The missing model data amounts to a percentage of 0.288% of the total model dataset. Therefore, it can be said that whether or not the sections with missing data is excluded or not, will not make a significant difference in the final results.

Figure 4.1.2 shows the total number of cloud bands for the entire study period of 1996/1997 to 2009/2010 for the 27 ensemble members and the observed dataset. From Figure 4.1.2 it can be concluded that the ensemble members under-predict the number of cloud bands, and therefore the model inevitably under-predicts the number of cloud bands.

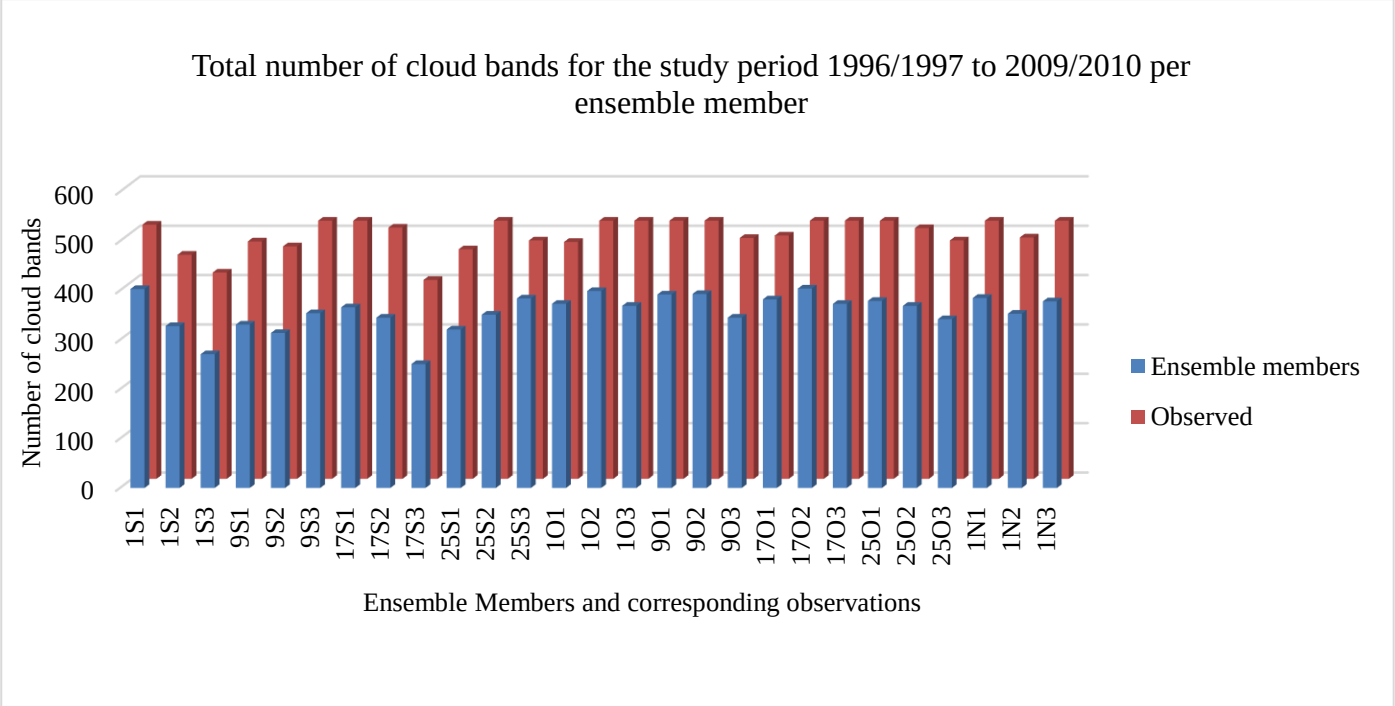

Figure 4.1.2: Graph indicating the number of cloud bands detected by the MetBot in the datasets of the 27 different ensemble members and the corresponding observations. The blue bars indicate the total number of cloud bands of the ensemble members and the orange bars indicate those in the corresponding observed dataset. Please refer to Table 3.1 for the abbreviations used for the ensemble members.

In Figure 4.1.3 the difference between the average number of cloud bands per ensemble member and the average number of cloud bands of the observations is illustrated. On average the model predicted 10.34 fewer cloud bands per season than that occurred. Therefore, it is verified that the different ensemble members and inevitably the model as well, under-predict the number of cloud bands. What is interesting to note is that the ensemble members with a shorter lead-time (the ensemble members initiated on 25 October and 1 November) under-predict the number of cloud bands more or less the same amount: in this case about 10 cloud bands too little. Lead-time is the time between the initiation date of the ensemble member and the start date of the considered months of the forecast, in the case of this study 1 November.

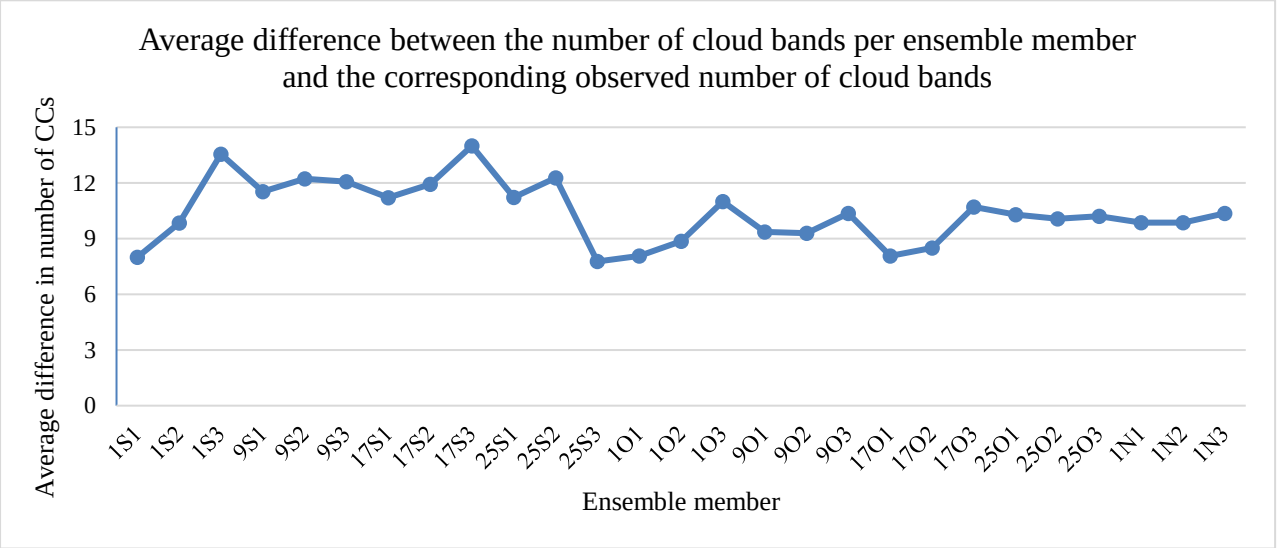

Figure 4.1.3: Average difference in the number of cloud bands between each ensemble member and its corresponding observed number of cloud bands. The words cloud bands are abbreviated as CCs.

The different ensemble members under-predicted the number of cloud bands for the entire period (1996/1997 to 2009/2010), but not for every NDJF season separately. Table 4.1.1 lists the NDJF seasons for which each ensemble member over-predicted the number of observed cloud bands. Interesting to note is that 22 of the 27 ensemble members (81.5%) over-predicted the number of cloud bands for the NDJF season of 1996/1997 and 13 of the 27 ensemble members (48.1%) for the 2006/2007 season.

Due to the fact that the ensemble members on average under-predicted the number of cloud bands, it was considered to adjust the bias of all the ensemble members separately. More on the bias-adjustment can be found in the Root-mean square error section (Section 4.3) later in this chapter.

To indicate by how many the different ensemble members under-predict the number of cloud bands, the percentage deviation and the Root-mean square error (RMSE) are calculated. These results will be presented in the two sections following Table 4.1.1.

Table 4.1.1: The NDJF seasons in which an ensemble member over-predicted the number of cloud bands, indicated by an 'X'. In the last row, the total number of ensemble members that over-predicted cloud band occurrences in that particular year is displayed.

	1996	1997	1998	1999	2000	2001	2002	2003	2004	2005	2006	2007	2008	2009
1S1	X										X			
1S2												X		
1S3	X										X			
9S1													X	
9S2	X										X			
9S3											X			
17S1	X						X				X			
17S2														
17S3	X													
25S1	X								X				X	
25S2	X											X		
25S3	X										X			
1O1	X						X		X		X			
1O2	X			X									X	
1O3	X													
9O1	X						X							
9O2	X													
9O3				X										
17O1	X									X		X		
17O2	X									X			X	
17O3	X			X										
25O1	X										X			
25O2	X										X			
25O3	X										X			
1N1	X										X			
1N2	X										X			
1N3	X										X			
Total	22	0	0	3	0	0	3	0	2	2	13	3	4	0

4.2 Percentage deviation

The percentage deviation is a measure to calculate the percentage the model data differs from the observed data and can be calculated using Eq. 2.2 and is calculated for each NDJF season in the study period spanning from 1996/1997 to 2009/2010 for each ensemble member, as well as the average percentage deviation over the entire period for all 27 ensemble members (the model/ensemble average).

Figure 4.2.1 indicates the average percentage deviation of the different ensemble members. From this figure it is apparent that every ensemble member under-predicts on average the number of cloud bands for the period 1996/1997 to 2009/2010. The average percentage deviation of the 27 ensemble members (the ensemble average) is calculated as -28.29%. Interesting to note is that the average percentage deviation seems to settle between -25% and -30% with a shorter lead-time, particularly for the ensemble members initiated on 25 October and 1 November. According to Figure 4.2.1, ensemble member 3 initiated on 25 September (25S3) performed the best with an average percentage deviation of -21.02%. The worst performer is ensemble member 3 initiated on 17 September (17S3) with an average percentage deviation of -37.97%. The data of the entire NDJF season of the year 2001/2002 is missing for ensemble member 25S3. Ensemble member 17S3 misses the data for three consecutive seasons (1999/2000, 2000/2001 and 2001/2002), which possibly contributes to the poor performance in predicting the number of cloud bands. The individual percentage deviation of the poorest and best performers is presented in Figures 4.2.2 and 4.2.3 respectively.

In the case where the data is missing for the entire NDJF season of a particular year, the line on the graph is connected from the previous year to the next year with available data. Thus, no interpolation was used in the calculations.

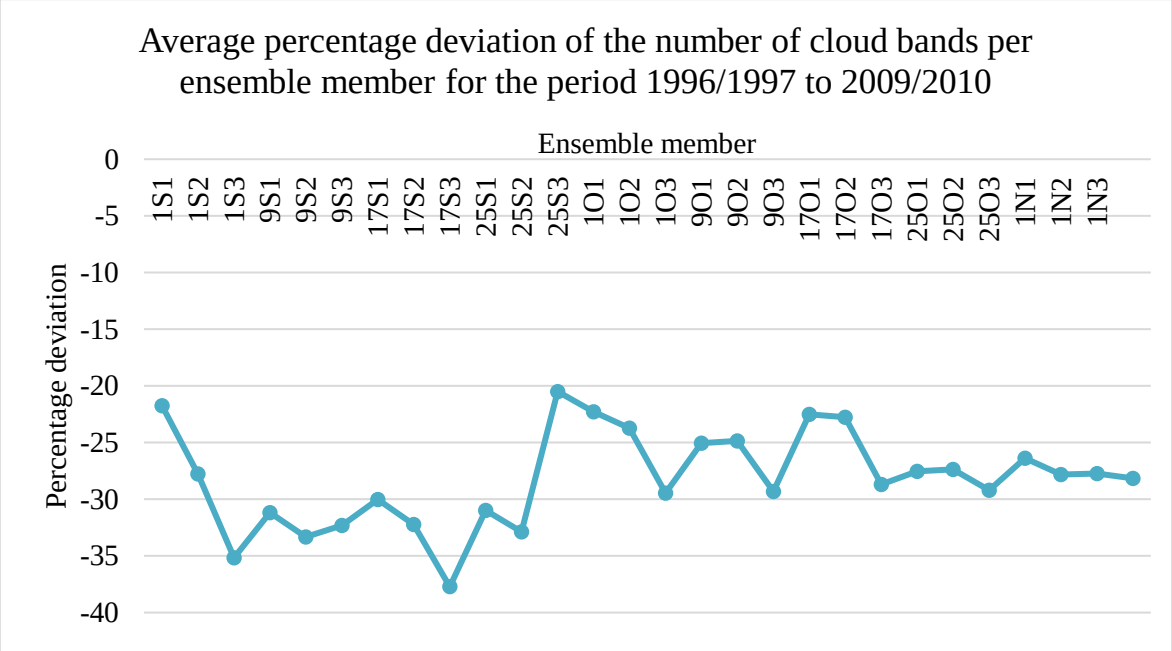

Figure 4.2.1: The average percentage deviation of the number of cloud bands for every ensemble member. The x-axis indicates the different ensemble members and the y-axis donates the percentage deviation. The abbreviations on the x-axis is explained in Table 3.1.

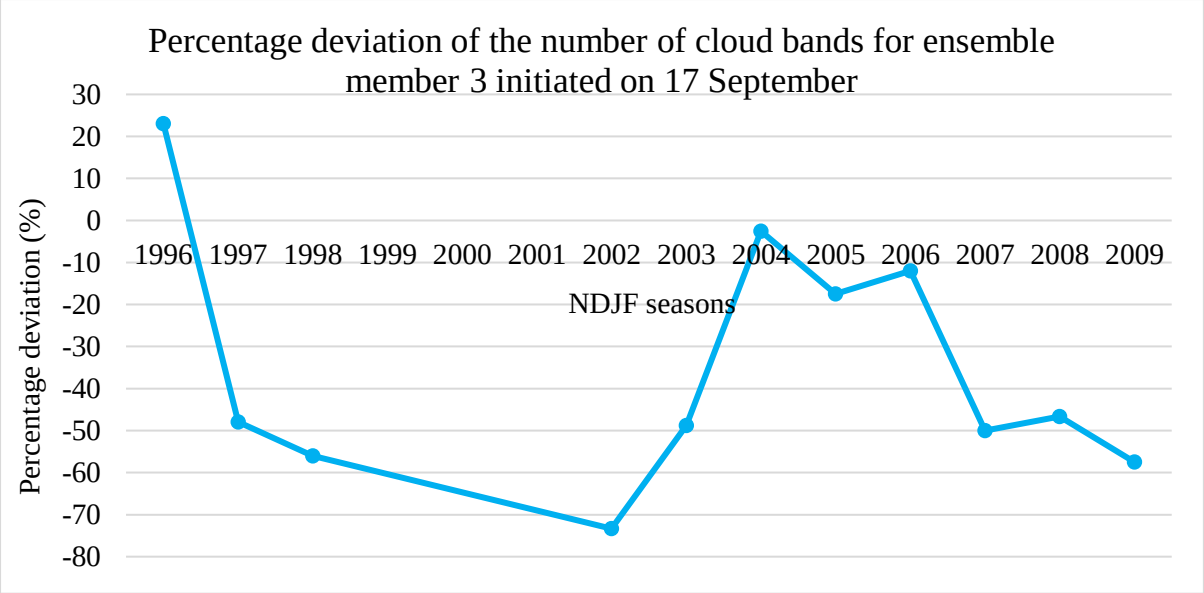

Figure 4.2.2: The percentage deviation of the number of cloud bands for ensemble member 3 initiated on 17 September. The x-axis indicates the different NDJF seasons in the study period and the y-axis donates the percentage deviation.

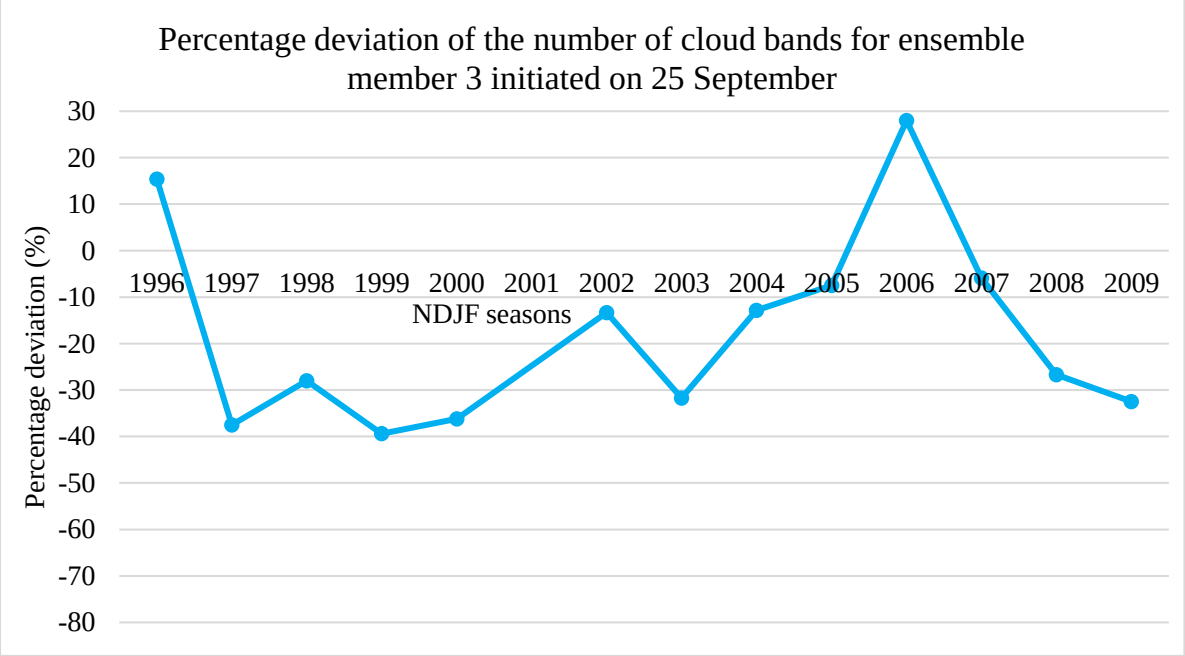

Figure 4.2.3: The percentage deviation of the number of cloud bands for ensemble member 3 initiated on 25 September. The x-axis indicates the different seasons in the study period and the y-axis donates the percentage deviation.

4.3 Root-Mean-Square-Error

The root-mean square error (RMSE) is used to measure the accuracy of forecasts (more on this measure in Chapter 2, Section 2.8.2). To calculate the RMSE, Equation 2.4 is used. After the RMSE is obtained, the percentage error is calculated using Equation 2.5.

The RMSE values and the corresponding percentage error of each ensemble member are presented in Table 4.3.1. The average RMSE of all the ensemble members is 14.22 cloud bands, which yields an average percentage error of 38.8%. Again, ensemble member 3 initiated on 25 September (25S3) fared the best with an RMSE of 10.94 cloud bands, while ensemble member 3 initiated on 1 September (1S3) performed the worst with an RMSE of 17.62 cloud bands. Ensemble member 1S3 has three seasons of data missing. These seasons are 1999/2000, 2002/2003, 2005/2006. As mentioned earlier in this chapter, ensemble member 25S3 misses data for the season of 2001/2002.

Table 4.3.1: The RMSE values (cloud bands) and the corresponding percentage error (%) of the number of cloud bands for the 27 different ensemble members. EM stands for ensemble member. The abbreviations of the ensemble members are presented in Table 3.1. The RMSE and percentage error averages in the last row of the last two columns are the averages for all 27 ensemble members.

EM	RMSE (cloud bands)	Error (%)		EM	RMSE (cloud bands)	Error (%)
1S1	14.05	38.20		1O3	14.18	37.96
1S2	12.96	36.95		9O1	12.53	33.55
1S3	17.62	46.15		9O2	13.13	35.15
9S1	13.94	37.67		9O3	13.82	39.48
9S2	15.95	43.84		17O1	13.07	36.96
9S3	15.36	41.12		17O2	13.29	35.58
17S1	15.28	40.89		17O3	13.04	34.92
17S2	14.11	38.58		25O1	14.88	39.83
17S3	17.59	47.76		25O2	13.50	37.07
25S1	16.24	45.22		25O3	13.49	38.95
25S2	15.37	41.15		1N1	15.81	42.31
25S3	10.94	29.32		1N2	14.23	40.58
1O1	12.82	36.63		1N3	14.29	38.25
1O2	12.50	33.46		**Average**	14.22	38.80

Due to the high RMSE values and the fact that the ensemble members in general under-predict the number of cloud bands, it was decided to apply a bias-adjustment. To apply the bias-adjustment, Equations 2.6 and 2.7 are used.

The newly calculated RMSE values after the bias-adjustment is applied, as well as the accompanying percentage error values, can be found in Table 4.3.2. The average bias-adjusted RMSE calculates to 9.61 cloud bands and the average bias-adjusted percentage error is 26.23%. After the bias is adjusted, the best and worst performers changed. According to the bias-adjusted RMSE values, ensemble member 3 initiated on 17 October (17O3) fared the best with an RMSE of 7.43 cloud bands and an error of 19.9%. Ensemble member 1 initiated on 1 November (1N1) has the highest RMSE (12.36 cloud bands), which results in an error of 33.1%. Both ensemble members 17O3 and 1N1 have no missing data for the entire study period.

Table 4.3.2: The RMSE values (cloud bands) and the percentage error (%) of the number of cloud bands for the 27 different ensemble members after the bias was adjusted. EM stands for ensemble member. The abbreviations of the ensemble members are explained in Table 3.1 on. The RMSE and percentage error averages in the last row of the last two columns are the averages for all 27 ensemble members.

EM	RMSE (cloud bands)	Error (%)		EM	RMSE (cloud bands)	Error (%)
1S1	11.55113	31.40		1O3	8.952254	23.96
1S2	8.429309	24.03		9O1	8.337584	22.32
1S3	11.26833	29.51		9O2	9.284615	24.85
9S1	7.821227	21.14		9O3	9.146484	26.13
9S2	10.23684	28.14		17O1	10.27802	29.07
9S3	9.497852	25.42		17O2	10.21728	27.35
17S1	10.37289	27.77		17O3	7.439552	19.91
17S2	7.535291	20.60		25O1	10.75326	28.79
17S3	10.64297	28.91		25O2	8.995747	24.69
25S1	11.73525	32.67		25O3	8.817017	25.45
25S2	9.238341	24.73		1N1	12.35694	33.08
25S3	7.69769	20.63		1N2	10.26685	29.27
1O1	9.960381	28.46		1N3	9.846008	26.36
1O2	8.822513	23.62		**Average**	9.611171	26.23

Figure 4.3.1 indicates the percentage error of the biased and bias-adjusted versions for the number of cloud bands of the ensemble members. Some ensemble members improved significantly with the bias-adjustment, and others less significantly, for example, ensemble

member 1 initiated on 1 September (1S1) improved only by 6.8%, while ensemble member 1 initiated on 9 September (9S1) improved by 16.5%.

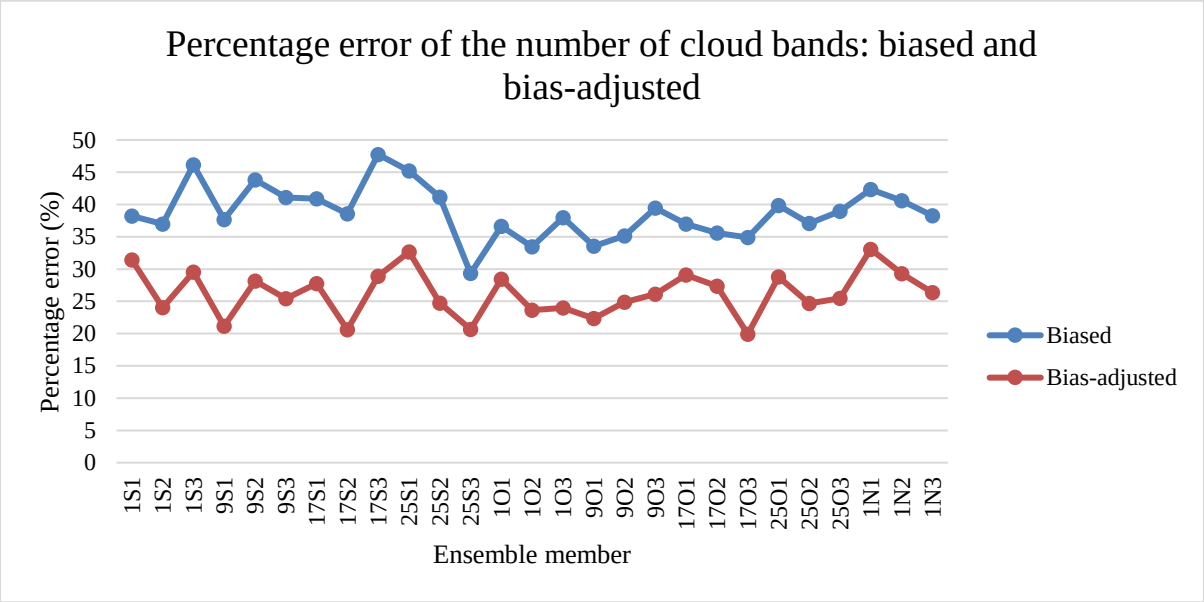

Figure 4.3.1: The percentage error of the cloud bands of the 27 different ensemble members before and after the bias is adjusted. The blue line indicates the percentage error of the raw data, while the red line represents the percentage error after the bias is adjusted. For the abbreviations of the ensemble members, please refer to Table 3.1.

4.4 Synopsis

In this chapter the number of cloud bands simulated by the model is compared to that of the observed dataset. The seasonal average is calculated, as well as the model average over the considered study period. Furthermore, the average percentage deviation of the number of cloud bands for every ensemble member was calculated, as well as the RMSE and the corresponding percentage error. The results (graphs) of the best and worst performing ensemble members are presented. The results of the remaining ensemble members can be found in Appendix A (the results regarding the percentage deviation). The ensemble average (model average) is also calculated for the percentage deviation, the RMSE and the percentage error.

In the next chapter the intensity of the TTT events and include the area, as well as the minimum and the maximum OLR of the cloud bands will be presented.

CHAPTER 5: Intensity of TTTs

This chapter focuses on the intensity of the TTT events (the cloud bands), and include the results regarding the area and the minimum and maximum OLR of the cloud bands. As mentioned in Chapter 3, abbreviations are used for the ensemble members. These abbreviations can be found in Table 3.1.

5.1 Area

This section focuses on the area of the cloud bands, which forms part of the output of the MetBot software. The area of the cloud band is an indication of the intensity of a TTT event, because it plays a role in the number of people affected by it and has an influence on nature. A large cloud band for example will have a greater area of rainfall than a smaller cloud band. Therefore, by looking at the area of the cloud bands, a part of one of the subobjectives (2.c: the intensity of TTT events) of this study is addressed.

5.1.1 Average area

In order to compare the different ensemble members to the observed, the average area is calculated for the entire summer rainfall season (NDJF) and for each ensemble member for the period 1996/1997 to 2009/2010. The same calculations are repeated for the observed dataset. Due to the fact that the objective of this study is to investigate the performance of the model on a seasonal time-scale, only the seasonal averages and the average for the entire period will be discussed, not the monthly average area.

Figure 5.1.1 shows the seasonal average area of the cloud bands in the observed dataset that are flagged by the MetBot. On average, the observed cloud bands have an area of 35841.33km^2. Interesting to note is that the cloud bands in the NDJF season of 1997/1998 has the greatest average area (46 749 km^2) and the cloud bands in 2003/2004 has the smallest average area (31 785 km^2). It is possible that ENSO played a role during these years, because the season of 1997/1998 was an exceptionally wet El Niño season for South Africa, while 2003/2004 was a neutral ENSO year. This will be investigated at a later stage.

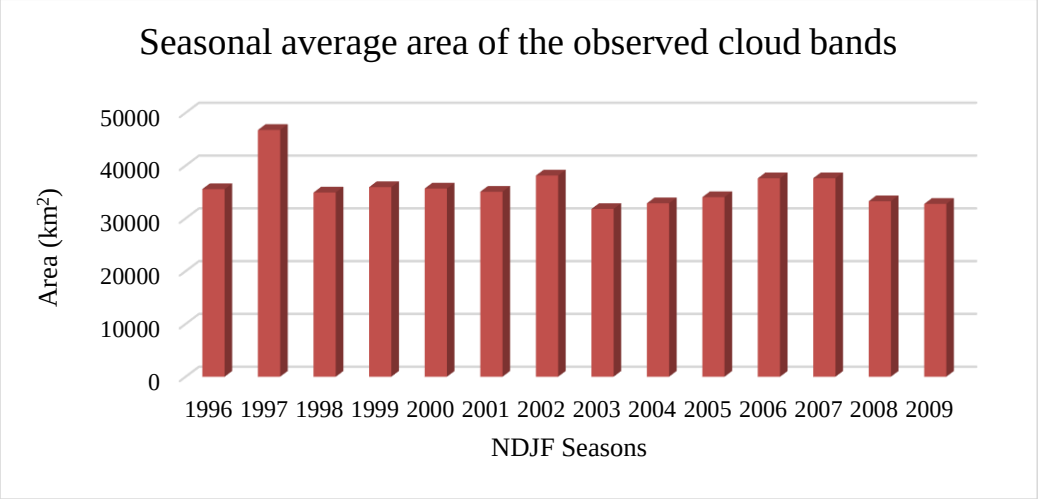

Figure 5.1.1: The seasonal average area in km^2 of the observed cloud bands for the period 1996/1997 to 2009/2010. The area of the cloud bands is averaged for the NDJF season.

In Figure 5.1.2 the average area of the cloud bands modelled by the ensemble members and the corresponding observed average area are displayed. Once again, the ensemble members under-predicted the average area of the cloud bands and it may therefore be necessary to do a bias-adjustment to better determine the performance of the model and its ensemble members. This will be done in a subsequent section. The average of the ensemble members, i.e. the model average for the area of the cloud bands is 29 893 km^2. As discussed in previous chapters, some ensemble members have sections with no data. Due to these periods of missing data, the area of the corresponding observed cloud bands is not the same for every ensemble member. Therefore, the observed average area differs from the "raw" observed cloud bands mentioned earlier in this section. By averaging the area of the corresponding observed cloud bands for every ensemble member, an average area of 35 795 km^2 is obtained.

The difference between the average area of the ensemble members' cloud bands and that of the corresponding observed cloud bands is displayed in Figure 5.1.3. This figure confirms that on average the model under-predicted the cloud band area by 5902 km^2. From Figure 5.1.3 it can be deduced that ensemble member 1S3 was the best performer regarding the average area of the cloud bands with a difference in the average area of 3495 km^2. Ensemble member 1S3 misses data for three seasons (1999/2000, 2002/2003 and 2005/2006). Ensemble member 17S2 fared the worst with a difference of 7323 km^2. Ensemble member 17S2 misses data for the month February of 2005.

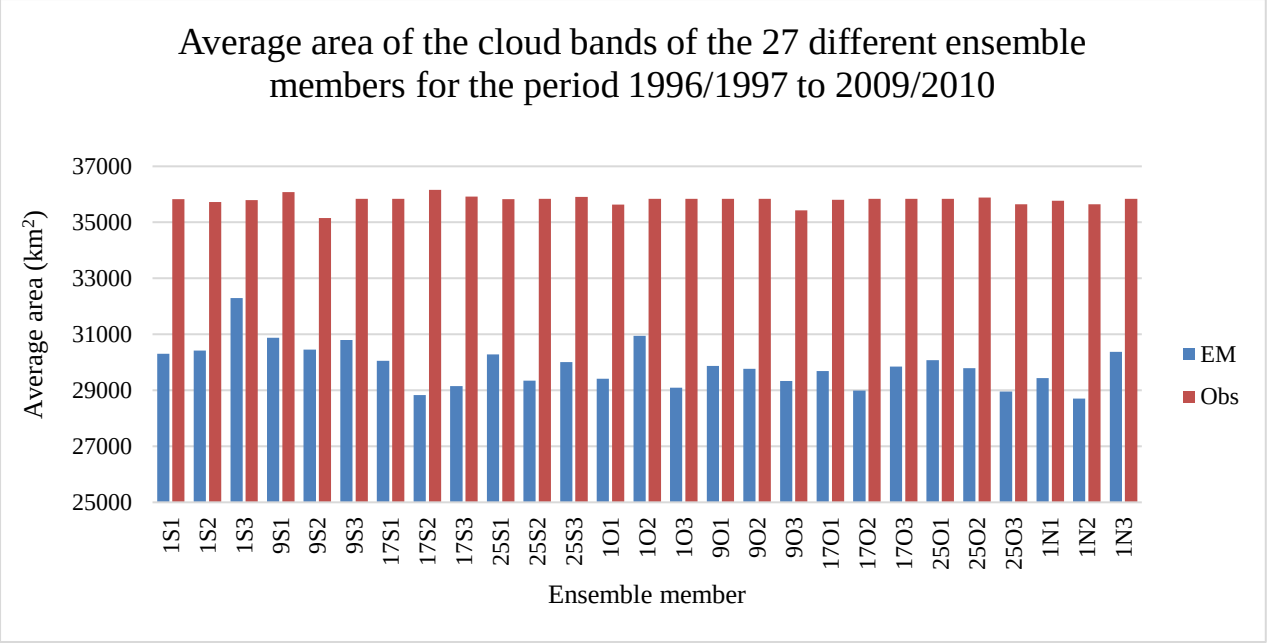

Figure 5.1.2: The average area in km^2 of the cloud bands as flagged by the MetBot for the 27 different ensemble members (in blue) and the corresponding average area of the observed cloud bands (in orange) for the period 1996/1997 to 2009/2010. The area is averaged for the NDJF season, and then for the entire period. For the abbreviations of the ensemble members, please refer to Table 3.1. Observed is abbreviated as Obs and ensemble member as EM in the legend.

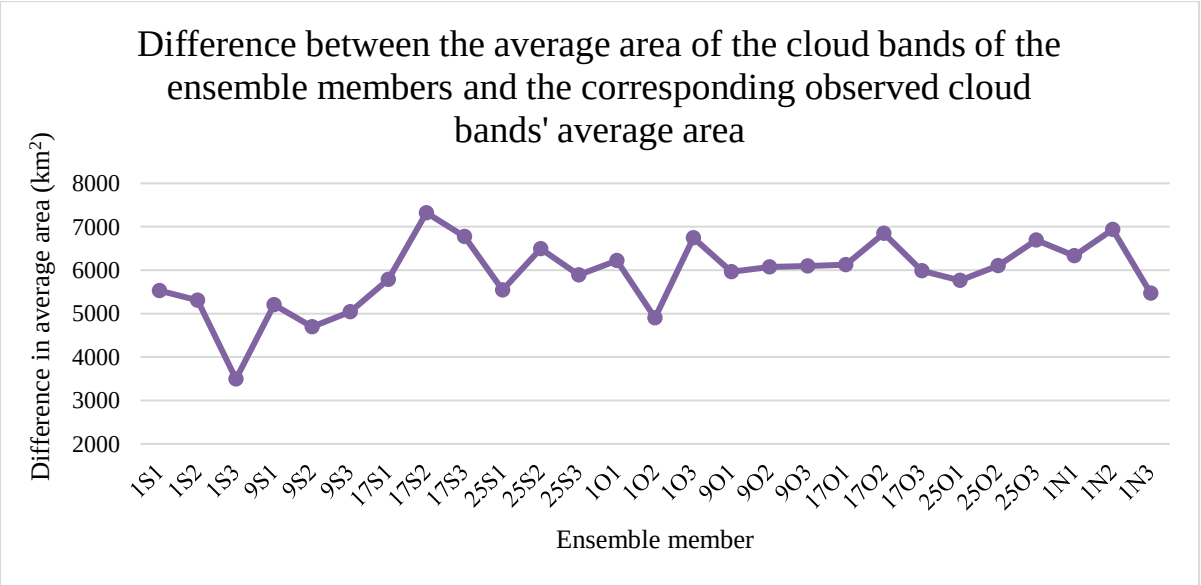

Figure 5.1.3: A graph indicating the difference between the average area of the cloud bands of the 27 different ensemble members and that of the corresponding observed cloud bands in km^2. For the abbreviations of the ensemble members, please refer to Table 3.1.

Figures 5.1.4 and 5.1.5 represent the modelled cloud bands' average areas per season of the worst and best performing ensemble members as discussed in the previous paragraph. A definitive outlier between the observed and the modelled average area is for the season 1997/1998, during which the average observed area is significantly higher than the other seasons in the study period. For ensemble member 1S3 (the best performer) the seasons of 2003/2004, 2004/2005 and 2009/2010 are very close to the average observed area of the cloud bands (the dots on the graph in Figure 5.1.4 almost coincide). The worst performer (ensemble member 17S2) has no seasons with values relatively close to that of the observed. Interesting to note is that both ensemble members over-predicted the average area of the cloud bands for the season 2003/2004 (more on this in Chapter 7).

In the case of ensemble member 1S3 where the data is missing for three entire seasons (1999/2000, 2002/2003 and 2005/2006), the line on the graph is connected from the previous year to the next year with available data. Thus, no interpolation was used during the calculations for the seasons with missing data.

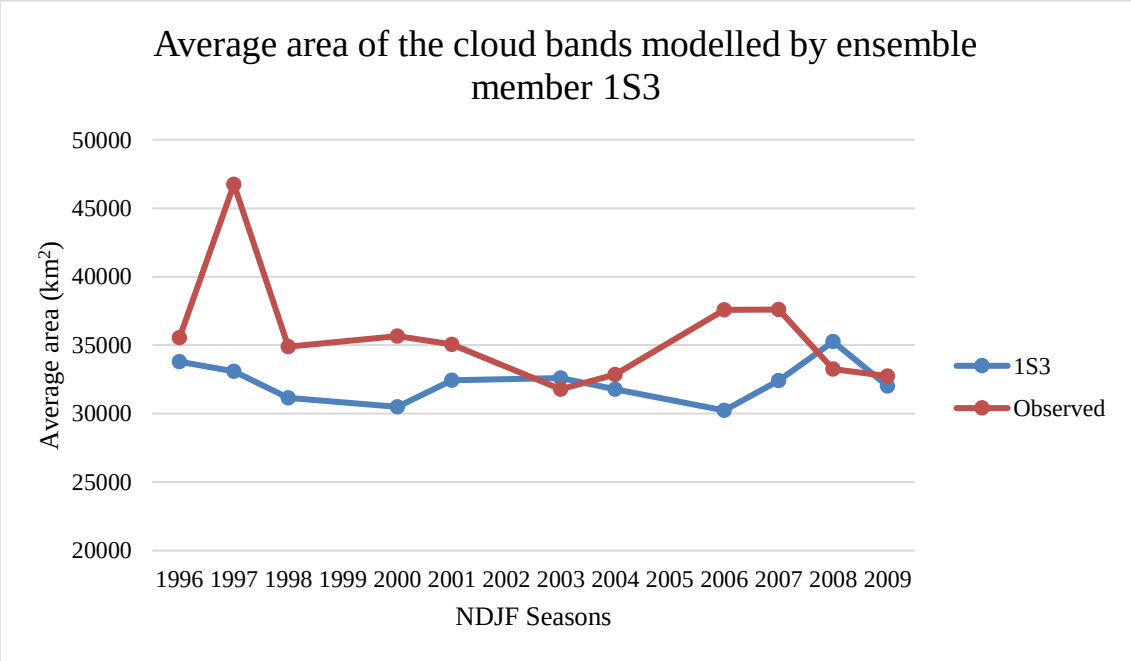

Figure 5.1.4: The average area of the cloud bands for ensemble member 1S3. The x-axis indicates the different seasons in the study period and the y-axis donates the average area in km^2. The blue line represents the average area of the ensemble member and the orange line the average area of the observed dataset.

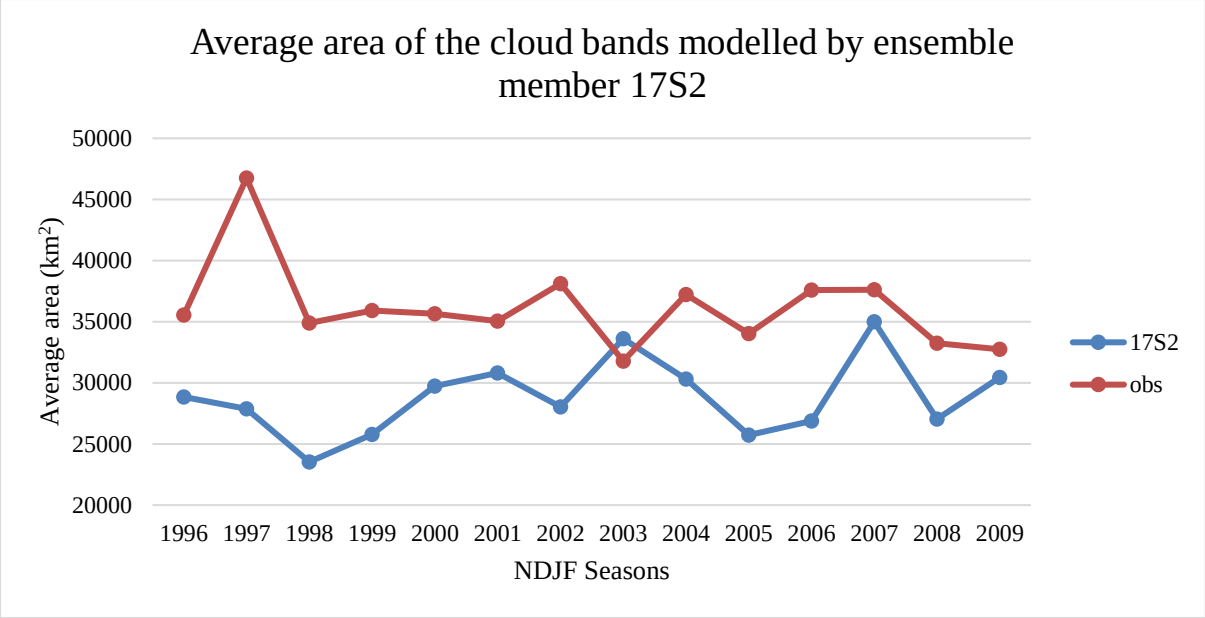

Figure 5.1.5: The average area of the cloud bands for ensemble member 17S2. The x-axis indicates the different seasons in the study period and the y-axis donates the average area in km^2. The blue line represents the average area of the ensemble member and the orange line the average area of the observed dataset. Observed is abbreviated as obs in the legend.

Once again, the average area of the entire study period of the different ensemble members is below the average area of the observed cloud bands. That is not the case when the seasons in this period is considerate separately. Table 5.1.1 lists the years for which each ensemble member over-predicted the average area of the cloud bands. Interesting to note is that 9 of the 27 ensemble members (33.3%) overpredicted the average area of the cloud bands in 2003/2004 (more on this is discussed in chapter 7). In 5 of the 14 seasons in the study period none of the ensemble members over-predicted the average area of the cloud bands.

Table 5.1.1: The NDJF seasons in which the ensemble members over-predict the average area of the cloud bands. 'X' marks a season in which an ensemble member over-predicts the average area of the cloud bands. In the last row, the total number of ensemble members which over-predict the average area of the cloud bands in that particular season, is displayed.

	1996	1997	1998	1999	2000	2001	2002	2003	2004	2005	2006	2007	2008	2009
1S1														
1S2								X		X				
1S3								X					X	
9S1				X				X						
9S2							X							
9S3						X				X				
17S1														
17S2								X						
17S3								X						
25S1														
25S2														
25S3														
1O1														
1O2								X						X
1O3														
9O1								X						
9O2										X				
9O3								X	X					
17O1			X										X	
17O2														
17O3								X						
25O1									X					
25O2									X					
25O3														
1N1									X					
1N2														X
1N3														
Total			**1**	**1**		**1**	**1**	**9**	**4**	**3**			**2**	**2**

5.1.2 Root-mean square error

The root-mean square error (RMSE) and the percentage error for the average area is calculated using Equation 2.4 and 2.5 respectively. This calculation is repeated for all 27 ensemble members.

The RMSE values in km^2 and the percentage error of each ensemble member are presented in Table 5.1.2. The average RMSE of all the ensemble members for the average cloud band area is 7268.43km^2. An average percentage error of 20.31% is obtained. Ensemble member 1S3 yielded the best RMSE value (5430.5km^2) with a percentage error of 15.17%, while ensemble member 17S2 performed the worst with an RMSE of 8753.1km^2 and a percentage error of 24.21%. As mentioned before, ensemble member 1S3 has three years of data missing (1999/2000, 2002/2003, 2005/2006) and ensemble member 17S2 misses the data for February 2005.

Table 5.1.2: The RMSE values in km^2 and the percentage error of the average area of the cloud bands for the different ensemble members. EM stands for ensemble member and the abbreviations of the ensemble members are explained in Table 3.1. The RMSE and percentage error averages in the last row of the last two columns are the averages for all 27 ensemble members.

EM	**RMSE (km^2)**	**Error (%)**		**EM**	**RMSE (km^2)**	**Error (%)**
1S1	6960.83	19.43		1O3	7513.80	20.96
1S2	8004.22	22.41		9O1	6803.20	18.98
1S3	5430.50	15.17		9O2	7016.41	19.58
9S1	6958.18	19.29		9O3	8006.40	22.60
9S2	6498.39	18.49		17O1	7539.85	21.06
9S3	6892.81	19.23		17O2	8139.90	22.71
17S1	7436.14	20.75		17O3	7312.81	20.40
17S2	8753.10	24.21		25O1	6726.83	18.77
17S3	8257.06	22.99		25O2	6891.68	19.20
25S1	6175.10	17.24		25O3	7445.13	20.88
25S2	7560.71	21.09		1N1	7972.91	22.29
25S3	7027.20	19.57		1N2	8266.83	23.19
1O1	7763.73	21.79		1N3	6671.03	18.61
1O2	6222.73	17.36		**Average**	7268.43	20.31

Because the RMSE values are quite high and the fact that the ensemble members in general underpredict the average area of cloud bands, the bias is adjusted. Again Equations 2.6 and 2.7 are used (as in chapter 4) in order to adjust the bias.

Table 5.1.3 shows the new RMSE values in km^2 and the accompanying percentage error after the bias is adjusted. The average bias-adjusted RMSE is $4358.2km^2$ and the average bias-adjusted percentage error is 12.18%. With the bias-adjustment, the average RMSE and the average percentage error is considerably lower. According to the new RMSE values, ensemble member 25S1 fared the best with an RMSE of $2713.41km^2$ and an error of 7.57%. The data of the 2002/2003 season and of the months January and February 2005 are missing for ensemble member 25S1. Ensemble member 9O1 has the highest RMSE value ($6803.2km^2$), which results in a percentage error of 18.98%. No data is missing for ensemble member 9O1.

Table 5.1.3: The RMSE values in km^2 and the percentage error of the average area of the cloud bands for the different ensemble members after the bias was adjusted. EM stands for ensemble member and the abbreviations of the ensemble members are explained in Table 3.1. The RMSE and the percentage error averages in the last row of the last two columns are the averages for all 27 ensemble members.

EM	RMSE (km^2)	Error (%)		EM	RMSE (km^2)	Error (%)
1S1	4231.89	11.81		1O3	3306.82	9.23
1S2	5773.65	16.16		9O1	6803.20	18.98
1S3	4156.73	11.61		9O2	3518.33	9.82
9S1	4619.28	12.80		9O3	5194.25	14.66
9S2	4492.68	12.78		17O1	4397.19	12.28
9S3	4699.75	13.11		17O2	4395.23	12.26
17S1	4666.60	13.02		17O3	4197.54	11.71
17S2	4795.09	13.26		25O1	3469.37	9.68
17S3	4716.71	13.13		25O2	3203.56	8.93
25S1	2713.41	7.57		25O3	3258.15	9.14
25S2	4041.87	11.28		1N1	4846.99	13.55
25S3	3827.84	10.66		1N2	4498.47	12.62
1O1	6220.06	17.45		1N3	3816.29	10.65
1O2	3837.44	10.71		**Average**	4359.20	12.18

Figures 5.1.6 to 5.1.9 display the average area of the cloud bands before and after the bias is adjusted, as well as the corresponding observed average area of the cloud bands for the best and worst performing ensemble members. From these four figures it can be seen that by adjusting the bias, the difference between the RMSE values of the ensemble member and that of the observed decreases. For some ensemble members there are more seasons which are relatively close to the observed values, but for other ensemble members it is the opposite. That is the case for ensemble member 1S3 (Figure 5.1.6) where there are three seasons in the bias

RMSE values which are close to that of the observed, while the bias-adjusted RMSE values only has two seasons which are relatively close to the observed (1998/1999 and 2002/2003). The average error of ensemble member 1S3 decreased from 15.17% to 11.61% after the bias was adjusted. The percentage error of the worst performer of the RMSE values for the average area, ensemble member 17S2, improved from 24.21% to 13.26% after the bias is adjusted.

It is clear that the performance of the ensemble members and the model for the average area of the cloud bands, improves after the bias was adjusted, but as can be deducted from Figures 5.1.6, 5.1.7, 5.1.8 and 5.1.9, there are still some seasons for which the different ensemble members under-predict the average area significantly. For the graphs of the average area of the rest of the ensemble members, please refer to Appendix A.

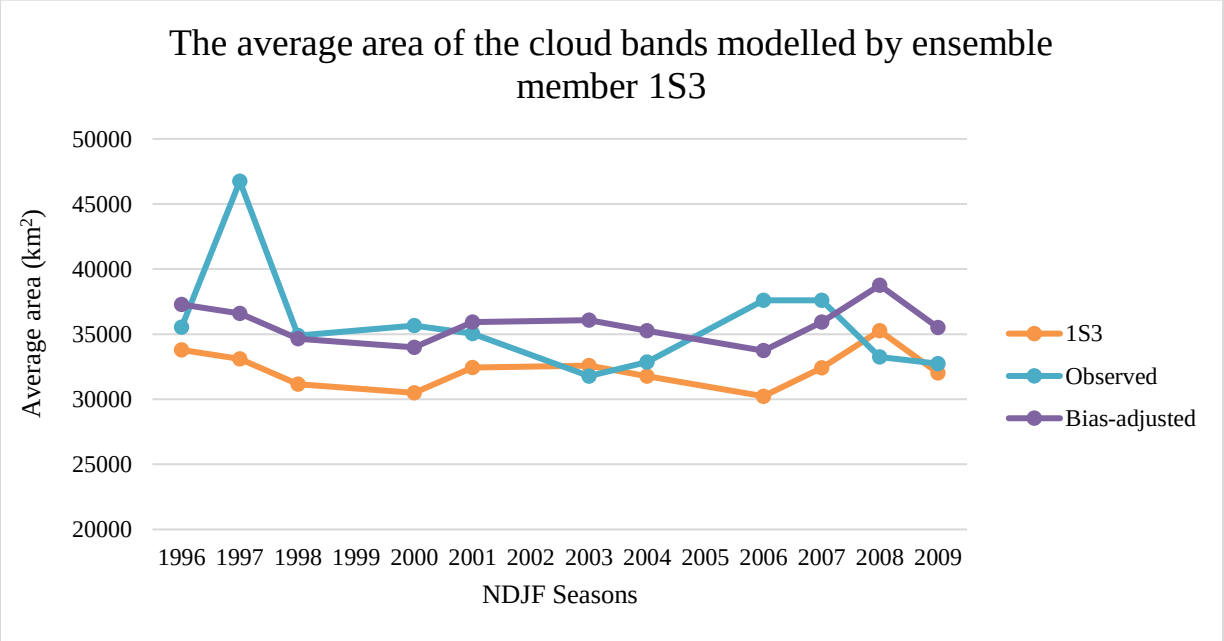

Figure 5.1.6: The average area of the cloud bands for ensemble member 1S3. The x-axis indicates the different seasons in the study period and the y-axis donates the average area in km^2. The green line represents the average area of the ensemble member, the yellow line the bias-adjusted average area of the ensemble member and the blue line the average area of the observed dataset.

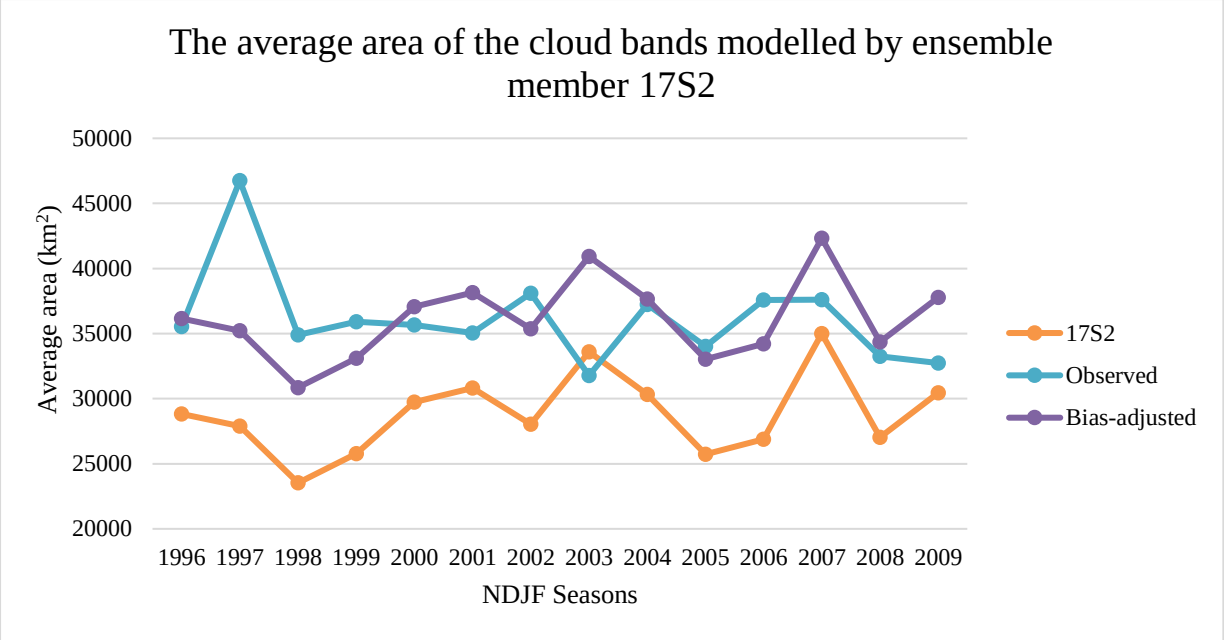

Figure 5.1.7: The average area of the cloud bands for ensemble member 17S2. The x-axis indicates the different seasons in the study period and the y-axis donates the average area in km^2. The green line represents the average area of the ensemble member, the yellow line the bias-adjusted average area of the ensemble member and the blue line the average area of the observed dataset.

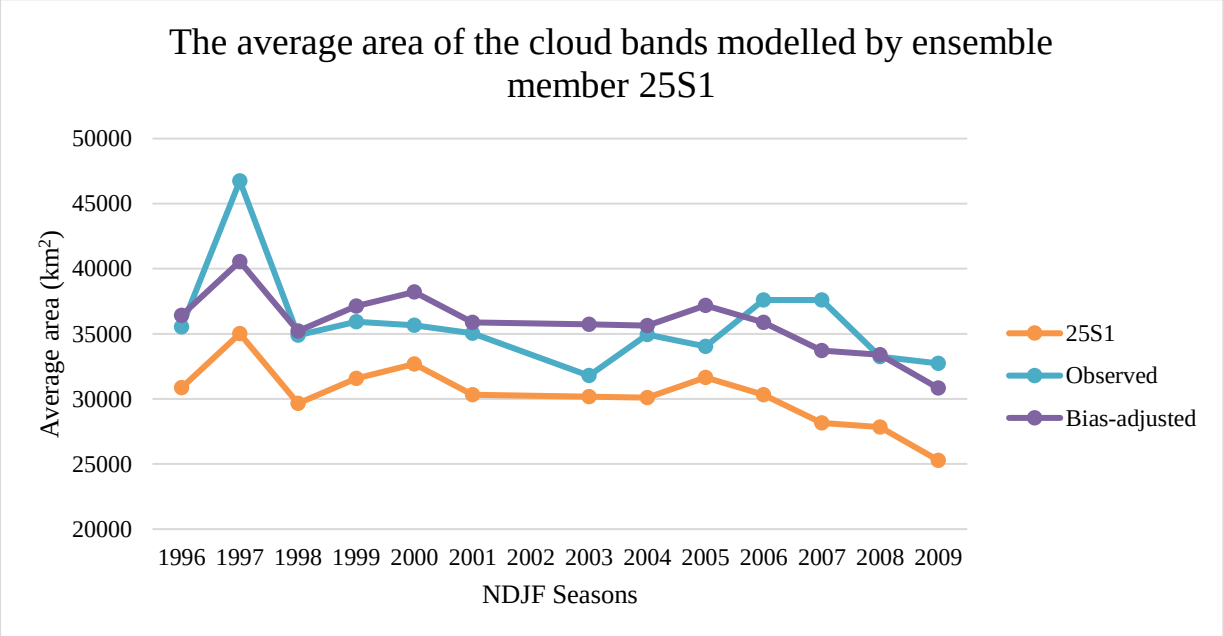

Figure 5.1.8: The average area of the cloud bands for ensemble member 25S1. The x-axis indicates the different seasons in the study period and the y-axis donates the average area in km^2. The green line represents the average area of the ensemble member, the yellow line the bias-adjusted average area of the ensemble member and the blue line the average area of the observed dataset.

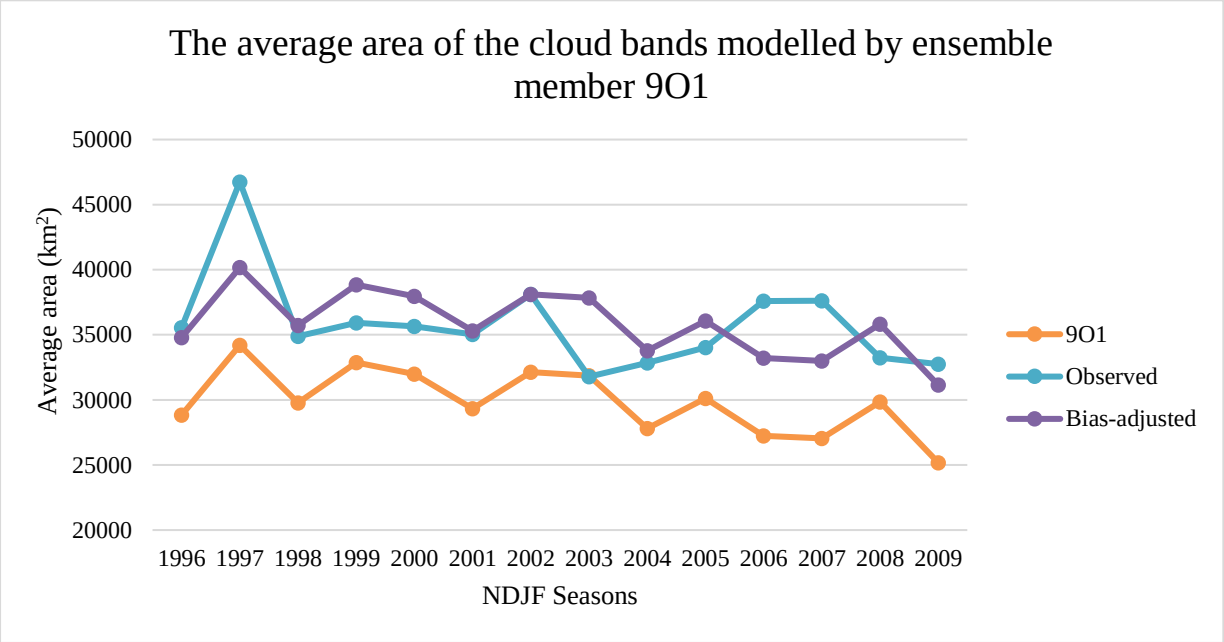

Figure 5.1.9: The average area of the cloud bands for ensemble member 9O1. The x-axis indicates the different seasons in the study period and the y-axis donates the average area in km^2. The green line represents the average area of the ensemble member, the yellow line the bias-adjusted average area of the ensemble member and the blue line the average area of the observed dataset.

5.2 Outgoing longwave radiation

Outgoing longwave radiation (OLR) is the energy emitted by the earth's surface due to the warming of the sun, which is also referred to as terrestrial radiation. The earth emits radiation all the time, but most of the radiation is emitted at night. Due to the great variability in diurnal and nocturnal radiation, daily mean OLR values are used in this study. The OLR is used as input data for the MetBot in order to identify candidate cloud bands. As part of the output, the minimum and maximum OLR values of each candidate cloud band are obtained. During clear skies and particularly clear skies at night, the earth emits more radiation than during overcast skies. Therefore, OLR can be used to identify cloud bands. The lower the OLR values, the thicker the clouds are (a thicker cloud will "trap" more radiation underneath it). Thicker and denser clouds indicate more precipitable water, which can lead to more rain on the ground. This relates to the intensity of a TTT event or a cloud band. Therefore, the minimum and maximum OLR values of the cloud bands can be used to determine the intensity of the cloud band and inevitably the TTT event as well.

One of the criteria the MetBot uses to flag a cloud band is for a blob to have OLR values less than 240 $W.m^{-2}$. Therefore, most of the minimum and maximum OLR values of a cloud band will be less than 240 $W.m^{-2}$. Sometimes it does happen that the maximum OLR values are greater than 240 $W.m^{-2}$. This is possible if part of the blob, which is detected as a cloud band, has a gap somewhere which will allow more OLR to pass through. In the end however, most of the gridded OLR values should be below 240 $W.m^{-2}$.

This section is divided in two subsections: OLR minimum and OLR maximum. Each section comprises of subsections, which focus on the average OLR values (minimum and maximum respectively), as well as the RMSE values and their associated percentage error.

5.2.1 Minimum OLR

The minimum OLR value indicates the least amount of outgoing radiation from the earth's surface that passes through a cloud band. Therefore, it can be concluded that the part where the least amount of radiation passes through, is the thickest part of the cloud band. This relates directly to the intensity of the cloud band, thus also the convective nature of the cloud band and the amount of precipitable water contained within the cloud.

5.2.1.1 Average minimum OLR

Figure 5.2.1 indicates the average minimum OLR values for every NDJF season of the observed dataset for the years 1996/1997 to 2009/2010. These values vary between 128.43 $W.m^{-2}$ in 1999 and 140.78 $W.m^{-2}$ in 2003. On average an observed cloud band has a minimum OLR value of 135.78 $W.m^{-2}$. As mentioned in the previous sections, the observed dataset for each ensemble member varies due to the fact that the data is not complete for every ensemble member.

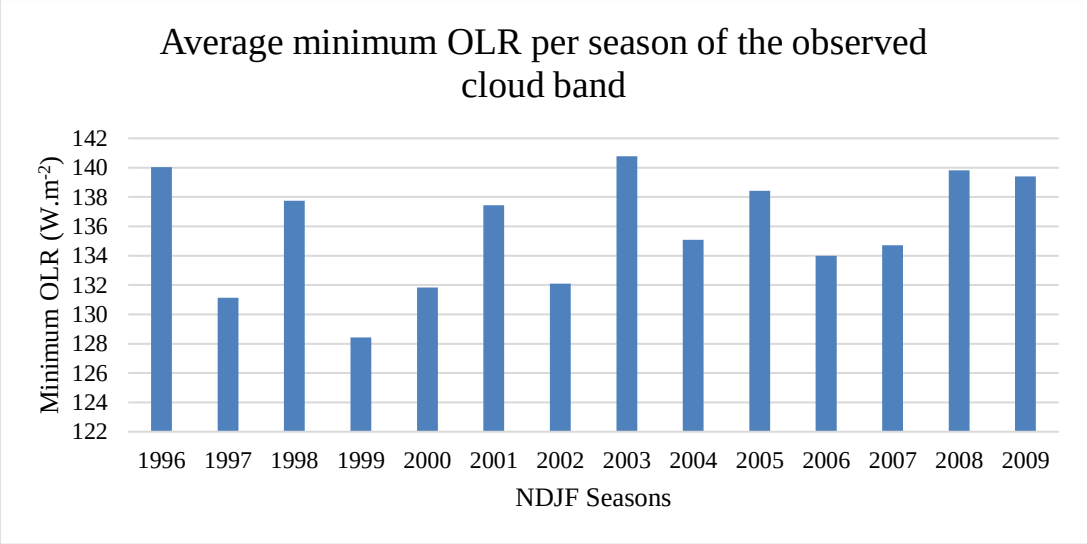

Figure 5.2.1: The average minimum OLR values in W.m^{-2} per season of the observed dataset for the NDJF seasons of 1996/1997 to 2009/2010.

Figure 5.2.2 depicts the average minimum OLR values per season of each ensemble member and the corresponding observed average minimum OLR values averaged over the study period. From the figure it can be deduced that the ensemble members in general under-predict the minimum OLR values. The only ensemble member which just slightly over-predicts the average minimum OLR value is ensemble member 17O1. The average minimum OLR value for ensemble member 17O1 is 136.49W.m^{-2} and the matching observed value is 136.31W.m^{-2}. Ensemble member 17O1 does not have data for the months December 2001, January 2002 and February 2002. The worst performer is ensemble member 1S3 with a value of 128.42 W.m^{-2}, which corresponds to an average observed value of 136.54 W.m^{-2}. Ensemble member 1S3 misses data for three NDJF seasons, namely 1999/ 2000, 2002/2003 and 2005/2006. The model average calculates to 132.99 W.m^{-2}.

To better establish the best and worst performers of the ensemble members when considering the average minimum OLR, the difference between the average minimum OLR values of each ensemble member and the corresponding observed value is calculated by using Equation 5.1: D indicates the difference between the ensemble member and the corresponding observed value, x_o is the ensemble member's specific average observed minimum OLR value and x_m is the average minimum OLR value of the considered ensemble member:

$$D = x_o - x_m \tag{5.1}$$

Thereafter the results are plotted and from this figure (Fig. 5.2.3) the best and worst performing ensemble members as discussed in the previous paragraph are confirmed.

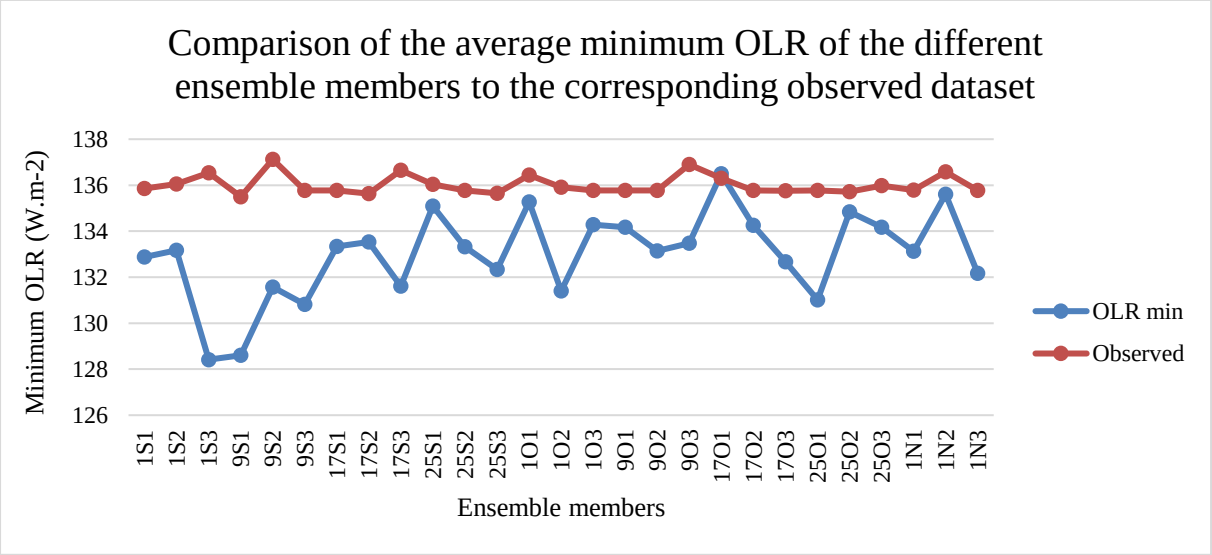

Figure 5.2.2: The average minimum OLR values per season of the 27 ensemble members and the corresponding observed dataset in $W.m^{-2}$ averaged for the NDJF seasons of 1996/1997 to 2009/2010. For the abbreviations of the ensemble members, please refer to Table 3.1.

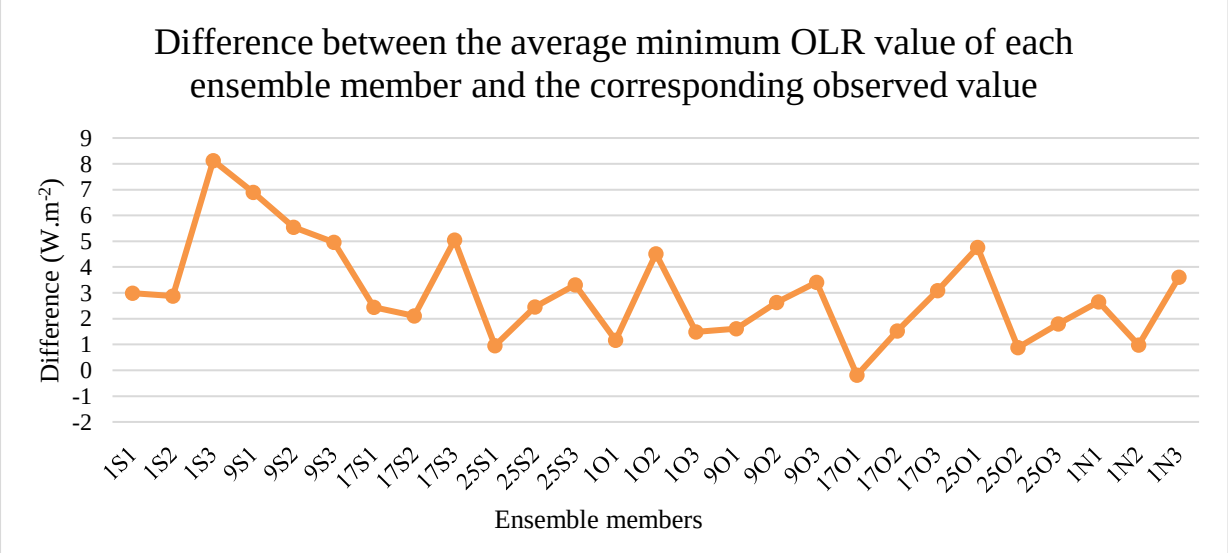

Figure 5.2.3: The difference between the average minimum OLR value per season in $W.m^{-2}$ for the NDJF seasons of 1996/1997 to 2009/2010 of every ensemble member and the corresponding observed value. For the abbreviations of the ensemble members, please refer to Table 3.1.

Figures 5.2.4 and 5.2.5 show the worst and the best performers of the ensemble members regarding the average minimum OLR value of the modelled cloud bands to that of the observed cloud bands, respectively. The year-to-year variability of ensemble member 1S3 is completely different to that of the corresponding observed dataset, especially towards the latter part of the study period (from season 2002/2003 onwards). There are also sections of data missing for this specific ensemble member. These sections are the complete seasons of 1999/2000, 2002/2003 and 2005/2006. Ensemble member 17O1 has missing data for the months December, January and February of 2001/2002. In Figure 5.2.5 it can be seen that the difference is in general less between the average minimum OLR values of the ensemble member (17O1) and that of the observed dataset. Even though there are a few outliers (1998/1999, 2002/2003 and 2008/2009), the year-to-year variation is closer to that of the observed dataset, compared to ensemble member 1S3 (Fig. 5.2.4).

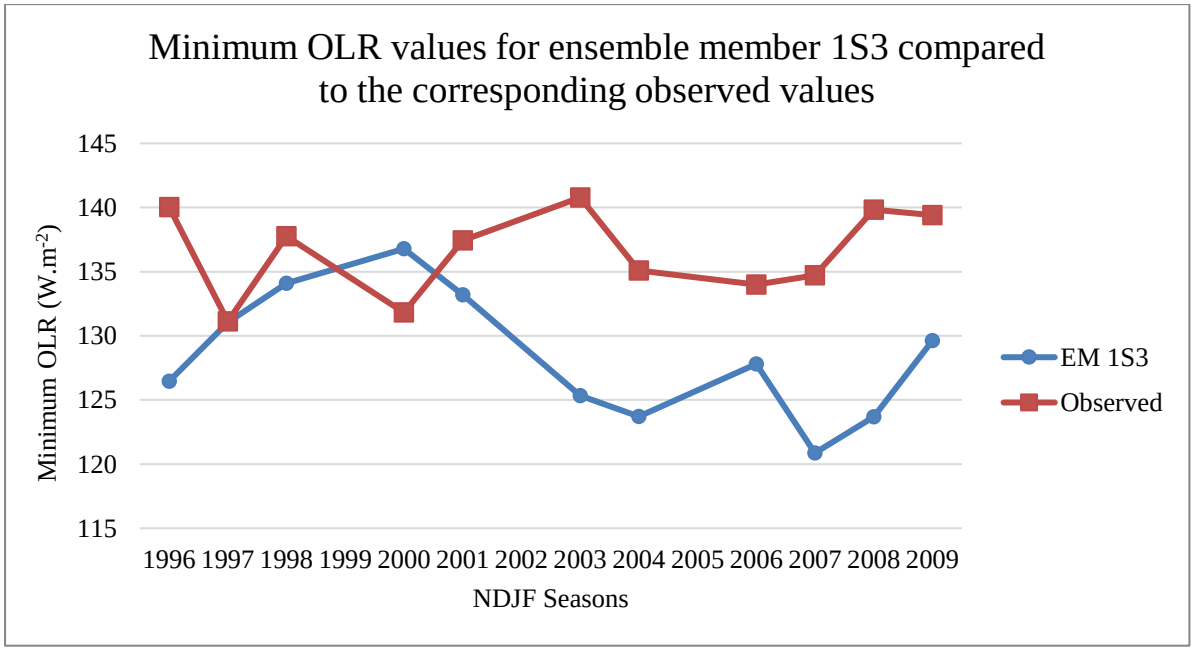

Figure 5.2.4: The minimum OLR value in $W.m^{-2}$ per season for the NDJF seasons of 1996/1997 to 2009/2010 of ensemble member 1S3 and the corresponding observed values. The blue line depicts the values of the ensemble member and the orange that of the observed dataset.

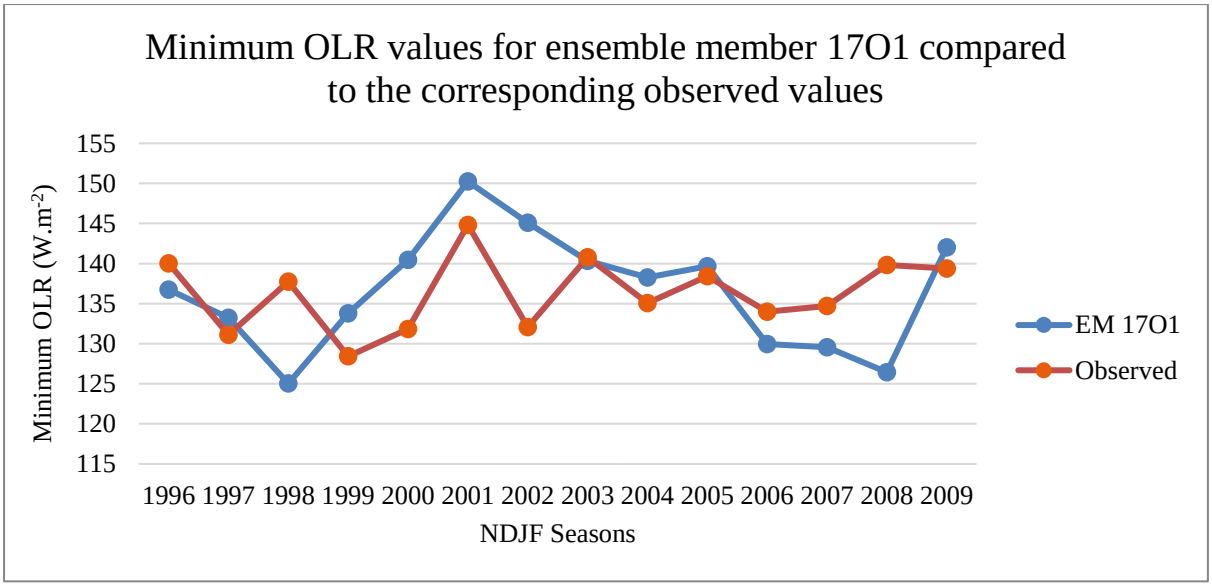

Figure 5.2.5: The minimum OLR value in $W.m^{-2}$ per season for the NDJF seasons of 1996/1997 to 2009/2010 of ensemble member 17O1 and the corresponding observed values. The blue line depicts the values of the ensemble member and the orange that of the observed dataset.

5.1.1.2 Root-Mean Square Error

By using equation 2.4 once again, the root-mean square error (RMSE) is calculated for the minimum OLR. The percentage error is also calculated for the minimum OLR by using Equation 2.5.

Table 5.2.1 lists the RMSE values of each ensemble member for the minimum OLR of each NDJF season of the years 1996/1997 to 2009/2010. The average minimum OLR of all 27 ensemble members came to 7.09 $W.m^{-2}$, which yielded an average percentage error of 5.20%. From the table it can be seen that ensemble member 17O3 has the lowest RMSE value (4.75$W.m^{-2}$, which yields a percentage error of 3.49%) and ensemble member 1S3 has the highest RMSE value (10.76 $W.m^{-2}$, which yields a percentage error of 7.63%). Ensemble member 17O3 has no missing data and as mentioned before, ensemble member 1S3 has no data for the years 1999/2000, 2002/2003 and 2005/2006.

Table 5.2.1: The RMSE values in $W.m^{-2}$ and the percentage error of the minimum OLR values of the cloud bands for the different ensemble members. EM stands for ensemble member and the abbreviations of the ensemble members can be found in Table 3.1. The RMSE and the percentage error averages in the last row of the last two columns are the averages for all 27 ensemble members.

EM	RMSE ($W.m^{-2}$)	Error (%)		EM	RMSE ($W.m^{-2}$)	Error (%)
1S1	6.26	4.60		1O3	5.14	3.78
1S2	8.62	6.33		9O1	5.68	4.17
1S3	10.76	7.87		9O2	7.21	5.30
9S1	9.65	7.11		9O3	6.27	4.57
9S2	9.51	6.92		17O1	6.83	5.00
9S3	8.17	6.00		17O2	5.50	4.04
17S1	6.95	5.11		17O3	4.75	3.49
17S2	9.16	6.74		25O1	6.54	4.81
17S3	9.08	6.64		25O2	5.38	3.95
25S1	5.94	4.35		25O3	5.01	3.68
25S2	7.99	5.87		1N1	6.73	4.95
25S3	6.51	4.79		1N2	8.32	6.08
1O1	6.18	4.52		1N3	7.11	5.22
1O2	6.15	4.52		**Average**	7.09	5.20

In Figures 5.2.6 and 5.2.7 the minimum OLR values are displayed of the best and the worst performing ensemble members when considering the RMSE values for the minimum OLR. There is a significant difference in the year-to-year variability of ensemble member 17O3 compared to that of the observed (Fig. 5.2.6) for the first few seasons of the study period. For the last few seasons (from 2005/2006 to 2009/2010) this variation between the forecast OLR values of ensemble member 17O3 and the OLR values of the observed cloud bands is improved. For the years 1997/1998, 1998/1999 and 2000/2001 to 2004/2005 ensemble member 17O3 under-estimates the average minimum OLR, in which case a bias-adjustment can be considered. For ensemble member 1S3 and that of the corresponding observed data set, there is a definitive difference, especially from the season of 2003/2004 till 2009/2010. There is not a clear relationship between the minimum OLR of ensemble member 1S3 and that of the corresponding observed dataset.

Due to the fact that the minimum OLR of the ensemble members yield an RMSE below 10 in all but one case and an average percentage error of 5.20%, a bias-adjustment is not necessary.

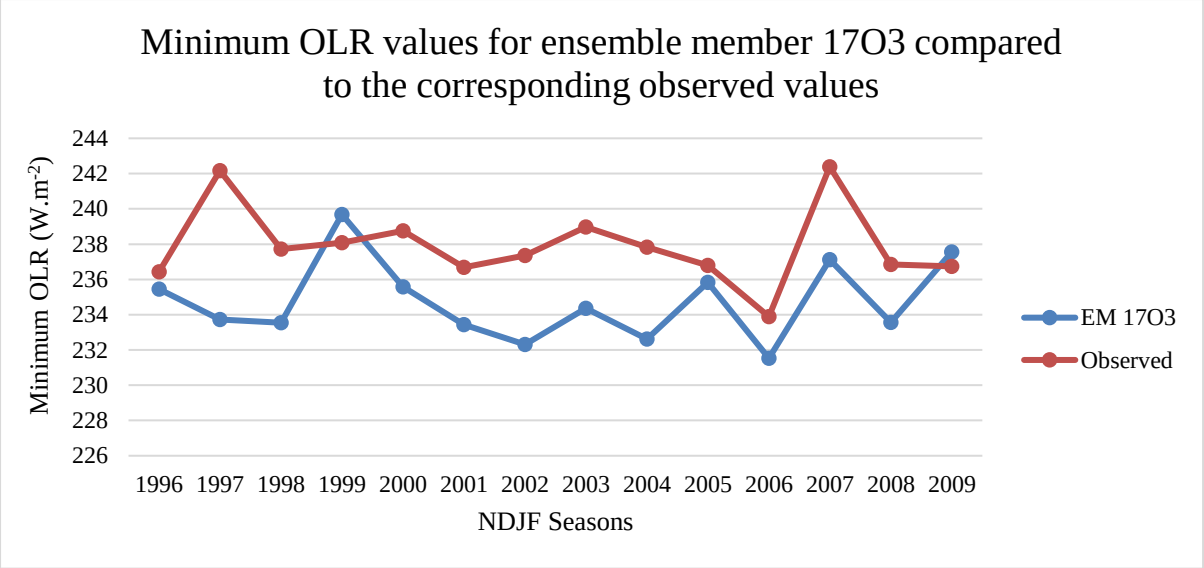

Figure 5.2.6: The minimum OLR value in $W.m^{-2}$ per season for the NDJF seasons of 1996/1997 to 2009/2010 of ensemble member 17O3 and the corresponding observed values. The blue line depicts the values of the ensemble member and the orange that of the observed dataset.

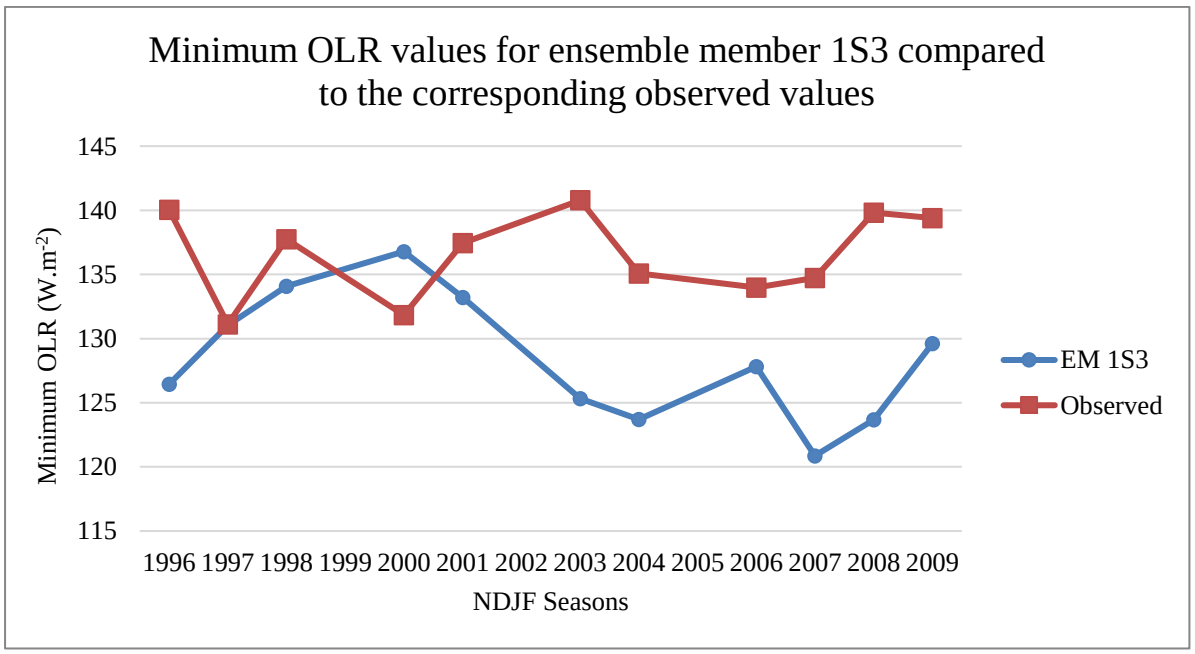

Figure 5.2.7: The minimum OLR value in $W.m^{-2}$ per season for the NDJF seasons of 1996/1997 to 2009/2010 of ensemble member 1S3 and the corresponding observed values. The blue line depicts the values of the ensemble member and the orange that of the observed dataset.

5.2.2 Maximum OLR

Every cloud band has a minimum and a maximum OLR value, which is part of the output of the MetBot. The maximum OLR value is usually below 240 $W.m^{-2}$, because of the criteria used by the MetBot to flag the cloud bands. The maximum OLR is an indication of the thinnest and least dense part of the cloud band. The thinner the cloud band, the less rain it can produce.

5.2.2.1 Average maximum OLR

The average maximum OLR values for every season from 1996/1997 to 2009/2010 for the observed dataset is displayed in Figure 5.2.8. These values vary between 233.89 $W.m^{-2}$ and 242.39 $W.m^{-2}$. There are two seasons with average values above the 240 $W.m^{-2}$ threshold. As mentioned before, this is not entirely impossible, but will be discussed in more detail in Chapter 7. The observed cloud bands have on average a maximum OLR value of 237.9 $W.m^{-2}$. For the ensemble members that does not have a complete dataset in the considered study period, the corresponding observed average maximum OLR value will differ.

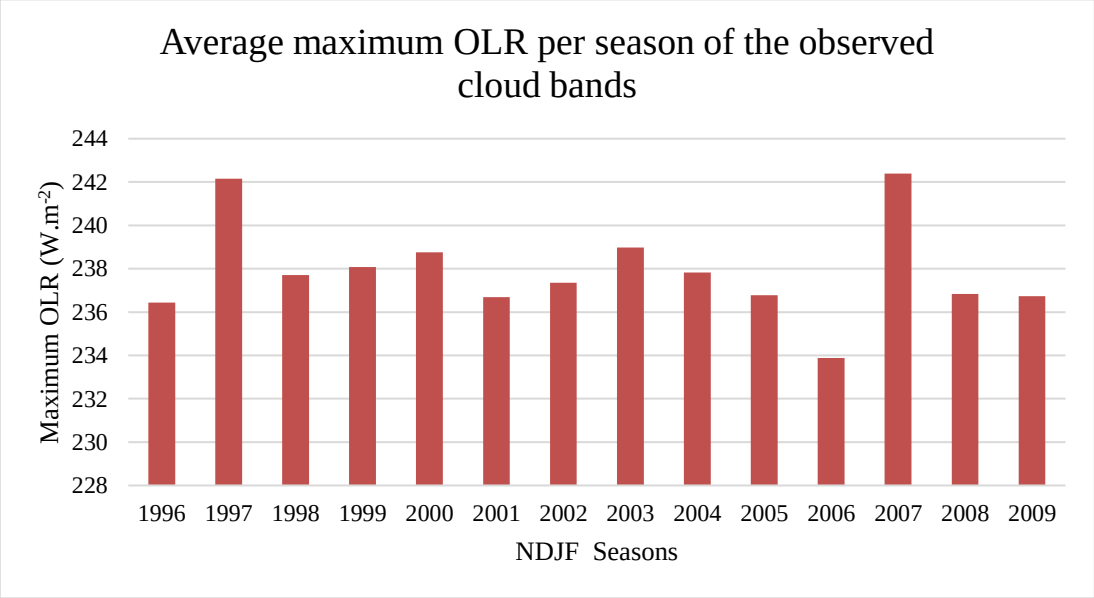

Figure 5.2.8: The average maximum OLR values in $W.m^{-2}$ per season of the observed dataset for the NDJF seasons of 1996/1997 to 2009/2010.

In Figure 5.2.9, the average maximum OLR per season in the study period of each ensemble member is compared to the corresponding observed average maximum OLR values. Once again it is the case that the values of the different ensemble members are lower than that of the observed. Only ensemble member 9S3 over-estimates the maximum OLR. Also notable is that the observed maximum OLR oscillates around 238 $W.m^{-2}$, however it is not that strange

considering that the maximum threshold for a cloud band is 240 W.m^{-2}. The fact that the ensemble members are well below the threshold can indicate that the model in general over-estimates the thickness of the clouds within the cloud bands.

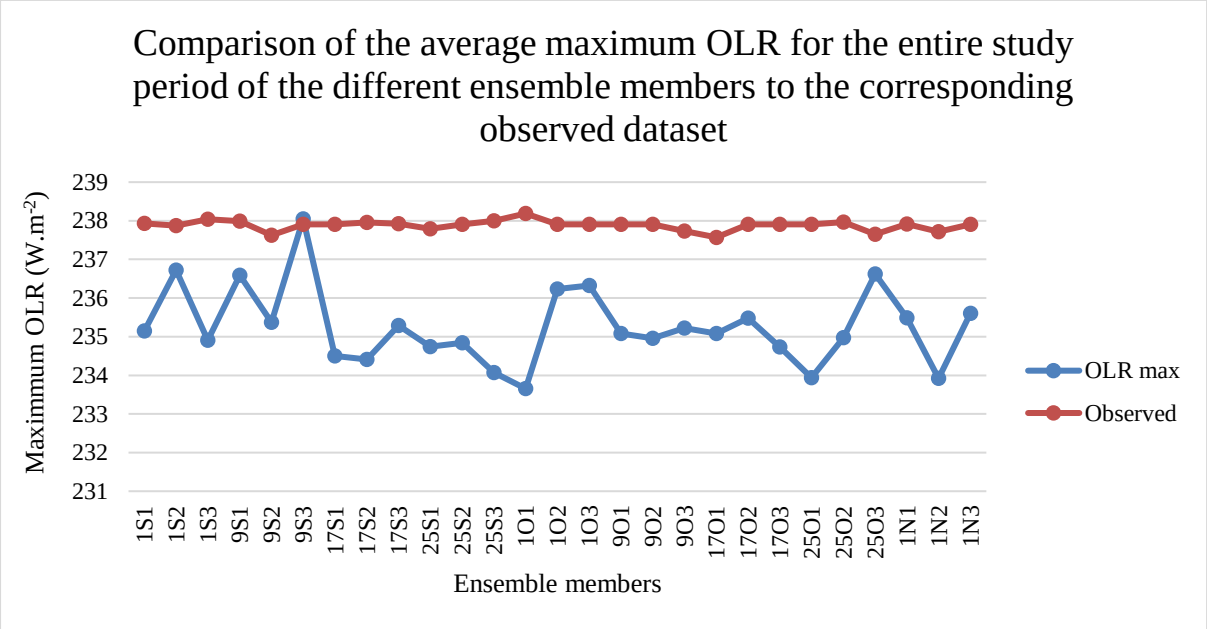

Figure 5.2.9: The average maximum OLR values for the entire study period (1996/1997 to 2009/2010) of the ensemble members (blue line) compared to that of the corresponding observed dataset (orange line) in W.m^{-2}.

From Figure 5.2.9, it can be deduced that ensemble member 9S3 is the best performer and ensemble member 1O1 the worst. The average maximum OLR for ensemble member 9S3 is 238.05 W.m^{-2} and the corresponding observed value is 237.9 W.m^{-2}. Ensemble member 9S3 does not have any missing data. Ensemble member 1O1 produces an average maximum OLR of 233.65 W.m^{-2} with a corresponding observed value of 238.19 W.m^{-2}. Ensemble member 1O1 misses data for the months December 2004, January 2005 and February 2005.

The difference between the average maximum OLR of the ensemble members and the corresponding observed values is displayed in Figure 5.2.10. To calculate the difference, the simple Equation of 5.1 is used.

In Figure 5.2.10, the best and worst performers can perhaps be better distinguished than in Figure 5.2.9. Ensemble member 9S3 has a difference of -0.14 W.m^{-2} with the corresponding average observed maximum OLR value (the minus indicates an over-estimation). The worst

performer, ensemble member 1O1, differs by +4.53 W.m^{-2} with the corresponding average observed maximum OLR value (the plus indicates an under-estimation). On average, the model calculated the maximum OLR per cloud band as 235.26 W.m^{-2}, which is of course less than the observed, but not significantly.

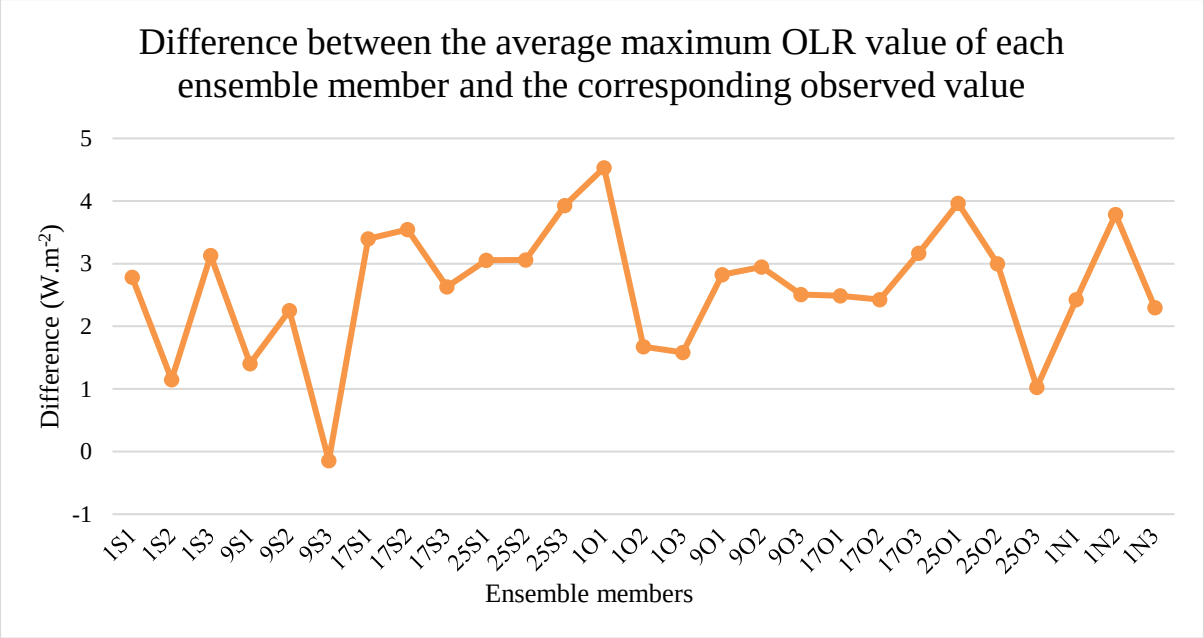

Figure 5.2.10: The difference between the average maximum OLR value per season in W.m^{-2} for the NDJF seasons of 1996/1997 to 2009/2010 of every ensemble member and the corresponding observed value. For the abbreviations of the ensemble members, please refer to Table 3.1.

The best and the worst performing ensemble members, when considering the average maximum OLR, are displayed in Figures 5.2.11 and 5.2.12. Ensemble member 9S3 (Fig. 5.2.11) follows more or less the same variability as that of the observed dataset. For the years 2001, 2005 and 2006 the ensemble member showed a decrease instead of an increase from the previous year as was the case with the observed data. Even though there is a decreasing variability from 2004 to 2005 for the average maximum OLR of the model, the value for 2005 differs by 0.13 W.m^{-2} to that of the model. This translates to a 0.05% percentage error, which is extremely low in comparison with the rest of the data. The worst performer (ensemble member 1O1) follows the same decrease and increase variability of the observed data for the first few seasons. From the 2002/2003 season however, the variability is completely different. For the seasons 2001/2002 and 2006/2007, the ensemble member's average maximum OLR is very close to that of the observed dataset (a percentage error of 0.39% and -0.29% respectively).

In general, the average maximum OLR of ensemble member 9S3 is closer to that of the observed dataset than the average maximum OLR of ensemble member 1O1.

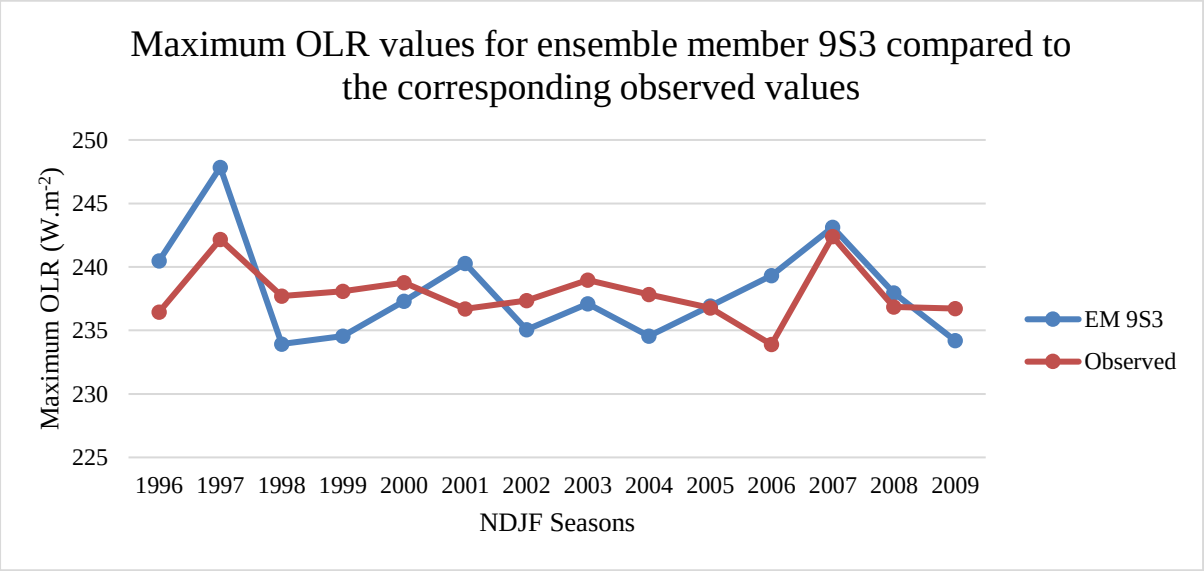

Figure 5.2.11: The maximum OLR value in $W.m^{-2}$ per season for the NDJF seasons of 1996/1997 to 2009/2010 of ensemble member 9S3 and the corresponding observed values. The blue line depicts the values of the ensemble member and the orange that of the observed dataset.

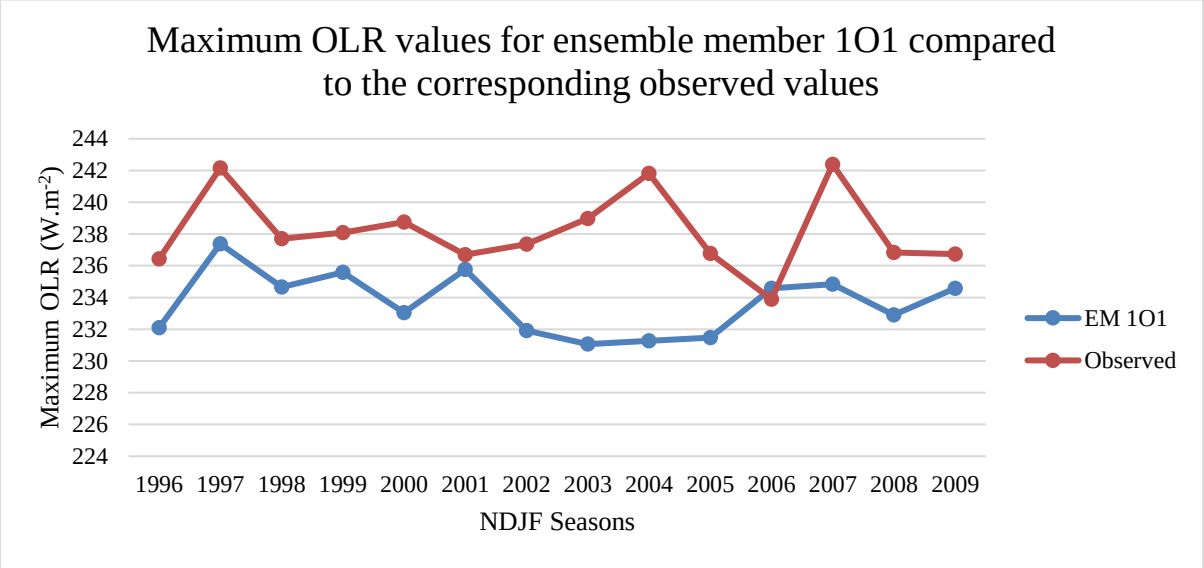

Figure 5.2.12: The maximum OLR value per season in $W.m^{-2}$ for the NDJF seasons of 1996/1997 to 2009/2010 of ensemble member 1O1 and the corresponding observed values. The blue line depicts the values of the ensemble member and the orange that of the observed dataset.

5.2.2.2 Root-Mean Square Error

Next the root-mean square error (RMSE) of the average maximum OLR is calculated for all 27 ensemble members using Equation 2.4. After the RMSE is calculated, the percentage error (PE) is also calculated by using Equation 2.5.

Table 5.2.2 lists the RMSE values in $W.m^{-2}$ of the average maximum OLR of the 27 different ensemble members, as well as the corresponding percentage error. The average RMSE for all 27 ensemble members is 4.53 $W.m^{-2}$ which results in a percentage error of 1.90%. From the table above, it can be seen that ensemble member 17S3 yields the highest RMSE value (6.11 $W.m^{-2}$) with a corresponding percentage error of 2.57% and ensemble member 9S3 yields the lowest RMSE value (3.42 $W.m^{-2}$) with a corresponding percentage error of 1.44%. Ensemble member 17S3 has three years of data missing, namely 1999/2000, 2000/2001 and 2001/2002, while ensemble member 9S3 has no missing data. Interesting to note is that ensemble member 9S3 is also the best performer in the previous section (the section on the average maximum OLR values).

Table 5.2.2: The RMSE values in $W.m^{-2}$ and the percentage error of the maximum OLR values of the cloud bands for the 27 different ensemble members. EM stands for ensemble member and the abbreviations of the ensemble members can be found in Table 3.1. The RMSE and the percentage error averages in the last row of the last two columns are the averages for all 27 ensemble members.

EM	RMSE ($W.m^{-2}$)	Error (%)		EM	RMSE ($W.m^{-2}$)	Error (%)
1S1	4.26	1.79		1O3	3.90	1.64
1S2	4.74	1.99		9O1	4.63	1.95
1S3	5.91	2.48		9O2	4.46	1.88
9S1	4.58	1.92		9O3	4.64	1.95
9S2	3.92	1.65		17O1	3.55	1.49
9S3	3.42	1.44		17O2	3.60	1.51
17S1	4.84	2.03		17O3	4.19	1.76
17S2	4.71	1.98		25O1	5.67	2.38
17S3	6.11	2.57		25O2	4.39	1.84
25S1	4.59	1.93		25O3	4.40	1.85
25S2	4.34	1.82		1N1	4.12	1.73
25S3	4.87	2.05		1N2	4.67	1.96
1O1	5.46	2.29		1N3	4.56	1.92
1O2	3.83	1.61		**Average**	4.53	1.90

In Figure 5.2.13, the average maximum OLR per season of ensemble member 17S3, the ensemble member with the highest RMSE, is displayed. The average maximum OLR of the seasons 1997/1998, 2007/2008 and 2009/2010 are significantly different than that of corresponding observed values. There is no model data available for the three seasons 1999/2000 to 2001/2002. The average maximum OLR values of the three seasons of 2003/2004 to 2005/2006 differ very little from that of the corresponding observed values and the average maximum OLR for the season of 2008/2009 only differs by 0.47% (1.12 $W.m^{-2}$). It is possible that the large section of missing data has an influence on the average performance of this ensemble member.

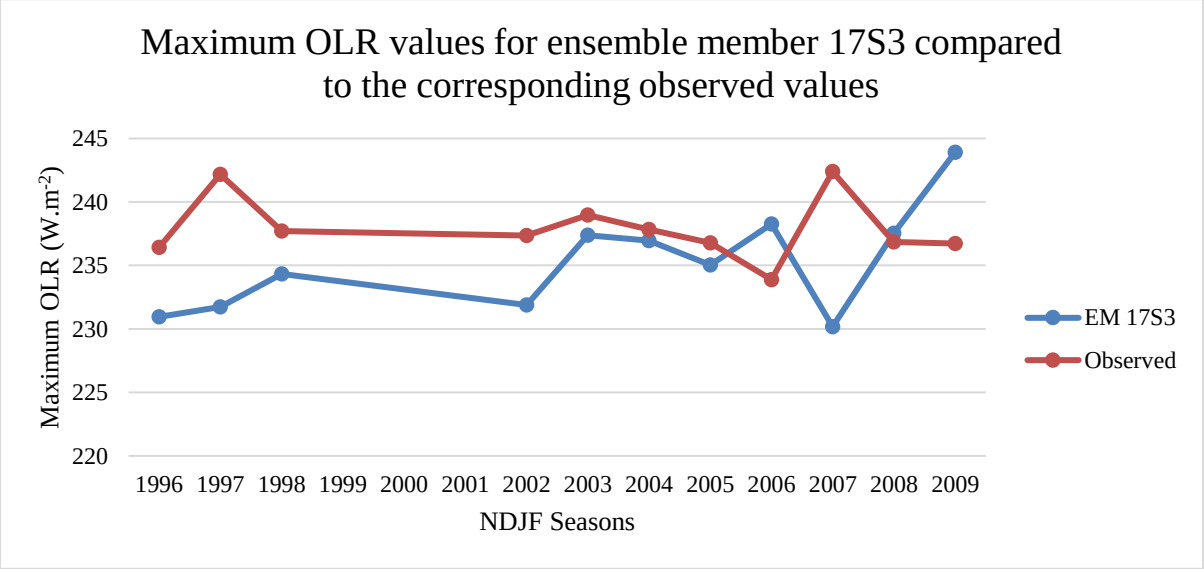

Figure 5.2.13: The maximum OLR value in $W.m^{-2}$ per season for the NDJF seasons of 1996/1997 to 2009/2010 of ensemble member 17S3 (blue line) and the corresponding observed values (orange line).

Figure 5.2.14 is almost the perfect example of a good performing ensemble member where the results of the ensemble member is in close agreement to that of the observed, in this case ensemble member 9S3. The general year-to-year variability of increasing or decreasing from one season to the next is very close to that of the corresponding observation dataset. The only outliers are the seasons of 2001/2002, 2005/2006 and 2006/2007. Both the average maximum OLR of ensemble member 9S3 and that of the observed dataset decreased from season 2008/2009 to 2009/2010, but the ensemble member decreases more than that of the observed dataset.

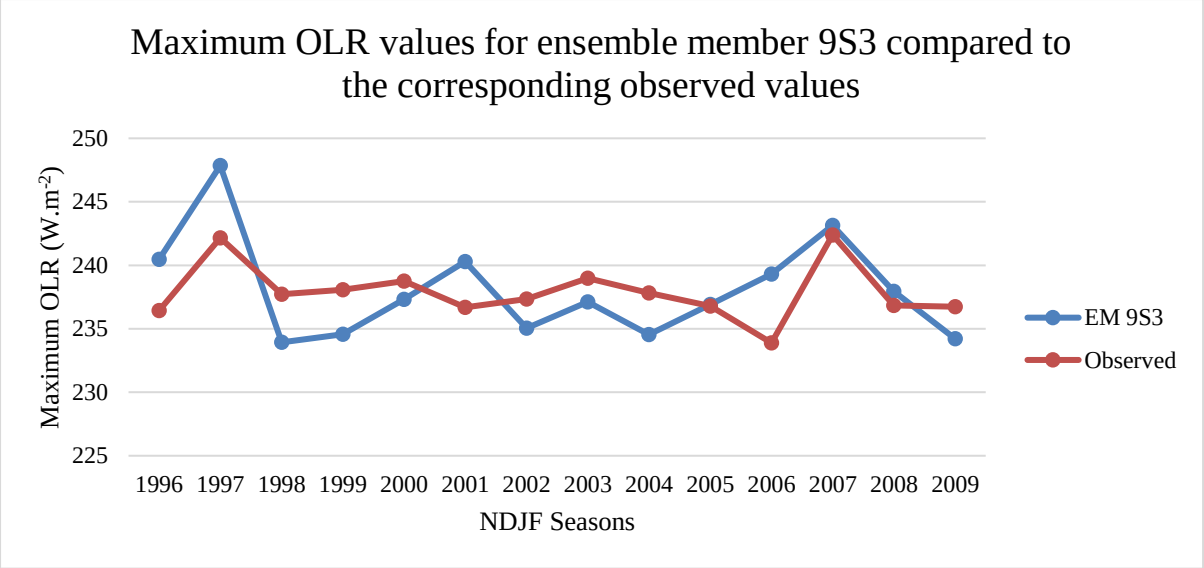

Figure 5.2.14: The maximum OLR value in $W.m^{-2}$ per season for the NDJF seasons of 1996/1997 to 2009/2010 of ensemble member 9S3 (blue line) and the corresponding observed values (orange line).

As in the case with the average minimum OLR values of the ensemble members, the RMSE and corresponding percentage errors are also very low for the average maximum OLR values. Therefore, it is decided not to adjust the bias.

5.3 Synopsis

This part of the results focuses on the intensity of the TTT events by looking at the area and the minimum and maximum OLR of the cloud bands. These variables of the modelled cloud bands are compared to that of the observed cloud bands by means of calculating the averages (seasonal average per ensemble member) and the model average (over the entire study period). Furthermore, the RMSE values and the corresponding percentage error are calculated. Thereafter, the graphs of the best and worst performing ensemble members are presented.

In the next chapter (the final chapter on the results of this study), the results regarding the location of the TTTs are presented. These results include the anchor point, the position of the centroid and the tilt of the cloud bands.

CHAPTER 6: Location of TTTs

Part 4 of the results focuses mainly on the location of the cloud bands and therefore also the location of the TTTs. This chapter consists of the analysis of the anchor points, the position of the centroid and the tilt of the cloud bands. As mentioned in Chapter 3, abbreviations are used for the ensemble members. These abbreviations can be found in Table 3.1.

6.1 Cloud band anchor point

The north-western most point of the cloud band is considered as the anchor point of the cloud band. The point can also be referred to as the root of the cloud band and has a specific longitude and latitude. These coordinates are located within the study area (geographical domain) that forms part of the criteria for the MetBot to identify cloud bands. The geographical domain was discussed in Chapter 2 Section 2.5 and displayed in Figure 2.3. The geographical domain extends from 5°S to 50°S and from 5°E to 80°E.

In Figure 6.1.1 the anchor points of all the observed cloud bands (as flagged by the MetBot) for the NDJF seasons of 1996/1997 to 2009/2010 are displayed by the red dots. Some cloud bands have exactly the same anchor points. Therefore, one red dot can represent multiple anchor points. The most of the cloud bands have their roots somewhere above Namibia and Angola between 5˚E and 21˚E. The second most anchor points fall within the region above Madagascar. Very few cloud bands start in the region above Zimbabwe/Mozambique. From Figure 6.1.1, the gridded nature of the data is clearly visible.

Due to the large geographical domain, cloud bands can originate in many different places with very different coordinates. It was found that the latitude of the anchor point of most of the modelled cloud bands is more or less consistent with those of the observed, but the longitude varies quite substantially. These differences in the latitudes between the modelled and the observed cloud bands resulted in large RMSE values and therefore also large percentage errors. It was therefore decided to rather use a graphical approach instead of a statistical approach to evaluate the performance of the ensemble members. However, first the original results will be

shown and briefly discussed to illustrate the issue faced with the anchor points of the cloud bands. Thereafter, the graphical results will be presented.

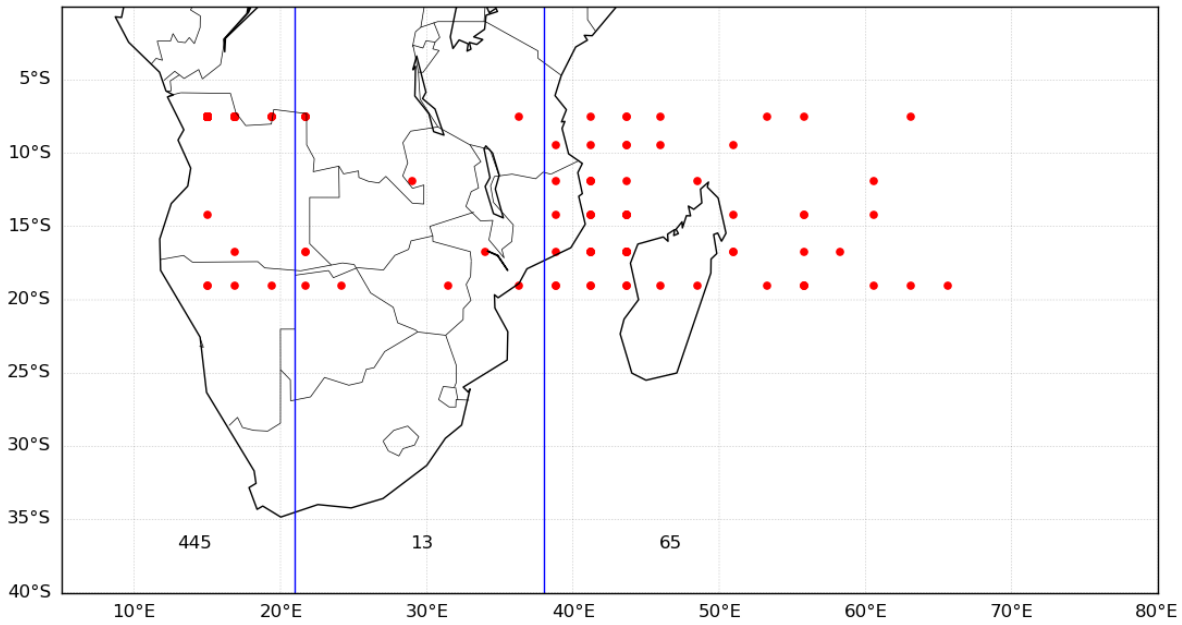

Figure 6.1.1: The anchor points of the observed cloud bands as flagged by the MetBot for the NDJF seasons of the years 1996/1997 to 2009/2010. The red dots indicate the anchor points. Each red dot can represent more than one anchor point, i.e. more than one cloud band. The blue lines divide the geographical domain in the three preferred regions where TTTs tend to develop. At the bottom of these three regions (columns), the number of cloud bands within that region is displayed (around 35˚S).

The geographical domain is divided in the following three sections based on the longitude of the anchor points: cloud bands with anchor points to the west of 21˚E (region 1), between 21˚E and 38˚E (region 2) and to the east of 38˚E (region 3). These three regions cover the three areas where the cloud bands have been found to have their roots, i.e. the first region is above and around Namibia up to the western and north-western parts of Botswana, the second above Zimbabwe, Mozambique and part of the Mozambican Channel, and the third stretches from above Madagascar to the Southern Indian Ocean.

Another challenge in evaluating the anchor point of the cloud bands is that there are quite a few seasons in the observed dataset as well as the modelled data where there are no cloud bands within specific regions. This lack of cloud bands within specific seasons influenced the average coordinates of the cloud bands significantly, which is a result when a no-cloud band season is

considered as 0, which is falsely registered as coordinates of 0˚S, 0˚E. One option is perhaps to discard the years without any modelled or observed cloud bands. However, there are so many years, especially in Region 2, where either the ensemble member does not model cloud bands or there are no cloud bands observed in this specific area, a large section of the data in the study period would then have to be disregarded.

In the three figures above (Fig. 6.1.2, 6.1.3 and 6.1.4) the dilemma that is faced with the coordinates of the cloud bands' anchor points, can be seen. Figure 6.1.2 represents region 1 (cloud bands with longitudes up to 20˚E) of ensemble member 1S1, as well as the corresponding observed longitudes for the study period. From this figure it can be seen that this specific ensemble member tends to model the cloud bands slightly farther east than what is observed. For region 2 (Fig. 6.1.3) ensemble member 1S1 performs well for 6 of the 14 seasons (1997/1998, 1999/2000, 2002/2003, 2003/2004, 2005/2006 and 2006/2007), but not for the rest of the study period. Especially the years where either the ensemble member does not forecast cloud bands or there are no cloud bands observed in region 2. For region 3 (Fig. 6.1.4) the ensemble member performed really well, except again for the two seasons where ensemble member 1S1 forecast cloud bands, while there are no observed cloud bands (1996/1997 and 2006/2007).

These three figures (Fig. 6.1.2 to 6.1.4) only represent one of the 27 ensemble members, but this dilemma is faced with most of the ensemble members, especially in region 2. This "dilemma" results in high RMSE values, which are displayed in the Table 6.1.1, 6.1.2 and 6.1.3. Ensemble member 1S1 is chosen randomly to illustrate this particular dilemma that is faced with most of the ensemble members.

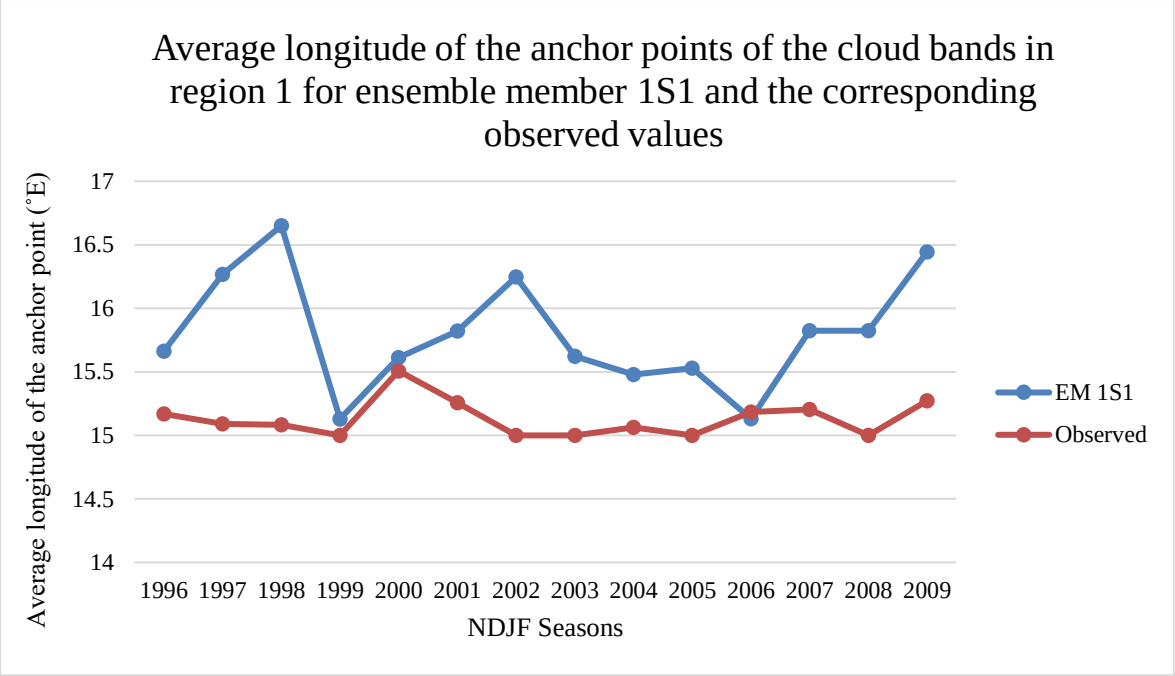

Figure 6.1.2: The average longitude of the cloud bands' anchor points in region 1 as modelled by ensemble member 1S1 (blue line) and the corresponding observed values (orange line) for the study period 1996/1997 to 2009/2010.

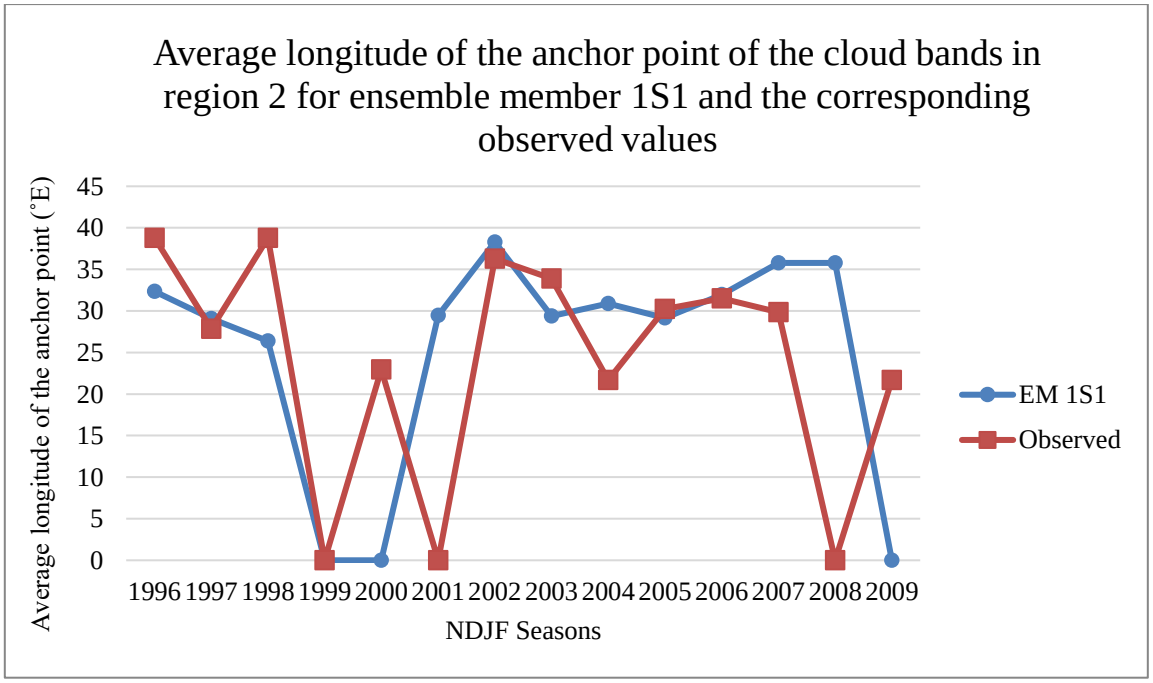

Figure 6.1.3: The average longitude of the cloud bands' anchor points in region 2 as modelled by ensemble member 1S1 (blue line) and the corresponding observed values (orange line) for the study period 1996/1997 to 2009/2010.

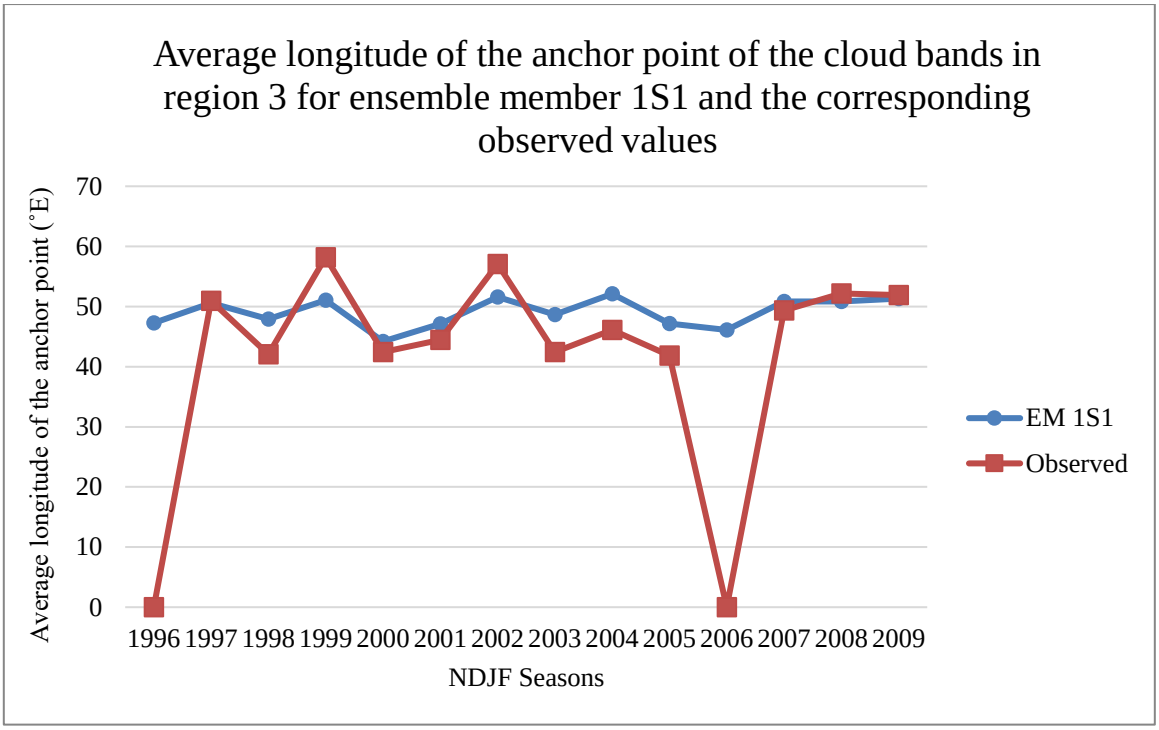

Figure 6.1.4: The average longitude of the cloud bands' anchor points in region 3 as modelled by ensemble member 1S1 (blue line) and the corresponding observed values (orange line) for the study period 1996/1997 to 2009/2010.

Table 6.1.1: The RMSE values in degrees east (˚E) and the percentage error of the anchor point of the cloud bands in region 1 for the 27 different ensemble members. EM stands for ensemble member and the abbreviations of the ensemble members can be found in table 3.1. The RMSE and the percentage error averages in the last row of the last two columns are the averages for all 27 ensemble members.

EM	**RMSE (˚E)**	**Error (%)**		**EM**	**RMSE (˚E)**	**Error (%)**
1S1	0.78	5.13		1O3	0.67	4.45
1S2	0.72	4.76		9O1	0.67	4.43
1S3	0.62	4.09		9O2	0.65	4.32
9S1	0.83	5.52		9O3	1.00	6.59
9S2	0.88	5.78		17O1	0.75	4.92
9S3	0.85	5.59		17O2	0.86	5.66
17S1	0.60	3.99		17O3	0.86	5.71
17S2	0.61	4.01		25O1	0.80	5.26
17S3	0.72	4.75		25O2	0.69	4.55
25S1	0.54	3.55		25O3	0.95	6.25
25S2	0.85	5.61		1N1	0.82	5.39
25S3	0.75	4.96		1N2	0.72	4.73
1O1	0.77	5.10		1N3	0.78	5.15
1O2	0.54	3.55		**Average**	0.75	4.96

Table 6.1.2: The RMSE values in degrees east (˚E) and the percentage error of the anchor point of the cloud bands in region 2 for the 27 different ensemble members. EM stands for ensemble member and the abbreviations of the ensemble members can be found in table 3.1. The RMSE and the percentage error averages in the last row of the last two columns are the averages for all 27 ensemble members.

EM	**RMSE (˚E)**	**Error (%)**		**EM**	**RMSE (˚E)**	**Error (%)**
1S1	14.74	61.86		1O3	15.67	66.67
1S2	22.51	87.74		9O1	17.49	74.40
1S3	18.45	76.01		9O2	19.17	81.54
9S1	11.54	48.81		9O3	13.89	66.96
9S2	17.81	79.05		17O1	16.80	71.45
9S3	19.09	81.21		17O2	18.99	80.80
17S1	14.81	67.43		17O3	18.03	76.71
17S2	16.95	77.21		25O1	16.86	71.73
17S3	18.72	67.25		25O2	19.69	83.75
25S1	18.16	87.08		25O3	15.56	75.03
25S2	19.29	87.84		1N1	20.87	88.77
25S3	17.83	75.41		1N2	16.29	78.56
1O1	16.90	82.82		1N3	17.16	73.00
1O2	20.16	85.75		**Average**	17.53	76.11

Table 6.1.3: The RMSE values in degrees east (˚E) and the percentage error of the anchor point of the cloud bands in region 3 for the 27 different ensemble members. EM stands for ensemble member. The abbreviations of the ensemble members can be found in Table 3.1. The RMSE and the percentage error averages in the last row of the last two columns are the averages for all 27 ensemble members.

EM	**RMSE (˚E)**	**Error (%)**		**EM**	**RMSE (˚E)**	**Error (%)**
1S1	22.79	55.13		1O3	20.62	50.08
1S2	23.98	59.17		9O1	19.18	46.59
1S3	19.93	51.97		9O2	19.65	47.72
9S1	25.78	63.80		9O3	19.09	46.56
9S2	19.43	49.40		17O1	23.57	62.05
9S3	18.60	45.19		17O2	19.52	47.43
17S1	24.95	60.77		17O3	23.39	56.82
17S2	20.83	50.89		25O1	19.96	48.50
17S3	22.53	57.48		25O2	20.52	49.89
25S1	20.59	51.79		25O3	23.37	61.24
25S2	17.84	43.45		1N1	19.55	47.49
25S3	20.42	50.06		1N2	24.92	60.51
1O1	22.96	56.15		1N3	18.60	45.19
1O2	17.36	42.18		**Average**	21.11	52.13

The average RMSE and the percentage error of the anchor point of the cloud bands in region 1 of the 27 ensemble members are 0.75˚ and 4.96% respectively. For region 2 these values are calculated as 17.53˚ and 76.11% and for region 3 as 21.11˚ and 52.13%. The values for region 1 are not as high as the other two regions, which could be due to the number of cloud bands simulated with their roots in and around Namibia, as well as the longitudinal dimension of region 1 that is narrower than the other two regions, in particular that of region 3. Regions 2 and 3 could have such a high percentage error due to the lack of cloud bands in these areas during some of the seasons, and due to the geographical extend of these two regions.

Due to the high RMSE values and the high percentage errors, as well as the dilemma discussed earlier in this section, it is decided to rather use a visual presentation to compare the anchor points of the modelled and the observed cloud bands.

In figures 6.1.5, 6.1.6 and 6.1.7 the anchor points of three of the ensemble members (1S1, 1O1 and 1N1) are displayed. These ensemble members are chosen randomly to illustrate the visual display of the anchor points of the modelled cloud bands. For the rest of the ensemble members, please refer to Appendix B. The red dots in the figures represent the anchor points of the cloud bands. One such a dot can represent more than one cloud band. The blue lines divide the study domain in the three regions where TTTs tend to develop. At the bottom of these regions the number of cloud bands with anchor points within that particular region is displayed. From the figures, as well as the other ensemble members not shown here, it is clear that most of the modelled cloud bands tend to develop in the first region, the second most in region 3 and the least in region 2. This is also the case with the observed cloud bands (fig. 6.1.1).

The gridded nature of the data can be seen in figures 6.1.5 to 6.1.7, as is the case with the observed data in figure 6.1.1. Also evident in these figures is the difference in the resolution of the different datasets: the ensemble members have a finer resolution than the observed dataset. Due to the lack of cloud bands in the second region, it might be sensible to divide the geographical domain in two regions instead of three, with the border between the two regions around 30˚E, which can be considered in a follow-up study. The division of the domain at 30˚E will accommodate the extension of TTT events over the landmass and the adjacent Southwest Indian Ocean (Harrison, 1984).

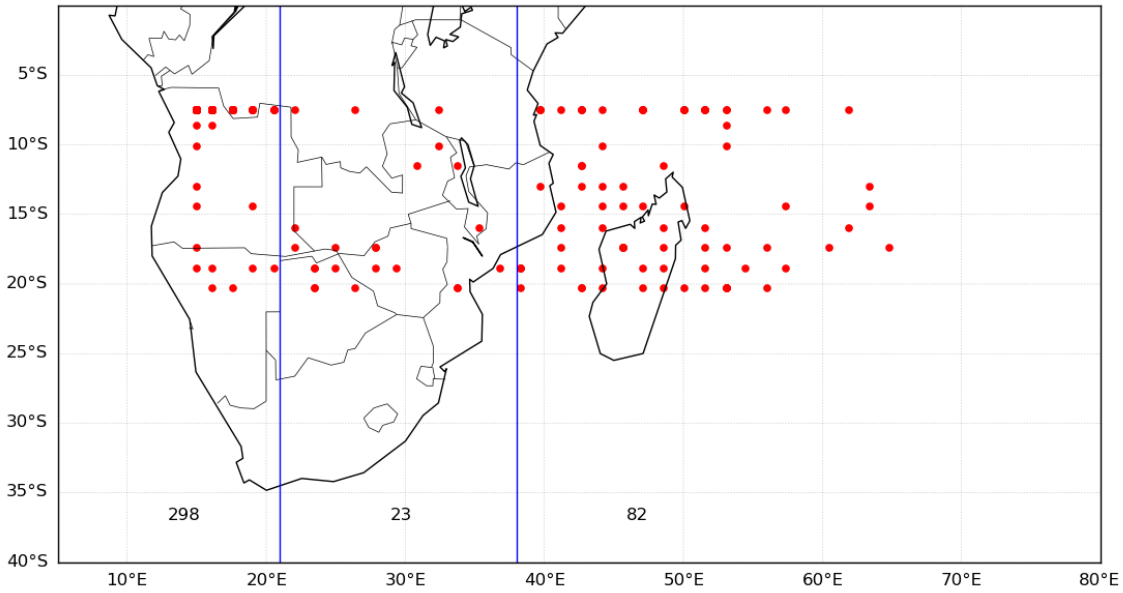

Figure 6.1.5: The anchor points (red dots) of the cloud bands modelled by ensemble member 1S1 during the study period. Each red dot can represent more than one anchor point. The blue lines divide the geographical domain in the three preferred regions where TTTs tend to develop. At the bottom of each region (columns), the number of cloud bands modelled within that region is displayed (around 35˚S).

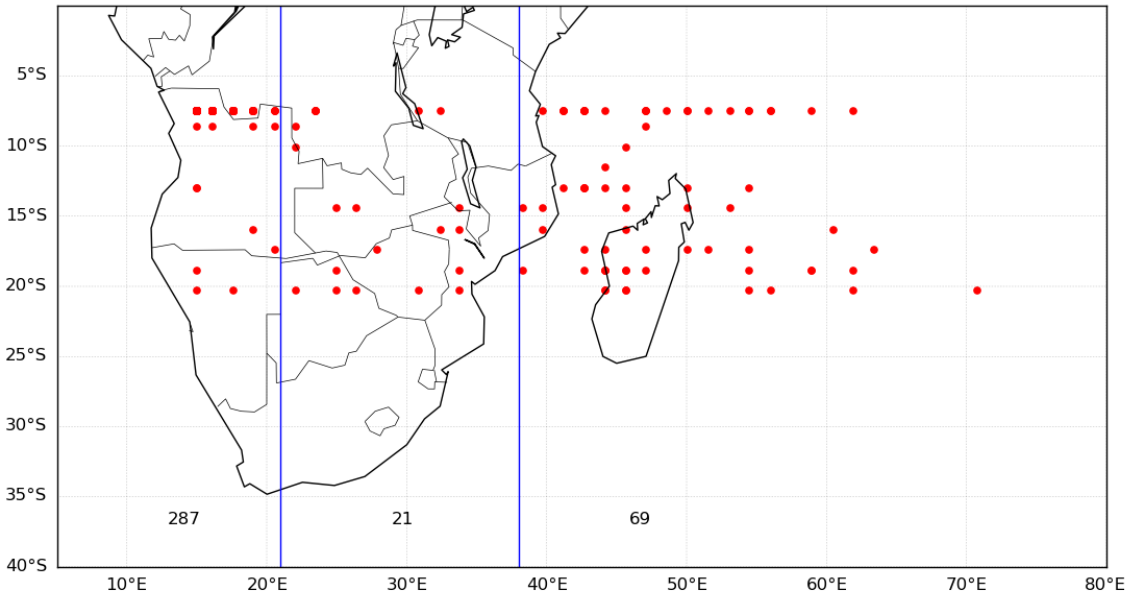

Figure 6.1.6: The anchor points (red dots) of the cloud bands modelled by ensemble member 1O1 during the study period. Each red dot can represent more than one anchor point. The blue lines divide the geographical domain in the three preferred regions where TTTs tend to develop. At the bottom of each region (columns), the number of cloud bands modelled within that region is displayed (around 35˚S).

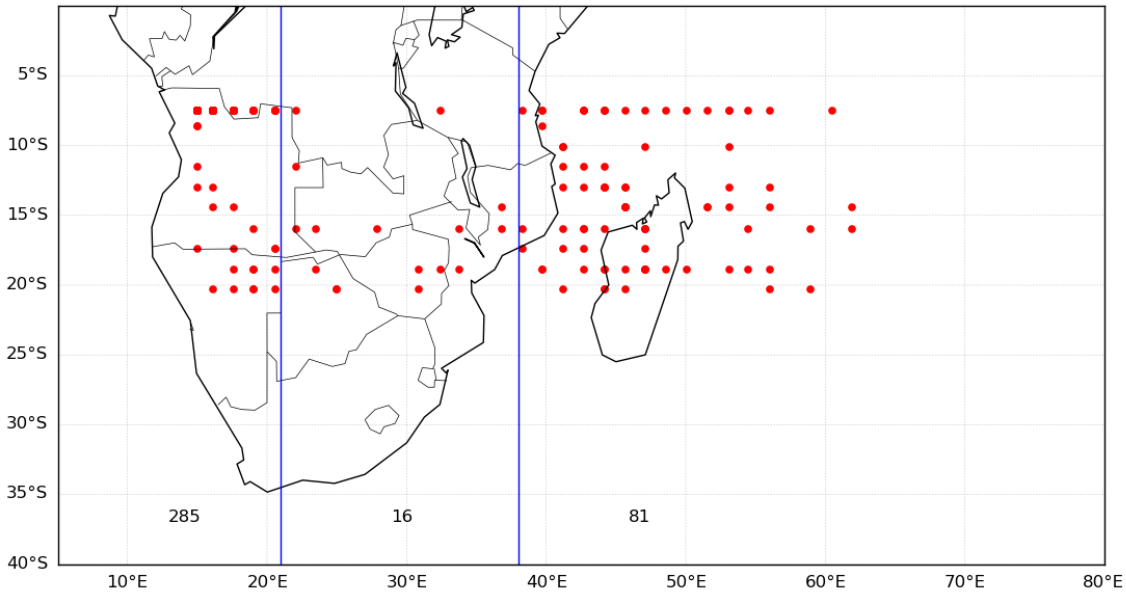

Figure 6.1.7: The anchor points (red dots) of the cloud bands modelled by ensemble member 1N1 during the study period. Each red dot can represent more than one anchor point. The blue lines divide the geographical domain in the three preferred regions where TTTs tend to develop. At the bottom of each region (columns), the number of cloud bands modelled within that region is displayed (around 35˚S).

According to the observed dataset (figure 6.1.1) the cloud bands have their anchor points between 5˚S and 20˚S. The ensemble members correctly modelled the latitude of the cloud bands, which could perhaps be part of the criteria of the MetBot to identify cloud bands. Regarding the longitude, the anchor points of the observed cloud bands can be found between 15˚E and 68˚E. Twelve ensemble members, i.e. 44% of the 27 ensemble members, modelled the cloud bands farther east than 68˚E, of which ensemble member 1O1 (fig. 6.1.6) is one of these.

6.2 Position of the centroid

The centroid, also called the geographical centre or the centre of mass, of the cloud bands is the arithmetic mean position of all the points in the shape, i.e. the centre of all the points in every coordinate direction. The centroid has therefore longitude and latitude and can be used to compare the average centre of the mass of the modelled cloud bands to that of the observed cloud bands. The position of the centroid contributes to two of the objectives of this study, namely the location of the cloud bands and the intensity of the cloud bands. By intensity is

meant the impact the cloud band and the resulting rain has on nature and humanity. The position of the centroid can also be an indication of whether the ensemble members have a bias towards a specific region and if the observed cloud bands tend to develop more in one location than another.

The same dilemma is faced in analysing the position of the centroid as with the anchor point of the cloud bands in Section 6.1. Therefore, a graphical display of the centroid's position will also be used in this section, instead of calculating the average position, the RMSE and the percentage deviation.

The position of the centroids of the observed cloud bands are displayed in figure 6.2.1 (the green dots in the figure). Interesting to note in the figure is that most of the centroids are situated above and around the summer rainfall region of South Africa (northern parts of South Africa), as well as Zimbabwe and the southern half of Mozambique. This "cluster" of centroids stretches across the Mozambique Channel towards the southern and central parts of Madagascar. A second smaller cluster can be found across the southern Indian Ocean (southeast of Madagascar). The centroid is calculated using the MetBot and therefore does not illustrate the gridded nature of data as can be seen in the results of the anchor points.

Figures 6.2.2, 6.2.3 and 6.2.4 indicate the positions of the centroids (the greed dots) of the cloud bands modelled by ensemble members 1S1, 1O1 and 1N1 respectively. These ensemble members are chosen randomly to illustrate the visual display of the centroids of the modelled cloud bands. For the rest of the ensemble members, please refer to Appendix B. The green dots indicate the positions of the centroids as modelled by the ensemble members. Also, in these figures are the positions of the anchor points of the cloud bands (the red dots). The anchor points are displayed in order to put the centroid positions in perspective. Keep in mind that one red dot can represent more than one cloud band. The blue lines divide the study domain in the three regions where TTTs tend to develop (have their anchor points). The number at the bottom of these regions is the number of cloud bands with anchor points in that particular region.

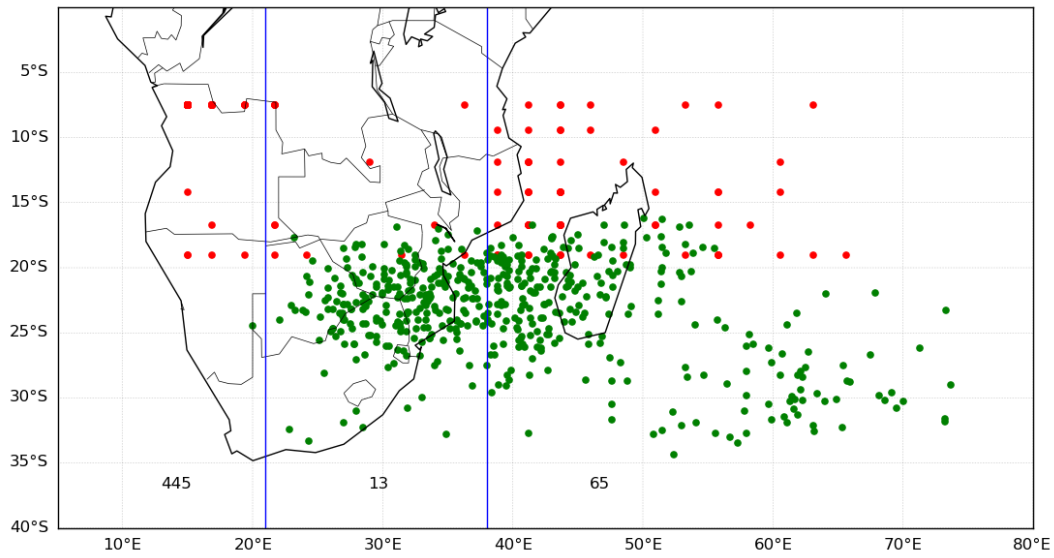

Figure 6.2.1: The anchor points (red dots) and the position of the centroids (green dots) of the observed cloud bands as flagged by the MetBot for the study period 1996/1997 to 2009/2010. Each red dot can represent more than one anchor point. The blue lines divide the geographical domain in the three preferred regions where TTTs tend to develop (have their anchor points). At the bottom of these three regions (columns), the number of cloud bands which developed within that region is displayed (around 37˚S).

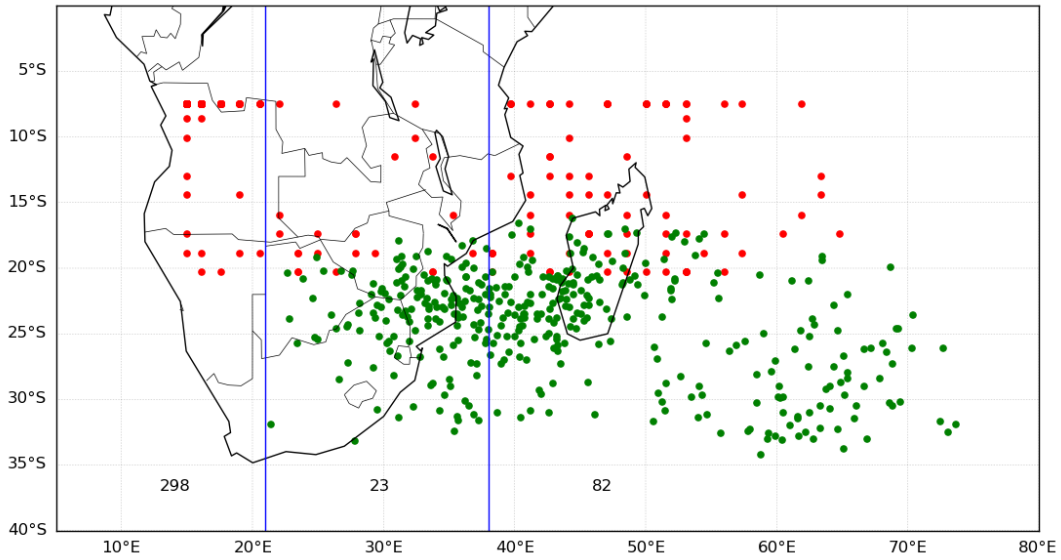

Figure 6.2.2: The anchor points (red dots) and the centroids (green dots) of the cloud bands modelled by ensemble member 1S1 for the NDJF seasons of 1996/1997 to 2009/2010. Each red dot can represent more than one anchor point. The blue lines divide the geographical domain in the three preferred regions where TTTs tend to develop. At the bottom of these three regions (columns), the number of cloud bands within that region is displayed (around 37˚S).

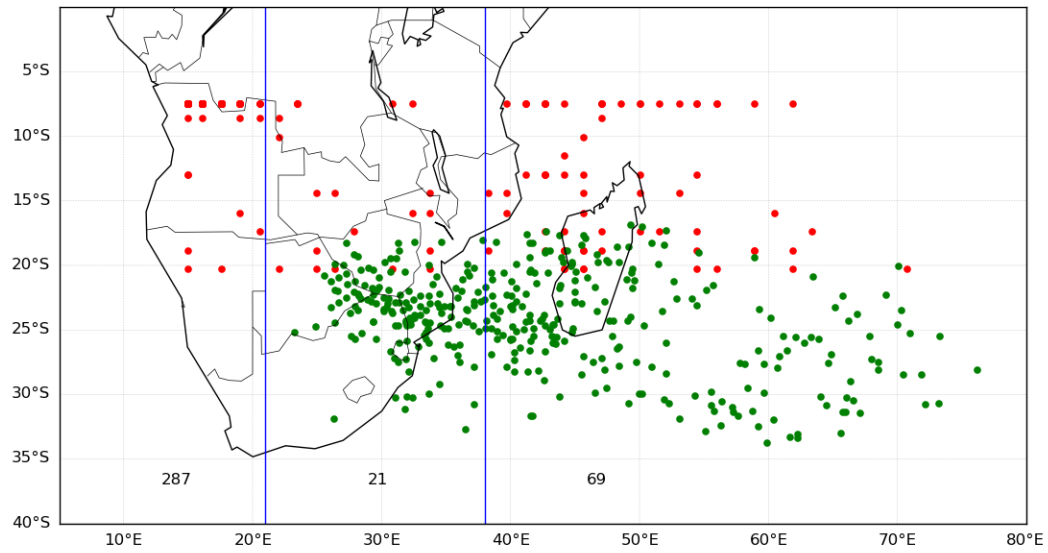

Figure 6.2.3: The anchor points (red dots) and the centroids (green dots) of the cloud bands modelled by ensemble member 1O1 for the NDJF seasons of 1996/1997 to 2009/2010. Each red dot can represent more than one anchor point. The blue lines divide the geographical domain in the three preferred regions where TTTs tend to develop. At the bottom of these three regions (columns), the number of cloud bands within that region is displayed (around 37˚S).

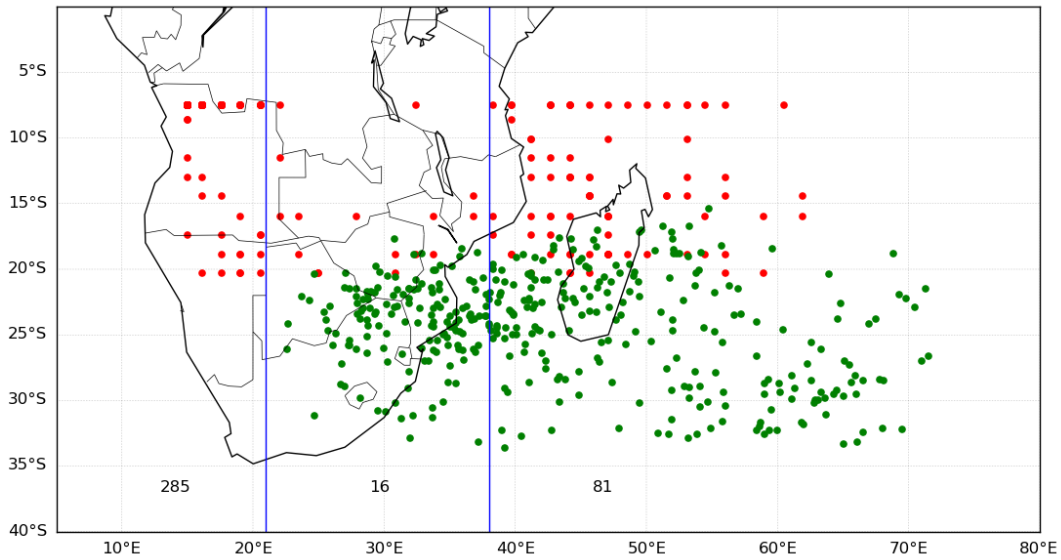

Figure 6.2.4: The anchor points (red dots) and the centroids (green dots) of the cloud bands modelled by ensemble member 1N1 for the NDJF seasons of 1996/1997 to 2009/2010. Each red dot can represent more than one anchor point. The blue lines divide the geographical domain in the three preferred regions where TTTs tend to develop. At the bottom of these three regions (columns), the number of cloud bands within that region is displayed (around 37˚S).

Most of the modelled cloud bands have their centroids in a similar region as that of the observed (fig. 6.2.1), i.e. most of the centroids of the modelled cloud bands are found around the northern parts of South Africa, across Zimbabwe and Mozambique, as well as the southern and central parts of Madagascar. No centroids (observed and modelled) are found north of 15˚S. Very few modelled centroids are positioned south of 30˚S. This is also the case with the observed centroids.

In the observed dataset, there is only one cloud band with its centroid positioned west of 21˚E, i.e. within region 1. The ensemble members modelled very few cloud bands with their centroids positioned in region 1. Most ensemble members do not have any cloud bands with their centroids positioned in this region. In fact, only four ensemble members (14.81% of the 27 ensemble members) modelled cloud bands with the position of the centroid in region 1.

Interesting to note is that a considerable number of centroids are positioned east of Madagascar in both the observed dataset and the modelled dataset. These cloud bands will inevitably have no or very little impact regarding rainfall over a landmass.

6.3 Tilt

The northwest-southeast (NW-SE) tilt of a cloud band contributes to the location of a cloud band, which is one of the sub-objectives of this study. It is calculated using the north-western most point (the anchor point) and the south-eastern most point. If the cloud band has more of a north-south tilt, it will for example be more confined to the west and the central parts of South Africa, if it has its roots in Namibia. A cloud band with a flatter tilt (more west-northwest to east-southeast) and with its roots in region 1, will stretch to the eastern parts of South Africa and even perhaps over the southwestern Indian Ocean. In the latter case, a cloud band will potentially affect more people due to the high population density in the eastern half of South Africa, compared to that of the western half.

The tilt of the cloud bands is part of the output of the MetBot. The tilt has a negative orientation and is usually between 0˚ and -90˚. In some cases, the MetBot picked up on a positive tilt for the cloud bands, which are nonetheless flagged and considered as cloud bands. There are two calculations for the tilt within the MetBot: a small section with the lowest OLR values and the

larger area, which consists of the entire cloud band. If the smaller section is within the criteria the MetBot uses, then it will be flagged as a cloud band. The tilt of the entire cloud band (the larger area) is then calculated and saved in the output file. It is therefore possible that cloud bands can have a positive tilt.

When calculating the average of the combined positive and negative tilts, the positive tilts will lead to a lower average tilt than when only the negative tilts are considered. Figure 6.3.1 illustrates the difference between the average of the combined negative and positive tilts (blue line) and the average of the negative tilts only (red line) of the observed cloud bands for the considered study period. The averages of the two series coincide for a few seasons, which means that for that specific season there are no observed cloud bands with a positive tilt, for example the seasons of 1998/1999 and 2002/2003. The greatest impact that the cloud bands with a positive tilt has, is on the average tilt of the NDJF season of 2009/2010. During this season, there are only three observed cloud bands with positive tilts. These three positive tilts have such a huge impact on the average due to the fact that the angle of two of them is greater than +80˚. Usually the positive angles are closer to 0˚.

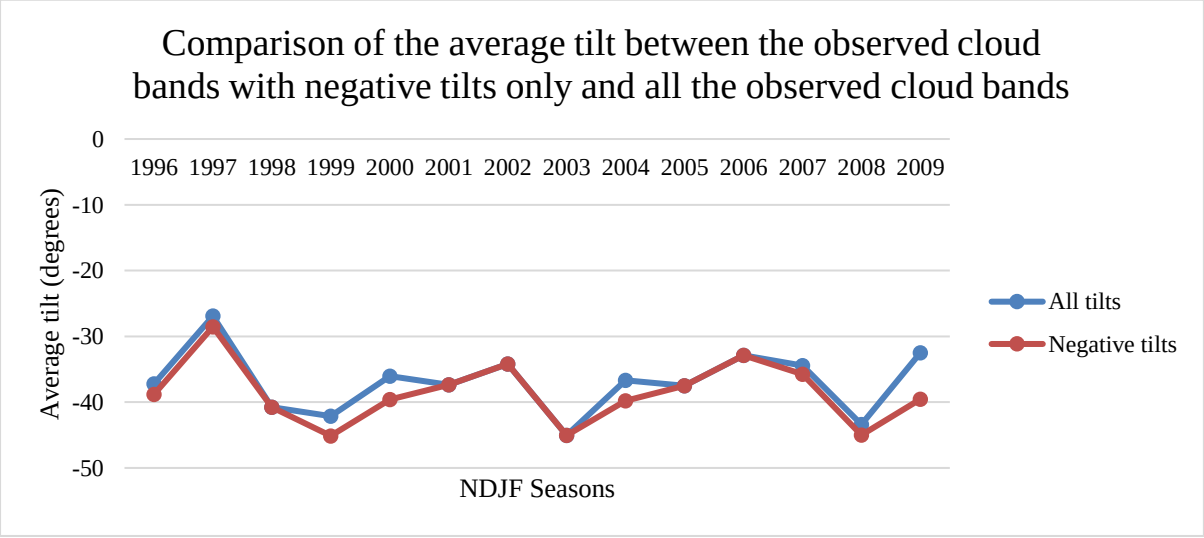

Figure 6.3.1: A comparison between the average of the positive and negative tilts (blue line) and the average of the negative tilts only (orange line) of the observed cloud bands per season for the NDJF seasons of 1996/1997 to 2009/2010.

It has been decided to include the cloud bands with a positive tilt for the characteristics of TTTs (except the tilt) discussed earlier in this study, because these cloud bands passed the criteria. Keep also in mind that both the observed and the modelled datasets run through the same

criteria and algorithm to establish possible TTT events and in both datasets, there are TTT events with positive tilts. This is perhaps an example that the model faired well, because it also simulated cloud bands with positive tilts, as are present in the observed dataset.

To illustrate the impact the positive tilts has on the results, both sets (the negative tilts only and the positive and negative tilts combined) are considered and represented in this section, with the subsection on positive tilts in somewhat lesser detail. In the subsections to follow, results will be shown for the averages, the RMSE values and the percentage errors of the negative tilted cloud bands, as well as for the positive and negative tilted cloud bands combined. To consider the positive tilts separately is not viable, because there are not that many of them and there are a few seasons with no positively tilted cloud bands.

6.3.1 Negative tilts only

To establish the effect the positive tilts have on the averages (and to investigate the performance of the model on this characteristic of TTTs properly), the negative tilts are considered separately. Figure 6.3.2 displays the average tilts of the observed cloud bands for every NDJF season of 1996/1997 to 2009/2010. The average of the negative tilts per season is between -27˚ and -47˚. Over the entire study period it averages to -38.57˚, which is 1.64˚ more negative than the average for the combined positive and negative tilts.

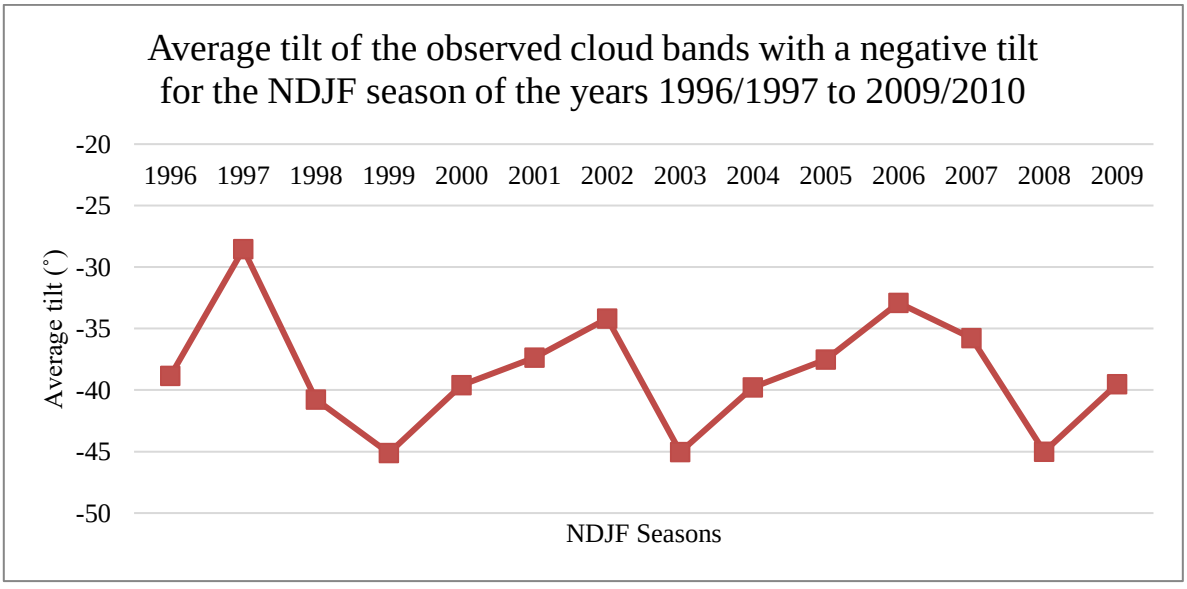

Figure 6.3.2: The average of the negative tilts of the observed cloud bands per season for the NDJF seasons of 1996/1997 to 2009/2010.

The averages of the negative tilts of the cloud bands represented by the 27 ensemble members for the entire study period are displayed in figure 6.3.3. The average tilt of the cloud bands modelled by the ensemble members calculates to -39.33˚ and corresponds to an observed average tilt of -38.55˚. As discussed before, the average value mentioned here differs from the one mentioned in the previous paragraph, because some of the ensemble members do not have a complete dataset for the entire study period. Therefore, the corresponding observed data for the missing periods of data of these ensemble members is omitted. The difference between the average modelled and the average observed tilts is 0.78˚.

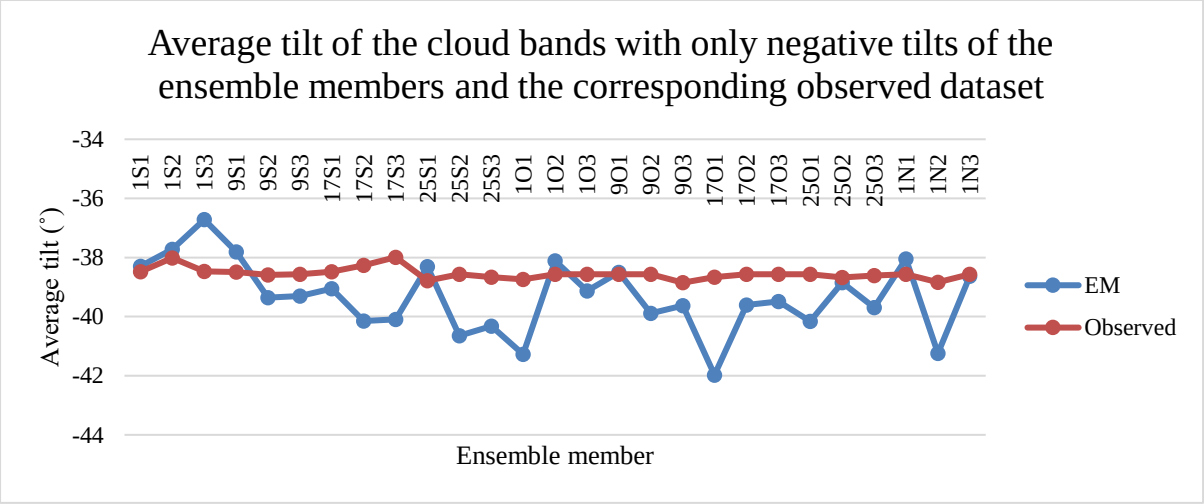

Figure 6.3.3: The average of the negative tilts of modelled cloud bands of all 27 ensemble members (blue line) compared to that of the corresponding observed cloud bands (red line) for the study period. EM stands for ensemble member. For the abbreviations of the ensemble members, please refer to table 3.1.

The RMSE values and the corresponding percentage errors for the average tilt of the cloud bands modelled by all ensemble members are given in table 6.3.1 below. The average RMSE and the percentage error of all the ensemble members calculate to 6.14˚ and 15.92% respectively. Regarding the average tilt of the cloud bands, ensemble member 1N3 fared the best. It has an RMSE value of 4.18˚ and a percentage error of 10.85%. Ensemble member 1O1 had the highest RMSE value (8.93˚) with the corresponding percentage error as 23.04%.

Table 6.3.1: The RMSE values in degrees (˚) and the percentage error of the average of negative tilts of the cloud bands for the 27 different ensemble members. EM stands for ensemble member and the abbreviations of the ensemble members can be found in table 3.1. The RMSE and the percentage error averages in the last row of the last two columns are the averages for all 27 ensemble members.

EM	**RMSE (˚)**	**Error (%)**		**EM**	**RMSE (˚)**	**Error (%)**
1S1	6.80	17.67		1O3	6.23	16.16
1S2	7.24	19.05		9O1	5.69	14.77
1S3	5.87	15.25		9O2	5.75	14.92
9S1	5.27	13.69		9O3	6.58	16.94
9S2	5.92	15.34		17O1	6.37	16.47
9S3	5.06	13.12		17O2	6.15	15.96
17S1	7.24	18.81		17O3	7.28	18.87
17S2	5.76	15.04		25O1	6.06	15.71
17S3	6.89	18.13		25O2	5.77	14.92
25S1	5.06	13.04		25O3	5.04	13.07
25S2	6.14	15.91		1N1	6.28	16.28
25S3	5.94	15.35		1N2	7.35	18.93
1O1	8.93	23.04		1N3	4.18	10.85
1O2	4.87	12.63		**Average**	6.14	15.92

The best and worst performing ensemble members regarding the average (negative) tilt of the modelled cloud bands are displayed in figures 6.3.4 and 6.3.5. The blue line indicates the average of the ensemble member and the orange line that of the observed cloud bands. In figure 6.3.4 it is apparent why the RMSE value of ensemble member 1N3 is the lowest: the year-to-year variation of the modelled average tilt is very close to that of the observed. The greatest difference between the modelled and the observed average tilt is for the seasons 1997/1998 and 2002/2003, as well as from 2006/2007 to 2009/2010. For the remaining seasons the difference is small. The worst performer (ensemble member 1O1) on the other hand, has a number of seasons where the difference is quite large, namely 1997/1998, 2003/2004, 2006/2007 and 2007/2008. These outliers inevitably affect the average tilt and therefore also the RMSE values significantly.

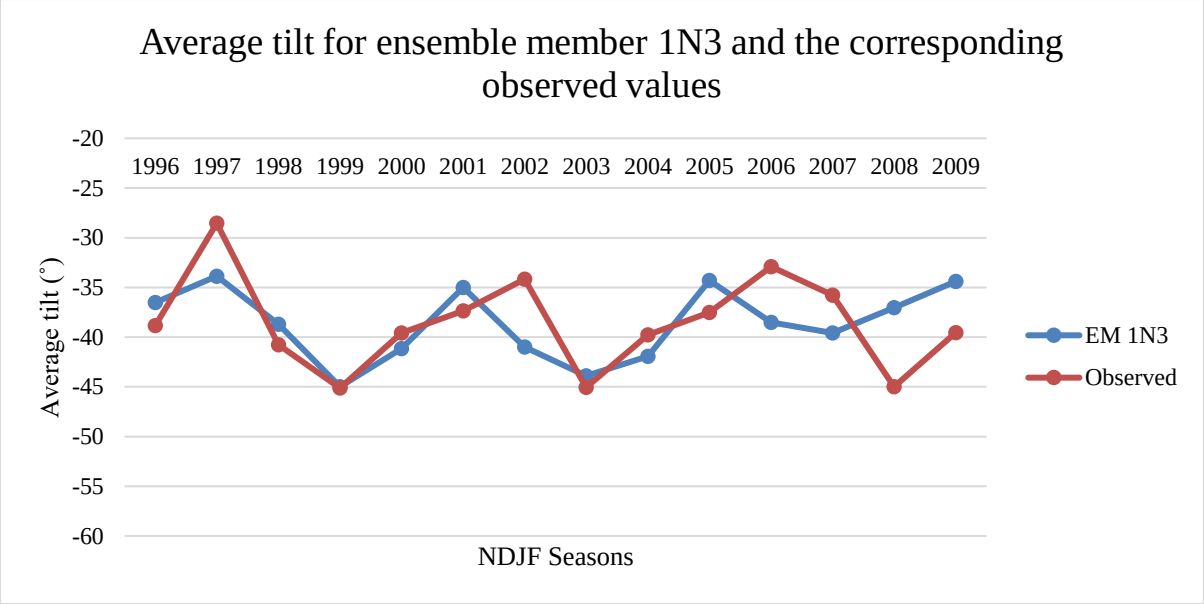

Figure 6.3.4: The average of the negative tilts of the cloud bands modelled by ensemble member 1N3 (blue line) and the corresponding observed values (orange line) for the study period 1996/1997 to 2009/2010.

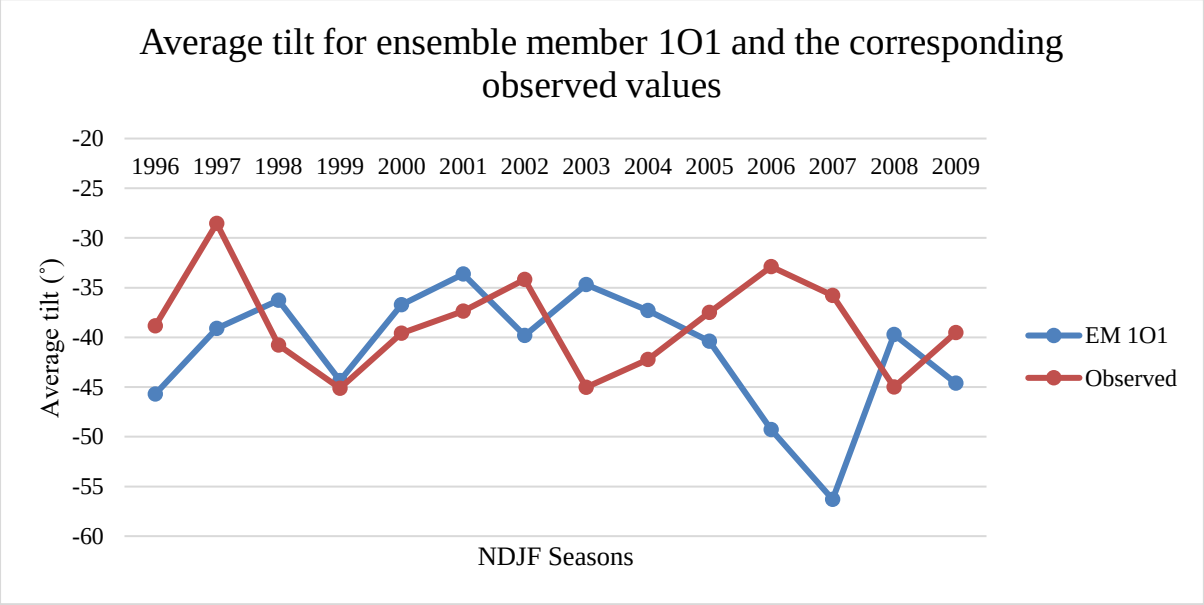

Figure 6.3.5: The average of the negative tilts of the cloud bands modelled by ensemble member 1O1 (blue line) and the corresponding observed values (orange line) for the study period.

There is no clear bias in the modelled average tilts of the ensemble members. Therefore, no bias-adjustment is necessary.

6.3.2 Positive and negative tilts combined

The average combined positive and negative tilts of the observed cloud bands for every season from 1996/1997 to 2009/2010 are displayed in figure 6.3.6. As can be seen in this figure, the seasonal average tilts are between -26˚ and -46˚. The average tilt for the entire study period (NDJF seasons of 1996/1997 to 2009/2010) calculates to -36.93˚.

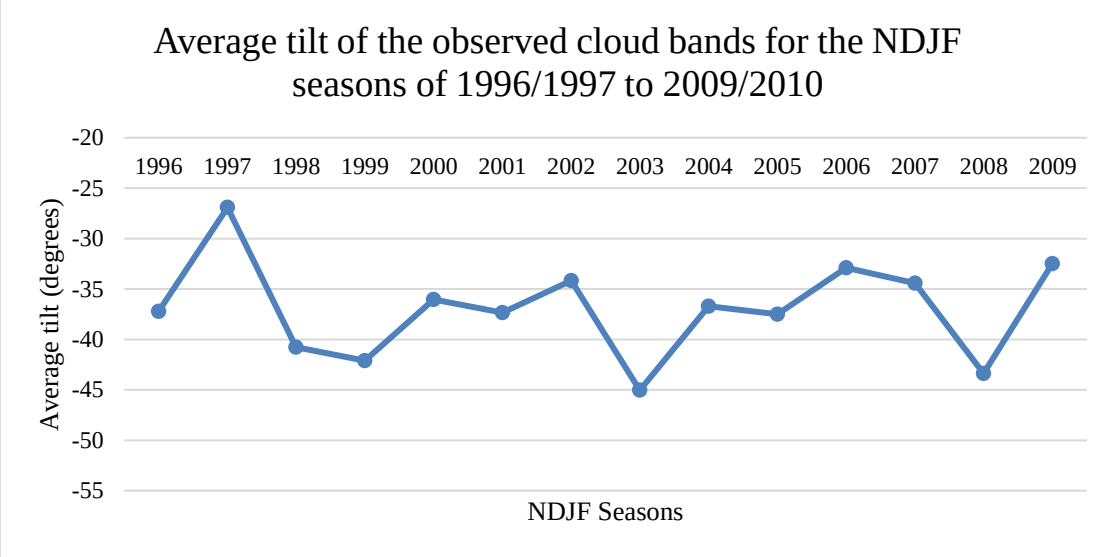

Figure 6.3.6: The average of the positive and the negative tilts combined of the observed cloud bands per season for the NDJF seasons of 1996/1997 to 2009/2010.

In figure 6.3.7 the combined positive and negative tilts of the cloud bands modelled by all the ensemble members can be found. These tilts are the average values of all the seasons within the study period. The average tilt of the ensemble members calculates to -37.19˚ and the average of the corresponding observed tilts comes to -36.94˚. The average value here differs from the one mentioned earlier, because (as discussed previously) the data of some of the ensemble members is not complete for the entire study period. Therefore, for these ensemble members the corresponding observed data has to be omitted (as discussed earlier in this study). The difference between the average modelled and the average observed tilts is 0.25˚. This results in a 0.68% error. The difference between the average modelled tilts and the average observed tilts is less than the difference in these variables when considering only the negative tilted cloud bands.

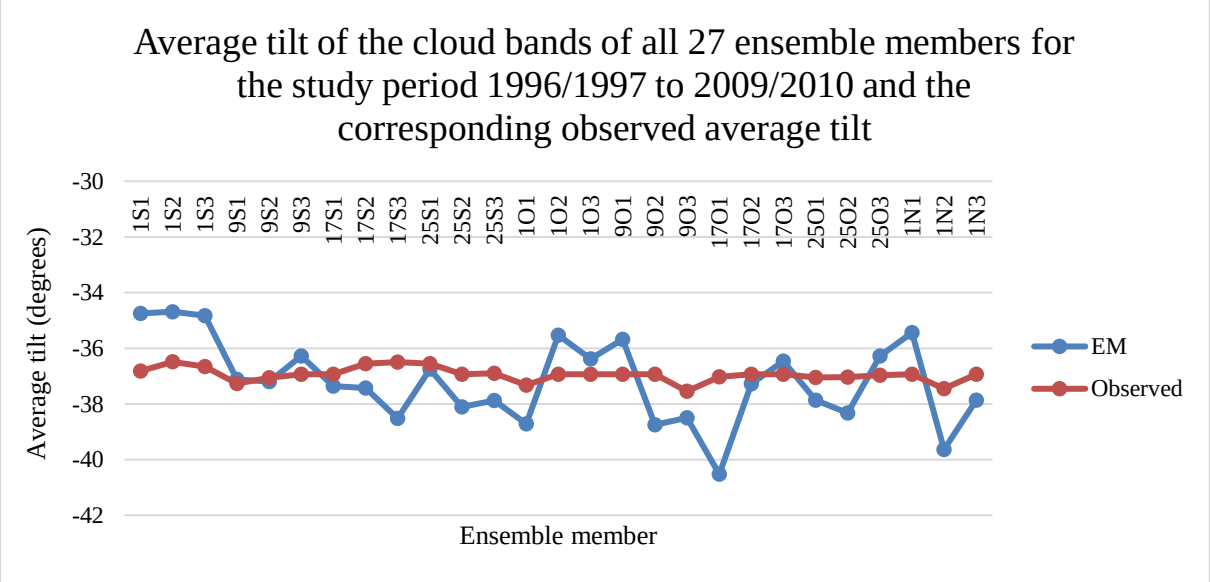

Figure 6.3.7: The average of the positive and the negative tilts combined of modelled cloud bands of all 27 ensemble members (blue line) compared to that of the corresponding observed cloud bands (orange line) for the study period. EM stands for ensemble member. For the abbreviations of the ensemble members, please refer to table 3.1.

In table 6.3.2 the RMSE values and the percentage errors for the average tilt of all the ensemble members are displayed. When perusing the RMSE's and the accompanying percentage errors of the tilts, the ensemble members do not fare as well as when comparing the average tilts directly. The average RMSE value and the accompanying average percentage error of all the ensemble members are 6.61˚ and 17.91% respectively. Ensemble member 1N3 has the lowest RMSE value (4.65˚) with a percentage error of 12.6%. This ensemble member has no missing data for the entire study period. Both these values are higher than that of the negative tilts only (6.4˚ and 15.92%). Whether the cloud band has a positive or a negative tilt does not have an effect on the RMSE value. It can therefore be concluded that the ensemble members fare better when only the cloud bands with negative tilts are considered.

From the table it seems like both ensemble members 17S3 and 1O1 are the worst performers with an RMSE of 8.27˚, while the percentage errors differ (22.65% compared to 22.16%). This is due to the difference in the average observed tilt for each of these ensemble members (due to the lack of data for some part of the study period). Ensemble member 17S3 misses data for the three seasons of 1999/2000, 2000/2001 and 2001/2002. Ensemble member 1O1 only misses data for the period December 2004 to February 2005. The RMSE value (to 4 decimals) of ensemble member 17S3 is 8.2692˚ and that of ensemble member 1O1 is 8.2723˚.

Table 6.3.2: The RMSE values in degrees (˚) and the percentage error of the average of the positive and negative tilts of the cloud bands for the 27 different ensemble members. EM stands for ensemble member and the abbreviations of the ensemble members can be found in table 3.1. The RMSE and the percentage error averages in the last row of the last two columns are the averages for all 27 ensemble members.

EM	**RMSE (˚)**	**Error (%)**		**EM**	**RMSE (˚)**	**Error (%)**
1S1	7.49	20.33		1O3	6.95	18.81
1S2	8.22	22.53		9O1	6.67	18.05
1S3	6.91	18.85		9O2	5.05	13.69
9S1	5.34	14.32		9O3	6.97	18.56
9S2	6.67	18.00		17O1	7.16	19.35
9S3	5.93	16.06		17O2	7.15	19.36
17S1	7.11	19.26		17O3	6.48	17.55
17S2	6.34	17.34		25O1	7.90	21.33
17S3	8.27	22.65		25O2	5.78	15.61
25S1	5.87	16.07		25O3	6.53	17.66
25S2	6.22	16.84		1N1	7.78	21.06
25S3	5.48	14.85		1N2	5.81	15.52
1O1	8.27	22.16		1N3	4.65	12.60
1O2	5.58	15.11		**Average**	6.61	17.91

6.4 Synopsis

In this chapter the results regarding the location of the cloud bands associated with TTT events are displayed. These results include the anchor points, the position of the centroid and the tilt of the cloud bands. Modelled data is compared to observed data. The geographical domain of this study is divided into the three regions where TTTs tend to develop. To evaluate the performance of the ensemble members regarding the anchor points and the position of the centroids, a visual display is used. To investigate the tilt of the modelled cloud bands and how it compares to the observed cloud bands, the average tilt, the RMSE and the percentage error are calculated. Thereafter, the results (maps and graphs) of the best and worst performing ensemble members are presented. Some of the flagged cloud bands in both the observed and the modelled datasets have a positive tilt. These positive tilts have an impact on the average tilt. Therefore, the results for the cloud bands with negative tilts are presented separately, in order to establish the true performance of the model regarding the tilt of the cloud bands.

This chapter concludes the results of this study. In the next chapter the results will be discussed in depth to finally draw a conclusion on the performance of the GloSea5 model (the ensemble average considering all the characteristics of TTT events) in the chapter thereafter.

CHAPTER 7: Discussion

This project investigates the ability of a state-of-the-art seasonal forecast model, the GloSea5 of the UK Met Office, to predict TTT events for the summer rainfall season of southern Africa. Daily outgoing longwave radiation (OLR) is used as input for the MetBot (as discussed in chapter 2) to flag TTT events in the observed and the modelled dataset. Using the output of the MetBot the different objectives and subobjectives of the project are addressed. These objectives are to identify cloud bands associated with TTT events in both the observed and the modelled data and to investigate the characteristics of these weather phenomena by looking at the frequency, location and intensity thereof.

For this study, 27 ensemble members of the GloSea5 are used. These members were initiated on the 1st, 9th, 17th and 25th of September and October, as well as the 1st of November for the years 1996 to 2009. The summer rainfall season of southern Africa is considered as the months November, December, January and February (NDJF) (e.g. Pohl et al, 2018). The meteorological summer usually lasts from 1 December until 28 (or 29) February in the southern hemisphere. However, due to the number of heavy rainfall events, such as TTT events, that occur in November (e.g. Hart et al, 2013), it is decided to include November as part of the summer rainfall season.

Both the modelled and the observed datasets consist of gridded data for the geographical domain of this project. More on this and the resolution of the datasets can be found in chapter 2 (Methodology).

In the previous four chapters (chapters 3 to 6) the results of this study are presented. This chapter consists of a detailed discussion on the results. First the results of each objective and subobjective will be discussed. Then a discussion will follow in how the forecast model fared as an ensemble average and to what length the research question is addressed.

7.1 Identifying modelled cloud bands

The MetBot is used to identify cloud bands in the modelled and the observed datasets. As part of the output, two figures are presented for each flagged cloud band (figure 3.1). These figures in itself are a confirmation that the MetBot can identify cloud bands which are associated with TTT events. Therefore, the first objective of this project is achieved, namely for the model to be able to identify modelled cloud bands associated with TTT events by using gridded data.

The details of the cloud bands identified by the MetBot are used to reach the next objective, which is to investigate the characteristics of the modelled cloud bands, namely the frequency, the location and the intensity.

7.2 Frequency of the modelled cloud bands

One of the characteristics of TTT events investigated in this project is the frequency thereof across southern Africa, i.e. how often do TTTs occur. For this sub-objective, the number of cloud bands are used. On average there are 37.36 cloud bands observed per NDJF season for the study period 1996/1997 to 2009/2010. The observed number of cloud bands may seem quite high, but keep in mind that these are only the cloud bands associated with TTT events and not particularly a fully developed TTT that lasts three to five days. The ensemble members predicted on average about 27 cloud bands per season. The average predicted number of cloud bands may be less than the observed number of cloud bands, but the model still fared well in predicting these systems more than 70% of the time.

When considering the ensemble members separately, it is found that there are some of the summer rainfall seasons in the study period for which certain ensemble members over-predicted the number of cloud bands. A surprising result is that 81.5% of the ensemble members (22 of the 27 members) over-predict the number of cloud bands for the season 1996/1997 and almost half of the ensemble members (48.1%) over-predict the number of cloud bands for the 2006/2007 season. This result could be related to the El Niño Southern Oscillation (ENSO), which will be discussed later in this chapter (section 7.7).

Another measure is used to compare the number of cloud bands of the observed and the modelled datasets, namely the percentage deviation. The average percentage deviation is calculated as -28.29%. It appears that the average percentage deviation converges to approximately -27% with a shorter lead-time. More specifically for the ensemble members initiated on 17 October, 25 October and 1 November, but especially for the last two initiation dates. This result is not unexpected, as most models perform better with a shorter lead-time. The question is whether this is the case with all the different output data – a question that will be addressed in the sections to follow.

The last calculations performed for the section on the number of cloud bands are to calculate the RMSE and the associated percentage error. By calculating the percentage error, the RMSE is put into perspective.

The RMSE and the percentage error calculated to 14.44 cloud bands and 38.8% respectively. This result indicates that the ensemble members under-predict the number of cloud bands, which already reflected in the previous results. This result can be improved by adjusting the bias. After the bias is adjusted, the RMSE and the percentage error came down to 9.61 cloud bands and 26.23% respectively. These values are significantly lower than the values calculated before the bias-adjustment is applied.

The ensemble members (and therefore the GloSea5 model as a whole) can identify cloud bands and inevitably TTT events during a season, but the number of cloud bands are somewhat underpredicted. It is possible that the GloSea5 models the correct number of cloud bands, but perhaps these are located farther west or farther east. To investigate this possibility, it will be necessary to enlarge the geographical domain. This change in the configuration can perhaps be considered in a future study. Therefore, when using this particular seasonal forecast model to predict whether above normal rainfall in one season will be caused by a few large heavy rainfall events such as TTTs, it will have to be kept in mind that the model under-predicts the number of these type of weather phenomena.

7.3 Intensity of the modelled cloud bands

The best way to study the intensity of the cloud bands is to compare the average area, as well as the minimum and maximum OLR values of the modelled cloud bands to that of the observed cloud bands. The area was chosen as it relates directly to the size of the cloud band and therefore the geographical area that is impacted by a TTT event. The larger the TTT on a horizontal scale, the greater the area affected. OLR was chosen due to its relation to the amount of rainfall. The lower the OLR values, the more radiation is trapped by the cloud band, therefore the thicker the cloud band. A thicker cloud band indicates more precipitable water within the clouds, which can lead to heavier rainfall. Therefore, the OLR is a measure of the intensity of the cloud band and TTT event.

7.3.1 Area

For the observed cloud bands, the average area of a cloud band (for the entire study period) calculates to 35841.33km^2. The season with cloud bands of the smallest spatial extent is 2003/2004 with an average area of 31785km^2 and the season with the largest average area is 1997/1998 (46749km^2). What could be of interest about this result is that the season of 1997/1998 is one of the strongest El Niño events during which South Africa unexpectedly received more rainfall than usually associated with an El Niño event. Usually the summer rainfall region of South Africa receives below-normal rainfall during an El Niño year. The higher-than-expected rainfall could be due to the fact that the TTT events of that particular season is on average larger than other seasons. If the two extreme seasons (largest and smallest average areas) are omitted, then the average area of the observed cloud bands calculates to 35270.38km^2, which is only slightly lower than the average of all 14 seasons. It can therefore be concluded that these two outlying seasons did not have such a great effect on the average area of the TTT events. From figure 5.1.1 it can be seen that the average area of the cloud bands for most of the seasons oscillates around 35000km^2.

When calculating the average observed area of the cloud bands per ensemble member and omitting the missing model data periods, an average of 35795 km^2 is obtained, which is slightly lower than the actual observed average area per cloud band.

Similar to the number of cloud bands, the different ensemble members under-predict the area of the cloud bands on average by 5902km^2. The ensemble members do not under-predict the

average area of the cloud bands for every season: there are seasons for which some ensemble members over-predict the average area. The season for which the most ensemble members over-predict the average area is the 2003/2004 season, in this case for 9 of the 27 ensemble members. The season for which the ensemble members over-predict the average area the second most is 2004/2005 (4 of the 27 ensemble members). The 2003/2004 season coincides with a neutral year, while the 2004/2005 season corresponds to a weak El Niño year. During La Niña years, South Africa tends to receive above average rainfall in the summer rainfall region (mainly the north-eastern part of the country), and during El Niño years below normal rainfall (as mentioned earlier in this chapter).

The RMSE value for the average area of the modelled cloud bands calculates to 7268.43km^2, which yields a percentage error of 20.31%. In combination with the previous results on the average area of the modelled cloud bands, it can be concluded that the ensemble members on average under-predict this particular TTT characteristic by 20.31%. The bias of the model can therefore be adjusted by taking this error into consideration. A bias-adjustment is subsequently applied and the resulting change in the performance of the model is significant. With the bias-adjustment, the average RMSE value reduces to 4359.2km^2 and the corresponding percentage error to 12.18%. While the error is still above 10%, it is quite an improvement from 20.31%. There are a few individual ensemble members with a bias-adjusted percentage error of less than 10%. These ensemble members do not necessarily have a short lead-time. The individual ensemble members will be discussed later in this chapter.

When regarding the general performance of the different ensemble members and that of the model as a whole, it may seem that the model did not fare that well. However, when considering the size of the cloud bands and the area that TTT events usually affect, the model fare well, and with a bias-adjustment applied, the model can be used to forecast the average area of TTT events on a seasonal scale, provided that a small margin of error is taken into consideration.

7.3.2 Outgoing Longwave Radiation

Outgoing Longwave Radiation (OLR) is used to determine the intensity of the cloud bands. Within a cloud band there is an area with the lowest OLR value, hereafter referred to as the minimum OLR, and an area with the highest OLR value, hereafter referred to as the maximum OLR. Both these values form part of the output file for every cloud band that is flagged by the MetBot.

7.3.2.1 Minimum OLR

The minimum OLR value indicates the section of the cloud band that emits the least amount of OLR. This value can be translated to the thickest part of the cloud as explained in chapter 5 section 5.2.1.

The average minimum OLR per season of the observed cloud bands for the considered study period range between 128 W/m^2 and 141 W/m^2. For the entire study period, the average minimum OLR calculates to 135.78 W/m^2. The seasons with the lowest average minimum OLR values are 1997/1998, 1999/2000, 2000/2001 and 2002/2003. The highest average minimum OLR values are obtained in the seasons 1996/1997, 2003/2004, 2008/2009 and 2009/2010. Of these seasons, 1997/1998, 2002/2003 and 2009/2010 are El Niño years, and 1999/2000 and 2000/2001 are La Niña years. The season 1997/1998 is considered one of the strongest El Niño events on record (e.g. L'Heureux et al, 2017). However, during this particular El Niño some parts of South Africa received above-normal rainfall (Lyon and Mason, 2007). Therefore, low average minimum OLR values do not necessarily coincide with ENSO, but they seem to indicate wetter than normal seasons. Of the four seasons with the highest average minimum OLR values, two are considered neutral ENSO years, one is a weak La Niña year and the last one is a strong El Niño year. It is possible that there might be a link between neutral ENSO years and seasons with TTT events with greater than average minimum OLR values. However, a more in-depth study is necessary with a longer study period to confirm or contradict this possible link between the average minimum OLR values of TTT events and ENSO.

Of all 27 ensemble members, only one (17O1) obtained an average minimum OLR value above that of the observed cloud bands. The rest of the ensemble members calculated lower average minimum OLR values than that of the observed dataset. Ensemble member 17O1 misses data for 3 months of the season 2001/2002, which could possibly have an effect on the average minimum OLR value being higher than the observed. However, the missing data sections are accounted for as described in various previous sections such as in chapter 2 (Methodology) section 2.4.3.

The fact that the average minimum OLR values of most ensemble members are lower than the values of the observed dataset, indicates that the model in general produces cloud bands that

are thicker than the observed. Thicker cloud bands in turn indicate TTT events with a higher intensity.

The average minimum OLR of the ensemble members varies between 4.75 W/m^2 and 10.76 W/m^2, thus it falls within a range of 6.01 W/m^2. The average RMSE for all 27 ensemble members of the average minimum OLR values calculates to 7.09 W/m^2, with a corresponding average percentage error of 5.2%. This is relatively low, especially compared to the RMSE and the percentage error of the other characteristics that are investigated. Due to the low average RMSE value, it is decided not to adjust the bias for the minimum OLR.

7.3.2.2 Maximum OLR

The maximum OLR value indicates the section of the cloud band that lets the most OLR pass through, i.e. the thinnest part of the cloud. On average the observed cloud bands have a maximum OLR of 237.9 W/m^2. The seasons with the highest average maximum OLR in the study period are 1997/1998 and 2007/2008. These two years are considerately higher than the rest (above 242 W/m^2). As mentioned earlier in this chapter, the season of 1997/1998 was one of the strongest El Niño events, which produced surprisingly high amounts of rainfall in South Africa, while 2007/2008 was a strong La Niña year. The season of 2006/2007 has the lowest average maximum OLR (less than 234 W/m^2) and is considered a weak El Niño. A possible connection between ENSO and TTT events will be discussed later in this chapter.

The average maximum OLR of all 27 ensemble members calculated to 235.26 W/m^2. As with the other parameters discussed, this value is lower than the observed average maximum OLR. The average RMSE and the percentage error of the maximum OLR of the ensemble members vary between 3.55 W/m^2 and 6.11 W/m^2, thus within a range of 2.56 W/m^2. The average RMSE value of the maximum OLR for the different ensemble members comes to 4.53 W/m^2 with a corresponding percentage error of 1.9%. These values are even lower than the average RMSE of the minimum OLR (7.09 W/m^2 and 5.2%). These lower values could be connected to the fact that there is a minimum threshold build into the criteria of the MetBot to flag cloud bands. However, seeing that some of the maximum OLR values of the observed cloud bands exceeded 240 W/m^2 (the minimum OLR criteria for a cloud band), it is more likely that the different ensemble members performed better regarding the maximum OLR per cloud band. Another indication that the ensemble members fare better regarding the maximum OLR values is that the difference between the lowest and the highest average maximum OLR compared to that of

the average minimum OLR of the different ensemble members is much smaller (2.56 W/m^2 compared to 6.01 W/m^2). Therefore, it can be said with some certainty that the model performed well regarding the maximum OLR of the cloud bands.

7.4 Location of TTT events

To discuss the performance of the model regarding the location of TTT events, part 4 of the results, namely the anchor points of the cloud bands, the position of the centroid and the tilt of the cloud bands, is taken into consideration.

7.4.1 Anchor points of the cloud bands

The anchor point of the cloud band is considered the north-western-most point of the cloud band. The geographical domain is divided into three regions according to the preferred regions where TTTs tend to develop.

As mentioned in chapter 6, a dilemma is faced when investigating the performance of the model regarding the anchor points of the cloud bands: the average position for the anchor points for seasons without any cloud bands in one of the regions is registered as 0˚S, 0˚E, which results in very strange averages with unusually large RMSE and percentage error values. Therefore, it is decided to rather use a graphical approach when considering the anchor points of the cloud bands.

The model performed reasonably well by modelling the latitude of the anchor points between 5˚S and 20˚S, when looking at a graphical representation of the modelled anchor points. There are a few anchor points around 19.5˚S, but that could be due to the difference in resolution between the observed and the modelled dataset (0.833º x 0.566º compared to 2.5° x 2.5°). Regarding the longitude, most of the modelled cloud bands fall within 15˚E and 68˚E. About 44% of all the ensemble members model cloud bands farther east than 68˚E. It is therefore plausible that the cloud bands within region 3 is misrepresented by the model, possibly because the GloSea5 tend to model the cloud bands slightly too far east. There seems to be no shift in modelled cloud bands in the other two regions. Another study with a larger geographical domain is necessary to prove or disregard this possibility.

A challenge arises when looking at the regions separately. This challenge comes from the fact that the observed and the modelled datasets have different resolutions. This difference in resolution poses difficulty if the anchor points within a specific region needs to be compared. Some ensemble members (about 33%) model the anchor points of the cloud bands in region 1 around the border of Angola and the Democratic Republic of Congo, as well as around the border of Angola and Namibia. A similar pattern is seen regarding the anchor points of the observed cloud bands in region 1. There are too few cloud bands observed in region 2 to make any assumption as to where these cloud bands tend to have their anchor points. The anchor points in region 3 are scattered between 5˚S and 20˚S, and 38˚E and 68˚E of both the observed and modelled cloud bands.

While graphically investigating the anchor points of the cloud bands, it is also discovered that the number of modelled cloud bands within a specific region compares well to that of the observed cloud bands within that region, i.e. the ensemble members modelled the most cloud bands within region 1 and the least in region 2, as is the case with the observed cloud bands.

In general, the ensemble members perform fairly good regarding the position of the anchor points of the cloud bands, as well as the number of cloud bands in each region. What perhaps can increase the performance of the model, is if the model and the observed dataset have the same resolution. The model has however a higher resolution than the observed values, and it would therefore be imprudent to reduce the resolution of the model just to study TTT events. It would be better to improve the resolution of the reanalysis data. Further investigation can include to compare the modelled number of cloud bands in each region with the observed values in more detail.

7.4.2 Position of the centroid

The centroid of a cloud band is the centre of mass of that particular cloud band. When looking at the centroids of the observed cloud bands, there is a clutter of centroids between 20˚S to 28˚S and 25˚E to 45˚E. The farthest north that the centroids form is about 17˚S and the farthest south observed centroid lies at approximately 34.5˚S. The westernmost centroid can be found at 19˚E and the easternmost one at 73˚E. There is also a smaller area containing a number of centroids, which can be found to the southeast of Madagascar in the southern Indian Ocean. Which is interesting about the larger cluttered area is that it includes the summer rainfall region of South Africa, as well as parts of tropical Mozambique, southern Zimbabwe and eastern

Botswana (hereafter referred to as the summer rainfall region of southern Africa). These areas tend to get ample rainfall during the months of November to February when it is a normal rainfall season (with the average amount of rainfall). The reason for the large amounts of rainfall could be related to the fact that the centre of mass of the TTT events tend to form above this area. November has been found to be the summer month over South Africa when TTT events contribute the most to the monthly rainfall totals (Hart et al, 2013). The question now is, did the ensemble members capture this "cluttered area", and if they did, how well did they capture it?

As is briefly discussed in one of the results chapters (Chapter 6, Section 6.2), the modelled centroids also lie more or less in the same region as the observed centroids. The modelled centroids fall south of 15˚S and the southernmost modelled centroid is found just north of 35˚S. Regarding the latitude, most modelled centroids can be found between 20˚E and 77˚E, with only three centroids forming between 19˚E and 20˚E. As with the observed centroids, the modelled centroids tend to "clutter" around the summer rainfall area of southern Africa. About 21 of the ensemble members (66.7%) also display the smaller clutter to the southeast of Madagascar with significantly more centroids in this smaller area than the rest of the geographical domain (except of course for the large cluttered area).

In general, the ensemble members perform well regarding the position of the centroid, capturing both the larger and the smaller "cluttered" areas correctly and with most of the centroids falling within similar boundaries as the observed centroids. Although the method followed to establish the performance of the model regarding the position of the centroids and the anchor points is not a statistical or mathematical process, this method still provides a good estimate on the performance of the model regarding these parameters.

7.4.3 Tilt of the cloud bands

The tilt of the cloud bands plays an important role on the effect a TTT event has across the sub-continent. If the cloud band is tilted more towards north-south or towards west-east, the TTT will fall across different parts of southern Africa. It could be above a more populated area or above a rural area. In the first case the TTT could potentially lead to flash flooding in urban areas, where in the latter case heavy rainfall could be profitable for farmers. Therefore, the tilt of the cloud bands is considered as part of the location of TTT events in this study.

The MetBot measures two tilts. The first tilt is a smaller section on a cloud band to first establish whether a cloud band falls within the criteria of the MetBot to flag cloud bands. This tilt is not part of the output file of the MetBot. The second tilt is that of the entire cloud band, which forms part of the output of the MetBot file. Therefore, it sometimes occurs that a cloud band has a positive tilt, whereas the criteria for a cloud band is that the tilt must be smaller than 0˚ and larger than -90˚. The flagged cloud bands with positive tilts are still considered as cloud bands, because they fit the original criteria of the MetBot. In practice, TTT events with a positive tilt has been observed on satellite imagery, but they are quite rare.

For completeness, both sets (the combined positive and negative tilts, as well as the negative tilts separately) are included in the results to investigate the difference in the outcome.

7.4.3.1 Positive and negative tilts combined

The average observed tilt for the entire study period is calculated as -36.94˚, while the average tilt of the 27 ensemble members calculates to -37.19˚. This results in a difference of 0.25˚ and a percentage error of 0.68%, which is smaller than the resolution of the model. It is therefore safe to state that the model performs extremely well when considering the cloud bands with both positive and negative tilts.

The reason for this positive result of the model could be because of the positive tilts that diminishes the effect of great negative tilts when calculating the average. For example, if a dataset contains a positive tilt of 80˚, it could possibly have an average tilt closer to 0˚ than a dataset with only negative tilts. Therefore, it is important to evaluate the performance of the model by only considering the negative tilts, the results of which are discussed in the following section.

The RMSE value and the corresponding percentage error of all the ensemble members calculates to 6.61˚ and 17.91% respectively. These values are higher than the average tilt error, but is considered here a more accurate way of evaluating the ensemble members. The RMSE values of the separate ensemble members are between 4.65˚ and 8.87˚, with the corresponding percentage error between 12.6% and 22.65%. These values are lower than the results of some of the parameters investigated during this project and although an error of around 18% is not ideal for a forecast model, the model can still be used to forecast the average tilt of the cloud bands, even when the cloud bands with positive tilts are included.

7.4.3.2 Negative tilts only

In this section of the results the cloud bands with positive tilts are omitted. For the observed cloud bands, the average tilt calculates to -38.55˚. For the modelled cloud bands of all 27 ensemble members an average tilt of -39.33˚ is obtained, which has a difference of 0.78˚ with the observed tilt and surmounts to an error 2.02%. This is slightly higher than the percentage error than what is obtained for the combined tilts, but a percentage error of just more than 2% is sill extremely low. Therefore, the model also fares impeccable regarding the modelling of the negatively tilted cloud bands.

The RMSE and the corresponding percentage error are calculated as 6.14˚ and 15.92% respectively. As in the previous section, these values are larger than the error calculated on the average tilt in the previous paragraph. However, RMSE is a better indication of the performance of a model, because in the calculation the error is squared, after which the square root is calculated. By squaring the error in the RMSE calculation the effect of the sign (positive or negative) on the value in the final result is nullified.

7.4.3.3 The comparison

It is possible that when the positive tilts are included, the average modelled tilt will be lower than when considering only the cloud bands with negative tilts, but that is not necessarily the case. For example, when a set of cloud bands contains only negative tilts, but all of the tilts are close to 0˚, the average tilt would also be closer to zero, than a set of cloud bands with positive and negative tilts, which fall within a great range. The question is how much of a difference the exclusion of the positive tilts makes. When subtracting the two average tilts, a value of 0.53˚ is obtained. Seeing that this is less than a degree, the difference will not necessarily be noted. However, when considering the RMSE values and the corresponding percentage errors,

the outcome is different. The modelling of the negatively tilted cloud bands results in a slightly lower RMSE (6.14˚) than the positive and negative tilts combined (6.61˚). The difference in percentage error of these two RMSE values is slightly greater (15.92% compared to 17.91%). It can therefore be said that the ensemble members perform slightly better when considering the negative tilts separately, but if only negative tilted cloud bands are considered, not all the possible cloud bands will be flagged, which will affect the seasonal forecast of TTT events by the model. Therefore, it is still important to consider the positively tilted cloud bands in a seasonal forecast for TTT events. However, for the location of these events the cloud bands with positive tilts should be omitted.

7.5 The Ensemble Members

Table 7.1 summarises the best and worst performers of the ensemble members for every parameter. There is no definitive "winner" under the different best performers. However, an ensemble average is also considered and recommended in order to investigate how the model performs as a whole and to be used in order to forecast TTT events on a seasonal scale. The performance of the model regarding the model average also depends on the lead-time of the forecast: most probably a shorter lead-time will result in a better forecast. However, most of the best performing ensemble members were initiated in September, which pose the question whether a shorter lead-time is really the best option for a seasonal forecast of TTT events in the case of the GloSea5 model.

The best and worst performing ensemble members for the anchor point and the centroid position, which forms part of the location of TTT events (subobjective 2.b), are not included in the table, because a visual presentation is used to compare these two parameters. By using visual inspection to establish best and worst performers, the results will be subjected to human error and it will not be scientifically viable.

What is interesting to note however is that the best performers changed in most of the cases when the bias is adjusted, for example with the number of cloud bands. Another positive result is that the worst performers are never the same when considering the average and the RMSE of a parameter. Therefore, by using this state-of-the-art seasonal forecast model to produce a

seasonal forecast for TTT events and equal weighting regarding the ensemble members will most probably be the best option.

Table 7.1: The best and worst performing ensemble members for every parameter investigated in this study. Each colour signifies a different characteristic of TTT events, which are: Frequency | Intensity | Location Ensemble member is abbreviated as EM.

Parameter	Sub-parameter	Ensemble member: best	Ensemble member: worst
Number of cloud bands	Percentage deviation	25 September EM 3	17 September EM 3
	RMSE	25 September EM 3	1 September EM 3
	RMSE: bias adjusted	17 October EM 3	1 November EM 1
Area	Average	1 September EM 3	17 September EM 2
	RMSE	1 September EM 3	17 September EM 2
	RMSE: bias adjusted	25 September EM 1	9 October EM 1
OLR: minimum	Average	17 October EM 1	1 September EM 3
	RMSE	17 October EM 3	1 September EM 3
OLR: maximum	Average	9 September EM 3	1 October EM 1
	RMSE	9 September EM 3	17 September EM 3
Tilt: Negative only	RMSE	1 November EM 3	1 October EM 1

The different ensemble members can also be evaluated by combining the different parameters that represents a characteristic of TTT events, for example the area of the modelled cloud bands combined with the minimum and maximum OLR thereof. This combination of different parameters can be considered in a follow-up study of this project.

7.6 The Model

It may be of interest to investigate how the ensemble members perform separately, but an ensemble of simulations will most probably be used on an operational level. In this section the overall performance of the GloSea5 is discussed by considering the ensemble average for the different characteristics of TTT events.

In table 7.2 a summary of the results for each parameter is tabulated. As can be seen in this table, the model under-performs regarding the number of cloud bands for the entire study period. The average area calculated for the cloud bands of the model is smaller than that of the

observed. The model performed reasonably well regarding the average minimum and maximum OLR values, as well as the tilt. The RMSE of the latter four parameters is below 10 with a percentage error of less than 20%. When considering only the percentage error, the model also performed good regarding the average area, since this value is also below 20%.

Table 7.2: A summary of the average values, the percentage deviation, the RMSE values and the percentage error of the different parameters investigated in this study, with the omission of the position of the anchor points and the centroids of the cloud bands. Not all of the RMSE values are bias-adjusted values.

Parameter (units, unless stated differently in the column headline)	Total/Average		Percentage deviation (%)	RMSE (bias-adjusted)	Percentage error (%)
	Observed	Model	Model	Model	Model
Number of cloud bands	523	355	-28.29	9.611171	26.23
Area (km^2)	35795	29893	*n/a*	4359.2	12.18
Minimum OLR ($W.m^{-2}$)	136.02	132.99	*n/a*	7.09	5.20
Maximum OLR ($W.m^{-2}$)	237.88	235.26	*n/a*	4.53	1.90
Tilt: Negative only (degrees)	-38.55	-39.33	*n/a*	6.14	15.92

For all the considered variables the model average is already calculated and discussed in the previous sections on the different parameters. Therefore, different lead-times will be considered in the subsections to follow. These lead-times will include a 2-month, a 1-month and a 0-month lead-time. For the 2-month lead-time the average of the results for the ensemble members initiated in September is used. The 1-month lead-time makes use of the average results of the ensemble members initiated in October. With a 0-month lead-time, the results of the ensemble members initiated on 1 November is used. For the latter only 3 ensemble members are used, while the other two lead-times consist of 12 ensemble members each.

7.6.1 The model: Frequency of TTT events

As was discussed in section 7.2, the different ensemble members under-predict the number of cloud bands. Inevitably the model also under-predicts the number of cloud bands. The results, including the bias-adjusted results are already discussed in section 7.2. What remains is to investigate whether the model performance increased with a shorter lead-time. Seeing that it is already established that a bias-adjustment is necessary, only these results will be discussed.

As can be seen in table 7.3, there is not much difference in the forecast skill of the different lead-times. With a 1-month lead-time, the RMSE and percentage error for the number of cloud bands is lower than for the other lead-times. That the RMSE and percentage error values of the 0-month lead-time is higher than that with a 1-month lead-time, could be due to the fact that only 3 ensemble members are used for the 0-month lead-time, while 12 ensemble members are averaged for the 1-month lead-time.

Table 7.3: The RMSE and the average percentage error of the different lead-times for the number of cloud bands predicted by the GloSea5 model.

Number of cloud bands: bias-adjusted		
Lead-time	RMSE	Error (%)
2-month	9.67	26.25
1-month	9.25	25.38
0-month	10.82	29.57

7.6.2 The model: Intensity of TTT events

As is the case in the section on the number of cloud bands, the different ensemble members also under-predict the average area of the cloud bands, the minimum OLR and the maximum OLR. Improved results are obtained for the ensemble mean by using a bias-adjustment in the case of the average area. The model performed better with the minimum and the maximum OLR values. Therefore, it was not necessary to adjust the bias in the latter cases.

In table 7.4 the RMSE and the percentage error of the different lead-times for the average area of the modelled cloud bands are displayed. From this table it can be seen that the ensemble members with a 1-month lead-time once again performed better than the other lead-times, but only by a small margin. The error remains above 10%, which will have to be taken into

consideration when using the GloSea5 model to forecast the intensity of TTT events across southern Africa during the summer rainfall season.

Table 7.4: The RMSE and the average percentage error of the different lead-times for the area of cloud bands as calculated by the GloSea5 model.

Area of cloud bands: bias-adjusted		
Lead-time	RMSE (km^2)	Error (%)
2-month	4396	12.3
1-month	4317	12.1
0-month	4387	12.3

In general, the ensemble members perform reasonably well with respect to the minimum OLR values. The RMSE values are below 10 $W.m^{-2}$ and the percentage errors are well below 10% (table 7.5). The 1-month lead-time forecast for the minimum OLR values however clearly out-performs the 2-month and 0-month lead-times with more than 1% difference. Regarding the minimum OLR, it can be concluded that the GloSea5 model performs well and can therefore be used to forecast seasonal minimum OLR values for TTT events.

Table 7.5: The RMSE and the average percentage error of the different lead-times for the minimum OLR of the cloud bands as modelled by the GloSea5 ensemble members.

Minimum OLR		
Lead-time	RMSE ($W.m^{-2}$)	Error (%)
2-month	8.22	6.02
1-month	5.89	4.32
0-month	7.39	5.42

The GloSea5 model performs even better with the maximum OLR values than with the minimum OLR values. Most of the RMSE values of the average maximum OLR forecast values are below 5 $W.m^{-2}$, with the corresponding percentage errors below 2% (table 7.6). Once again, the average of the ensemble members with a 1-month lead-time is the lowest with an error of 1.84%. The GloSea5 model can therefore also be used to forecast the seasonal average maximum OLR values of TTT events.

Table 7.6: The RMSE and the average percentage error of the different lead-times for the minimum OLR of the cloud bands as modelled by the GloSea5 ensemble members.

Maximum OLR		
Lead-time	RMSE ($W.m^{-2}$)	Error (%)
2-month	4.69	1.97
1-month	4.39	1.84
0-month	4.45	1.87

7.6.3 The model: Location of TTT events

In the previous chapters and in section 7.4 it is established that the different ensemble members in general perform well regarding the position of the anchor point and the centroid of the cloud bands. Due to the fact that the RMSE and percentage error are not calculated for the position of the anchor point and the centroid, the different lead-times cannot be considered in the same way as with the other studied parameters. With these two parameters, a graphical representation will need to be used to establish whether or not the model performs better at different lead-times. In order to compare the different lead-times, all the ensemble members initiated within a specific calendar month (September, October or November) will have to be combined to establish the performance of the model, a study that can perhaps be considered in the future. However, seeing that the individual ensemble members perform well regarding these two parameters, regardless of the lead-time of the forecast, it can be concluded that the model as an ensemble average will also perform well.

The third parameter investigated regarding the location of TTT events is the tilt of the cloud bands. As was discussed to length in section 7.4.3, two separate sets are investigated, namely positive and negative tilts combined and negative tilts separately. Seeing that the positive tilts affect the results in such a way that a true average cannot be obtained, only the results of the negative tilted cloud bands are discussed.

The same conclusion applies to the set with only the negative tilts as for the combined set: although the RMSE values are relatively low (below 10˚E), the percentage error is still above 10%. Therefore, this margin of error needs to be accounted for when using the GloSea5 model. Once again, the model performs marginally better with the shortest lead-time (table 7.8). This small difference between the modelled and the forecast average tilt of TTT events does not affect the location of the TTT significantly.

Table 7.8: The RMSE and the average percentage error of the different lead-times for the cloud bands with negative tilts as modelled by the GloSea5 model.

Negative tilts		
Lead-time	RMSE (˚E)	Error (%)
2-month	6.10	15.87
1-month	6.23	16.12
0-month	5.94	15.35

7.6.4 The model: a short summary

In general, the model is able to forecast TTT-events to a good degree. With most of the parameters the 1-month lead-time forecast is the most accurate. The 1-month lead-time forecast consists of forecasts from ensemble members 1, 2 and 3 initiated on 1, 9, 17 and 25 October. It is only in the case of the negative tilts, that the 0-month lead-time forecast is more accurate than that of the 1- and 2-month lead-times. As was discussed in the various sub-sections on the tilts of the cloud bands, by only considering the negative tilts separately not all of the modelled cloud bands are being investigated.

7.7 ENSO and modelled TTT events

The correlation between ENSO (El Niño-Southern Oscillation) and the characteristics of TTT events was briefly discussed in the previous sections and chapters. What stands particularly out in the results is that during some years (in both the observed and modelled datasets) the number, area, etc. of cloud bands are significantly greater or smaller than other years. This could perhaps be due to an association with ENSO.

ENSO is a phenomenon that presents itself in the tropical eastern Pacific Ocean. It has to do with the irregular variation in the wind and the sea-surface temperatures over the tropical Pacific Ocean. This phenomenon affects the climate in the tropics and subtropics across much of the world. It consists of three phases, which relate to the Walker Circulation, namely the warming phase (El Niño), the neutral phase and the cooling phase (La Niña). The Walker Circulation is the globular flow of air in the troposphere of the tropics. During the warm El Niño phase, the summer rainfall region of southern Africa typically receives below-normal

rainfall, while the cooler La Niña phase usually implies above-normal rainfall (Fauchereau et al, 2009; Wallace & Hobbs: 431-438, 2006).

During the study period considered in this project, there were five El Niño years and six La Niña years. The rainfall in these years were not always as one would expect during ENSO events, for example in the El Niño year 1997/1998 some areas of the summer rainfall regions of South Africa received above-normal rainfall during mid-summer (e.g. Lyon and Mason, 2007). This particular ENSO event was one of the strongest El Niño events on record (e.g. Fauchereau et al, 2009; L'Heureux et al, 2017). During the 2005/2006, 2007/2008 and 2008/2009 La Niña years, South Africa did not receive above-normal rainfall. These three cooling ENSO events were however considered as weak La Niña's, which could have contributed to the amount of rainfall received across southern Africa. The different ENSO phases and the strength thereof during the 14 studied seasons in this project, are displayed in table 7.9.

Figure 7.1 displays the number of observed cloud bands for each season during the study period, colour coded according to the different ENSO phases (and the strength thereof) during the particular season. The strongest El Niño during the studied period resulted in the second-most observed cloud bands and the strongest La Niña of 1998/1999 in the most cloud bands. The least cloud bands per season are observed during the weak El Niño of 2006/2007. Although the most cloud bands are observed during a La Niña year and the least in an El Niño year, it cannot be confirmed that there is a linear relationship between the observed number of cloud bands and ENSO phases.

Table 7.9: The ENSO phases of the 14 seasons studied in this project. El Niño years are coloured red and La Niña years blue. The strength of the ENSO phase (weak, moderate, strong or very strong) is indicated with an X. In this classification the Niño 3.4 index is used.

	El Niño/La Niña	Weak	Moderate	Strong	Very strong
1996/1997	Neutral				
1997/1998	El Niño				X
1998/1999	La Niña			X	
1999/2000	La Niña			X	
2000/2001	La Niña	X			
2001/2002	Neutral				
2002/2003	El Niño		X		
2003/2004	Neutral				
2004/2005	El Niño	X			
2005/2006	La Niña	X			
2006/2007	El Niño	X			
2007/2008	La Niña			X	
2008/2009	La Niña	X			
2009/2010	El Niño			X	

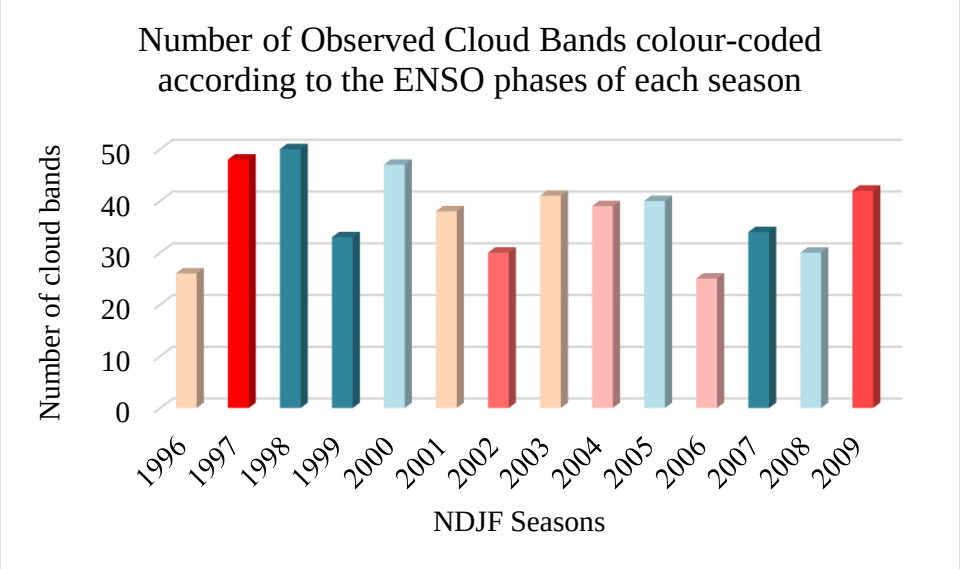

Figure 7.1: The number of observed cloud bands colour-coded according to the ENSO phases of each season. Red indicates El Niño years, the green bars designate the neutral years and blue relates to La Niña years. The strength of the ENSO phase is indicated by the intensity of the colour (a darker colour indicates a stronger event).

As discussed in the previous paragraph, the observed number of cloud bands do not necessarily correlate to the ENSO phase of each season, but perhaps the number of modelled cloud bands do. Therefore, the analysis is repeated using the ensemble averaged number of cloud bands. The modelled number of cloud bands are displayed in figure 7.2. What stands particularly out is that the seasons with the least cloud bands are all El Niño years (2002/2003 and 2009/2010), and the seasons with the most cloud bands are La Niña and neutral years (1996/1997, 1998/1999 and 2005/2006). For the rest of the seasons there is no distinct correlation to ENSO, because there are El Niño years with more cloud bands than La Niña years. For example, the season of 2004/2005 and 2006/2007 are weak El Niño years with a relatively high number of cloud bands, while the seasons of 2007/2008 and 2008/2009 are strong and weak La Niña years, but with a relatively low number of cloud bands.

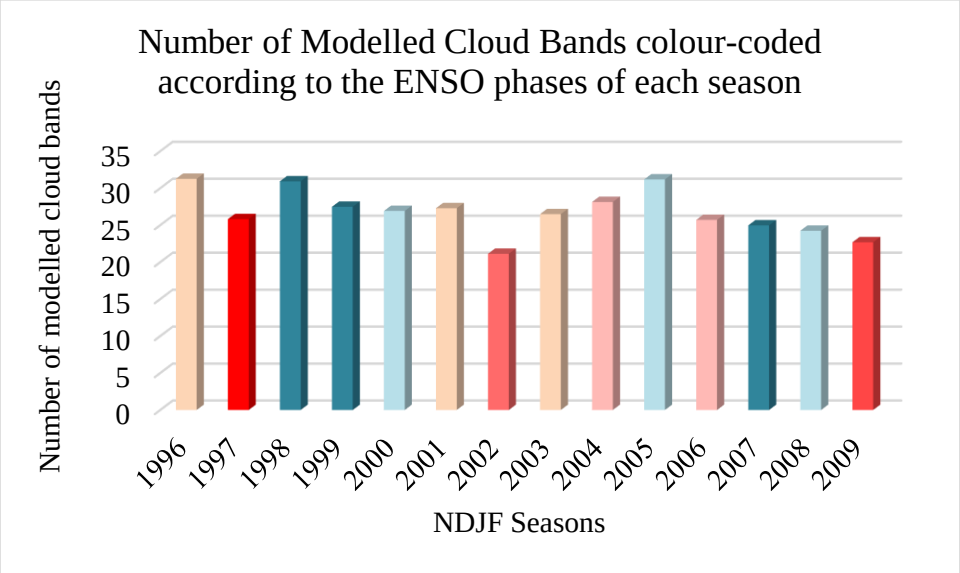

Figure 7.2: The number of modelled cloud bands colour-coded according to the ENSO phases of each season. Red indicates El Niño years, the green bars designate the neutral years and blue relates to La Niña years. The strength of the ENSO phase is indicated by the intensity of the colour (a darker colour indicates a stronger event).

To fully establish the relation between ENSO and TTT events, a more detailed investigation is necessary, which is however not part of the scope of this project. A preliminary test with only the number of cloud bands did not yield a definitive link between ENSO and TTT events with regards to the observations and the modelled data. More on possible future studies will be discussed in the next chapter (Chapter 8: Conclusion).

This section (and chapter) concludes with a preliminary investigation on how the model performs regarding the forecast of TTT events during different ENSO years. A link between the inter-annual variability of TTT events and ENSO has already been established in previous studies (Manhique et al, 2011). In the following and final chapter of this project a conclusion, as well as possible future studies that can be considered on this topic of TTT events, are presented.

CHAPTER 8: Conclusion and Future Work

The skill of numerical models is constantly improving, but in order to know the margin of this improvement, it is necessary to investigate how these numerical models predict specific weather scenarios. That is the aim of this project: to investigate the predictability of TTT events across southern Africa on a seasonal time-scale by using a state-of-the-art seasonal forecast model. The research question therefore is: What is the ability of a state-of-the-art seasonal forecast model to simulate TTT characteristics over southern Africa? To address this research question, certain objectives have been set aside:

1. Identify modelled cloud bands associated with TTT events using gridded data
2. Investigate the characteristics of modelled TTT events using the gridded data:
    a. Frequency of TTT occurrences
    b. Location of TTT events across southern Africa
    c. Intensity of TTT events over southern Africa

The objectives and sub-objectives have each been investigated separately for the 27 ensemble members of the GloSea5 forecasting model of the UK Met Office initialised between 1 September and 1 November for NDJF of 1996/1997 to 2009/2010, by looking at the different aspects of the identified cloud bands, such as their anchor point and their surface area. In chapters 3, 4, 5 and 6 the results have been presented and in chapter 7 these results have been discussed in detail. After the different ensemble members are investigated separately, the ensemble average is calculated.

By using the MetBot, the cloud bands associated with TTT events can easily be identified in both the observed and the modelled datasets. Therefore, by capturing the cloud bands using the MetBot, objective 1 is achieved. Regarding the rest of the objectives, it has been found that the model performs fairly well for certain characteristics of TTT events, such as the average minimum and maximum OLR values (which relates to the intensity of TTT events) and not as well regarding other characteristics, namely the number of cloud bands (which relates to the frequency of TTT occurrences within the summer season). However, the fact that the model is able to identify TTT events on a seasonal timescale and to forecast these events to a certain extent, is encouraging.

The GloSea5 model has performed the best regarding the average minimum and maximum OLR values. Due to the fact that the OLR is a key parameter with the identification of TTT events across southern Africa and the fact that it provides an indication of the intensity of these events, this result is of significance since it provides evidence that the GloSea5 model can be successfully used to forecast the intensity of TTT events on a seasonal time-scale, albeit with a small margin of error.

To expand on the investigation of the predictability of TTT events by a state-of-the-art seasonal forecasting model, additional work will have to be performed which takes, for example, the rainfall amounts and other circulation dynamics, such as the convergence and divergence zones around TTT events, also into consideration. An important further study would be to explore the physical mechanism(s) related to the under-prediction of TTT events within the summer season across southern Africa. The proposed additional work is outside the scope of this project, since this study only uses modelled and observed OLR values to investigate whether or not TTT events can be predicted on a seasonal time-scale, which is sufficient to address the research question and the different objectives.

The discussion chapter (chapter 7) ends with a quick investigation of the predictability of the number of TTT events occurring during the summer rainfall season of southern Africa during ENSO years. It could not be confirmed whether there is a linear relationship between the number of cloud bands (observed and modelled) and ENSO phases. The study period will have to be lengthened to further investigate a possible link between wetter La Niña/drier El Niño seasons and the number of TTT events modelled/observed during a summer season in southern Africa.

Future work

While investigating the frequency of TTT events, it has been noted that there might be a possibility that the model forecast TTT events slightly farther east or west than the considered geographical domain. A future study could therefore be done by using a greater geographical domain. In this manner, if the model reproduces cloud bands farther west or farther east of the geographical domain considered in this study, the number of TTT events will increase, i.e. the frequency thereof. However, a larger geographical domain could also increase the number of

observed cloud bands (even though previous studies are consistent on the area where TTTs tend to develop across southern Africa), but it might still be worthwhile to investigate.

Due to the nature of the investigation regarding the position of the anchor point and the centroid of the cloud bands (a visual representation is used), the RMSE and the percentage error is not calculated. A possible issue that can arise from using the visual-representation method is that there is room for human error, because it relies on approximations using subjective methods. The characteristics could be further investigated by combining ensemble members to produce forecasts with different lead-times. A possible solution to exclude human error in the investigation of the anchor point and the centroid of the modelled cloud bands, could be to use cluster analysis or boxplots.

During the investigation it has been noted that certain seasons produced significantly higher values of specific parameters than other seasons in both the observed and the modelled datasets. This anomaly lead to the question: did ENSO play a part in the modelled (and observed) characteristics of TTT events during these seasons? The reason behind this argument is that it is known that ENSO influences seasonal rainfall across southern Africa. A preliminary study has been done in chapter 7 to investigate whether the seasons with a significantly higher number of cloud bands (observed and modelled) were in fact during El Niño or La Niña years. No definitive association has been found; however, a more in-depth study could certainly be useful in investigating this possible relationship further. This investigation could be combined with a study regarding the Southern Indian Ocean Oscillation/Dipole. It has already been found that the Southern Indian Ocean Oscillation/Dipole has a connection to the seasonal rainfall across southern Africa (Behera and Yamagata, 2001), and perhaps an even greater connection when compared to ENSO or specific ENSO events. To elaborate the study further, the three preferred regions where TTT's tend to develop, could also be taken into consideration.

Another definitive opportunity for future studies to further advance our understanding of TTT events is to use observed (and modelled) rainfall data, for example to investigate whether the model predicts heavy rain in a small area of the geographical domain during seasons with relatively more TTT events. The relation between the minimum OLR values and the rainfall data can also be investigated.

All of the above mentioned “future studies” do not fall within the scope of this study, seeing that these studies are not necessary to address the research question and the different objectives. These possible future studies are mere suggestions as to how the predictability of TTT events by a state-of-the-art seasonal forecasting model can further be enhanced, should one wish to do so.

Final remarks

The study on the ability of a state-of-the-art seasonal forecast model to forecast the characteristics of TTT events on a seasonal timescale is a original study: It has never been done before. The fact that the GloSea5 forecasting model can identify TTT events and can most certainly forecast the different characteristics associated to TTT events to a great extent, is a ground breaking discovery in the field of numerical weather prediction. From the results it can be concluded that the GloSea5 forecasting model can be used to forecast the intensity of TTT events, as this characteristic mainly depends on the minimum and the maximum OLR values, as well as the area. Although the model performs less well with the geographical extent of TTT events (the area), the average percentage error is still less than 15%. The location of TTT events is also captured well by the GloSea5. The model had some difficulty in forecasting the frequency of TTT occurrences, however when taking about a 25% margin of error into account, the model can also be used to forecast the number of TTT events within a summer rainfall season across southern Africa. Lastly, in forecasting most of the parameters, the model performed best with a 1-month lead-time. Therefore, the seasonal forecast obtained in October will probably be the most accurate.

In conclusion this study has successfully addressed the objectives of the work. It has demonstrated that different characteristics of TTT events can be captured and therefore forecast on a seasonal timescale by a state-of-the-art seasonal forecast model. Contemporary weather models most certainly have come a long way.

This study is one of the first of its kind with positive results for the investigation of the different characteristics of a specific weather system on a seasonal timescale. This original study has therefore most certainly contributed to the research on the forecast ability of seasonal forecasting models, as well as the research of these fascinating weather phenomena across southern Africa.

REFERENCES

Ahrens, C.D., 2007: *Meteorology today: An introduction to weather, climate and the environment*, 8th edition, Canada, Thomson Brooks/Cole, 35-38, 450.

Arribas, A., Glover, M., Maidens, A., Peterson, K., Gordon, M., MacLachlan, C., Graham, R., Fereday, D., Camp, J., Scaife, A.A., Xavier, P., McLean, P., Colman, A. and Cusack, S., 2011: The GloSea4 ensemble prediction system for seasonal forecasting, *Monthly Weather Review*, **139**, 1891-1910.

Behera S.K. and Yamagata, T., 2001: Subtropical SST dipole events in the southern Indian Ocean, *Geophysical Research Letters*, **28 (2)**, 327-330.

Bjerknes, V., 1904: Das Problem der Wettervorhersage, betrachtet vom Standpunte der Mechanik und der Physik, *Meteorologische Zeitschrift*, **21**, 1-7.

Blamey, R.C. and Reason, C.J.C., 2009: Numerical simulation of a mesoscale convective system over the east coast of South Africa, *Tellus*, **61A**, 17-34.

Bolin, B, 1955: Numerical forecasting with the barotropic model, *Tellus*, **VII**, 1, 27-49.

Coiffier, J., 2011: Fundamentals of numerical weather prediction, Cambridge University Press, 276-281.

Bowler, N., Arribas, Al, Beare, S., Mylne, K.E. and Shutts, G., 2009: Th local ETKF and SKEB: Upgraders to the MOGREPS short-range ensemble prediction system, *Quarterly Journal of the Royal Meteorological Society*, **135**, 767-776.

Cook, K.H., 2000: The south Indian Ocean convergence zone and interannual rainfall variability over southern Africa, *Journal of Climate*, **13**, 3789-3804.

Crimp, S.J., Lutjeharms, J.R.E. and Mason, S.J., 1998: Sensitivity of a tropical-temperate trough to sea-surface temperature anomalies in the Agulhas retroflection region, *Water SA*, **24**, 93-101.

D'Abreton, P.C. and Tyson, P.D., 1995: Divergent and non-divergent water vapour transport over southern Africa during wet and dry conditions, *Meteorology and Atmospheric Physics*, **55**, 47-59.

De Coning, E., Forbes, G.S. and Poolman, E., 1998: Heavy precipitation and flooding on 12-14 February 1996 over the summer rainfall regions of South Africa: synoptic and isentropic analyses, *National Weather Digest*, **22**, 3, 26-36.

Fauchereau, N., Pohl, B., Reason, C., Rouault, M. and Richard, Y., 2009: Recurrent daily OLR patterns in the southern Africa / southwest Indian Ocean region, implications for South African rainfall and teleconnections, *Climate Dynamics*, **32**, 575-591.

Fox, D.G., 1981: Judging air quality model performance, *Bulletin American Meteorological Society*, **62**, 599-609.

Graham, R.J., Gordon, M., Mclean, P.J., Ineson, S., Huddleston, M.R., Davey, M.K., Brookshaw, A. and Barnes, R.T.H., 2005: A performance comparison of coupled and uncoupled versions of the Met Office seasonal prediction general circulation model, *Tellus*, **57A**, 320-339.

Harangozo, S. and Harrison, M.S.J., 1983: On the use of synoptic data indicating the presence of cloud bands over southern Africa, *South African Journal of Science*, **79**, 413-414.

Harrison, M.S.J., 1984: A generalized classification of South African summer rain-bearing synoptic systems, *International Journal of Climatology*, **4**, 547-560.
Hart, N.C.G., Reason, C.J.C. and Fauchereau, N., 2010: Tropical-extratropical interactions over southern Africa: Three cases of heavy summer season rainfall, *Monthly Weather Review*, **138**, 2608-2609.
Hart, N.C.G., Reason, C.J.C. and Fauchereau, N., 2012: Building a tropical-extratropical cloud band metbot, *Monthly Weather Review*, **140**, 4005-4016.
Hart, N.C.G., Reason, C.J.C. and Fauchereau, N., 2013: Cloud bands over southern Africa: seasonality, contribution to rainfall variability and modulation by the MJO, *Climate Dynamics*, **41**, 1199-1212.
Holton, J.R. and Hakim, G.J., 2013: An introduction to dynamic Meteorology 5th edition, Elsevier Inc, 159-160.
Knippertz, P., Fink, A.H., Reiner, A. and Speth, P., 2003: Three late summer/early autumn cases of tropical-extratropical interactions causing precipitation in northwest Africa, *Monthly Weather Review*, **131**, 116-135.
Knippertz, P., 2005: Tropical-extratropical interactions associated with an Atlantic tropical plume and subtropical jet streak, *Monthly Weather Review*, **133**, 2759-2776.
Knippertz, P., 2007: Tropical-extratropical interactions related to upper-level troughs at low latitudes, *Dynamics of Atmospheres and Oceans*, **43**, 36-62.
Landman, W.A., De Witt, D., Lee D.E., Beraki, A. and Lötter, D., 2012a: Seasonal rainfall prediction skill over South Africa: 1- vs. 2-tiered forecasting systems, *Weather and Forecasting*, **27**, 489-501.
Landman, W.A., Graham, R., Knight, J., Engelbrecht, C. and Olivier, C., 2012b: Assessment of GloSea4 seasonal forecasts for SADC and the global oceans, SASAS, 26-27 September 2012, 102-103.
Liebmann, B. and Smith, C.A., 1996: Description of complete (interpolated) outgoing longwave radiation dataset, *Bulletin of the American Meteorological Society*, **77**, 1275-1277.
Lorenz, E.N., 1963: Deterministic non-periodic flow, *Journal of the Atmospheric Sciences*, **20**, 130-141.
MacLachlan, C., Arribas, A., Peterson, K.A., Maidens, A., Fereday, D., Scaife, A.A., Gordon, M., Vellinga, M., Williams, A., Comer, R.E., Camp, J., Xavier, P. and Madec, G., 2014: Global seasonal forecast system version 5 (GloSea5): a high-resolution seasonal forecast system, *Quarterly Journal of the Royal Meteorological Society*, DOI:10.1002/qj.2396.
Macron, C., Pohl, B., Richard, Y. and Bessafi, M., 2014: How do tropical temperate troughs form and develop over southern Africa?, *Journal of Climate*, **27**, 1633-1647.
Manhique, A.J., Reason, C.J.C., Rydberg, L. and Fauchereau, N., 2011: ENSO and the Indian sea surface temperatures with tropical temperate troughs over Mozambique and the southwest Indian Ocean, *International Journal of Climatology*, **31**, 1-13.
McGuirk, J.P., Thompson, A.H. and Smith, N.R, 1987: Moisture bursts over the tropical Pacific Ocean, *Monthly Weather Review*, **115**, 787-798.
Mogensen, K., Balmaseda, M., Weaver, A.T., Martin, M. and Vidard, A., 2009: NEMOVAR: A variational data assimilation system for the NEMO ocean model, *ECMWF Newsletter*, Walter Z. (ed.) **120**: 17-21, ECMWF: Reading, UK.

Mogensen, K., Balmaseda, M.A. and Weaver, A.T., 2012: The NEMOVAR ocean data assimilation system as implemented in the ECMWF ocean analysis for System 4, *Technical Report*, TR-CMGC-12-30, CERFACS: Toulouse, France.
Muller, A., Reason, C.J.C. and Fauchereau, N., 2007: Extreme rainfall in the Namib Desert during late summer 2006 and influences of regional ocean variability, *International Journal of Climatology*, **28**, 1061-1070.
NASA (National Aeronautics and Space Administration), 2014: The NASA's Earth Energy Budget Poster, https://science-edu.larc.nasa.gov/energy_budget/
Novella, N.S. and Thiaw, W.M., 2013: African rainfall climatology version 2 for famine early warning systems, *Journal of Applied Meteorology and Climatology*, **52**, 588-606.
Pohl, B., Fauchereau, N., Richard, Y., Rouault, M. and Reason, C., 2009: Interactions between synoptic, intraseasonal and interannual convective variability over southern Africa, *Climate Dynamics*, **33**, 1033-1050.
Ratna, B.S., Behera, S., Ratnam, J.V., Takahashi, K. and Yamagata, T., 2013: An index for tropical temperate troughs over southern Africa, *Climate Dynamics*, **41**, 421-441.
Rawlins, F., Ballard, S.P., Bovis, K.J., Clayton, A.M., Li, D., Inverarity, G.W., Lorenc, A.C. and Payne, T.J., 2007: The Met Office global four-dimensional variational data assimilation scheme, *Quarterly Journal of the Royal Meteorological Society*, **133**, 347-362.
Reason, C.J.C., Landman, W.A. and Tennant, W., 2006: Seasonal to decadal prediction of the southern African climate and its links with the variability of the Atlantic Ocean, *Bulletin of the American Meteorological Society*, **87**, 941-955.
Richardson, L.F., 1922: Weather Prediction by Numerical Process, Cambridge University Press, 1-3.
Scaife, A.A., Arribas, A., Blockleay, E., Brookshaw, A., Clark, R.T., Dunstone, N., Eade, R., Fereday, D., Folland, C.K., Gordon, M., Hermanson, L., Knight, J.R., Lea, D.J., MacLachlan, C., Maidens, A., Martin, M., Peterson, A.K., Smith, D., Vellinga, M., Wallace, E., Waters, J. and Williams, A., 2014: Skilful long-range prediction of European and North American winters, *Geophysical Research Letters*, **41**, 2514-2519.
Schuman, F.G., 1989: History of numerical weather prediction at the National Meteorological Centre, *Weather and Forecasting*, **4**, 286-296.
Todd, M. and Washington, R., 1999: Circulation anomalies associated with TTT in southern Africa and the southwest Indian Ocean, *Climate Dynamics.*, **15**, 937-951.
Todd, M., Washington, R. and Palmer, P.I., 2004: Water vapour transport associated with tropical-temperate trough systems over southern Africa and the southwest Indian Ocean, *International Journal of Climatology*, **24**, 555-568.
Tracton, M.S. and Kalnay, E., 1993: NMC Notes: Operational ensemble prediction at the National Meteorological Centre: Practical analysis, *Weather and Forecasting*, **8**, 379-398.
UK Met Office website, April 2012: Overview of the Met Office: Technology - Computers and Satellites, [accessed 19 May 2016], www.metoffice.gov.uk
UK Met Office website, November 2015: 50 years of numerical weather prediction (NWP) system by the Met Office, [accessed 9 Augustus 2016], www.metoffice.gov.uk
Vigaud, N., Pohl, B. and Crétat, J., 2012: Tropical-temperate interactions over southern Africa simulated by regional climate model, *Climate Dynamics*, **39**, 2895-2916.

Wallace, J.M. and Hobbs, P.V., 2006: *Atmospheric Science: An introductory Survey*, 2nd edition, Canada, Elsevier Inc., 1-15, 113-114, 120-121, 139, 144.
Washington, R. and Todd, M., 1999: Tropical temperate links in southern Africa and the southwest Indian Ocean daily rainfall, *International Journal of Climatology*, **19**, 1601-1616.
Weedon, G.P., Gomes, S., Viterbo, P., Shuttleworth, S.J., Blyth, E., Österle, H., Adam, J.C., Bellouin, N., Boucher, O. and Best, M., 2011: Creation of the WATCH forcing data and its use to assess global and regional reference crop evaporation over land during the twentieth century, *Journal of Hydrometeorology*, **12**, 823-848.
Wilks, D.S., 2011: *Statistical methods in the Atmospheric Sciences*, 3rd edition, USA, Elsevier Inc., 359.
Williams, C.J.R., Kniveton, D.R. and Layberry, R., 2007: Climatic and oceanic associations with daily rainfall extremes over southern Africa, *International Journal of Climatology*, **27**, 93-108.
Willmott, C.J., 1982: Some comments on the evaluation of model performance, *Bulletin American Meteorological Society*, **63**, 1309-1313.

APPENDIX A: Average area of the modelled cloud bands

This appendix consists of the graphs with the average area of the cloud bands per NDJF Seasons as modelled by the 27 different ensemble members for the study period November, December, January and February of the years 1996/1997 to 2009/2010. In all the graphs below the x-axis indicates the different NDJF Seasons in the study period and the y-axis donates the average area in km^2. Both the biased (green line) and the bias-adjusted (yellow line) average area-graphs are presented. The observed average area of the cloud bands per NDJF Seasons is displayed as a blue line on each graph. The abbreviations used for the 27 different ensemble members are given in the table below (table 3.1).

Table 3.1: A list of the abbreviation used for each ensemble member in this chapter and the following results chapters. The date in the second and forth column is the date on which the ensemble member is initiated.

Abbreviation	Ensemble member (EM)	Abbreviation	Ensemble member (EM)
1S1	1 September EM 1	1O3	1 October EM 3
1S2	1 September EM 2	9O1	9 October EM 1
1S3	1 September EM 3	9O2	9 October EM 2
9S1	9 September EM 1	9O3	9 October EM 3
9S2	9 September EM 2	17O1	17 October EM 1
9S3	9 September EM 3	17O2	17 October EM 2
17S1	17 September EM 1	17O3	17 October EM 3
17S2	17 September EM 2	25O1	25 October EM 1
17S3	17 September EM 3	25O2	25 October EM 2
25S1	25 September EM 1	25O3	25 October EM 3
25S2	25 September EM 2	1N1	1 November EM 1
25S3	25 September EM 3	1N2	1 November EM 2
1O1	1 October EM 1	1N3	1 November EM 3
1O2	1 October EM 2		

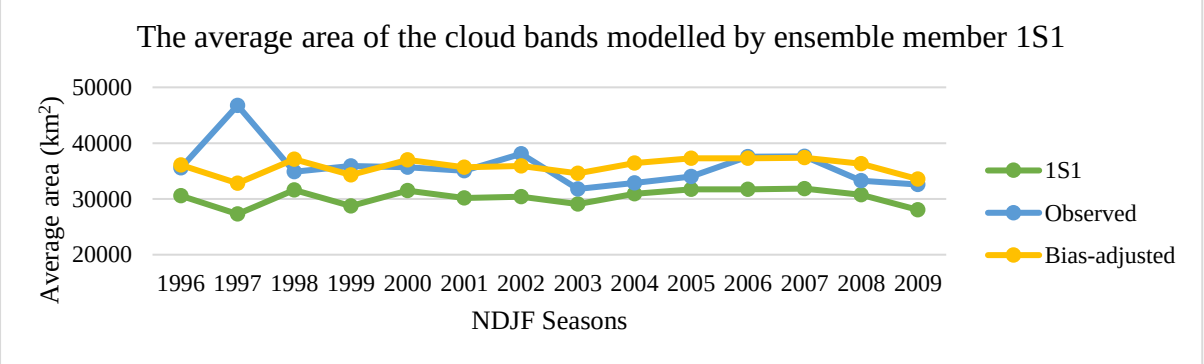

Figure A 1: The average area of the cloud bands for ensemble member 1S1.

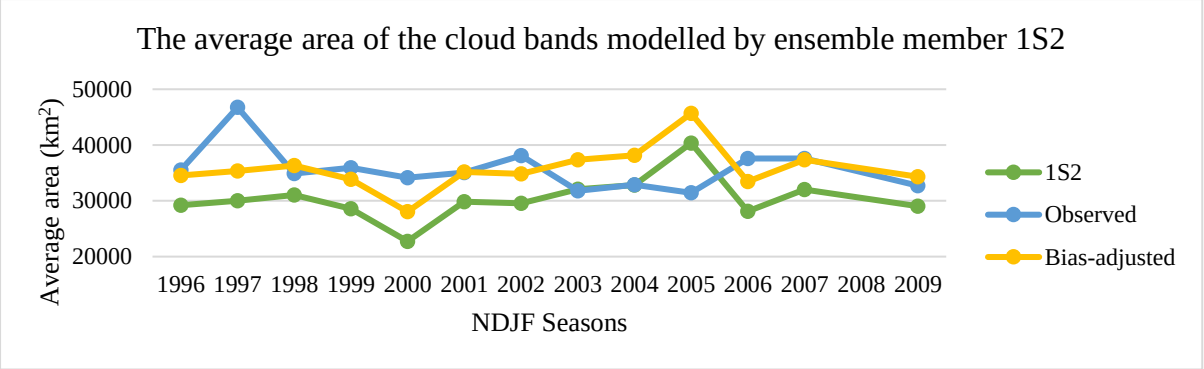

Figure A 2: The average area of the cloud bands for ensemble member 1S2.

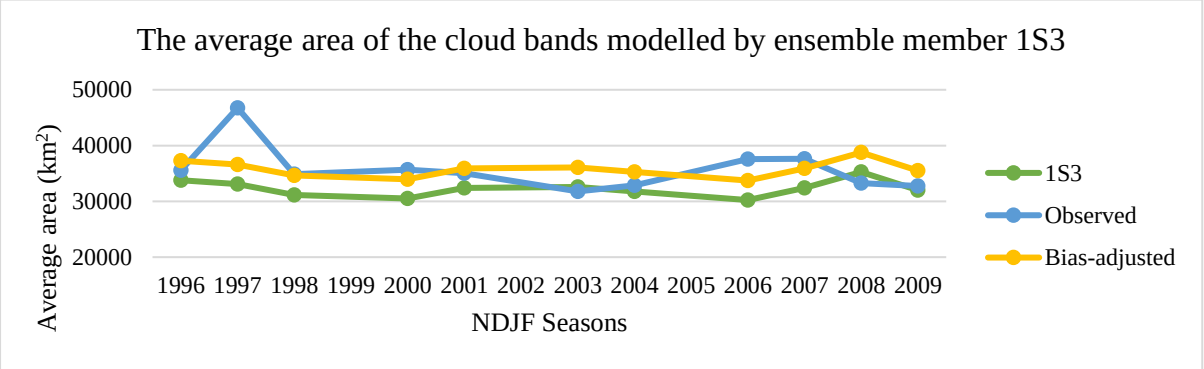

Figure A 3: The average area of the cloud bands for ensemble member 1S3.

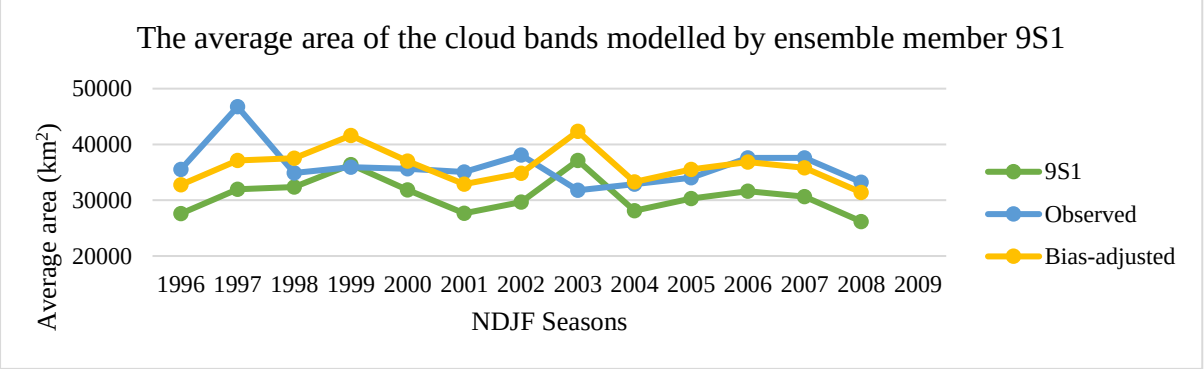

Figure A 4: The average area of the cloud bands for ensemble member 9S1.

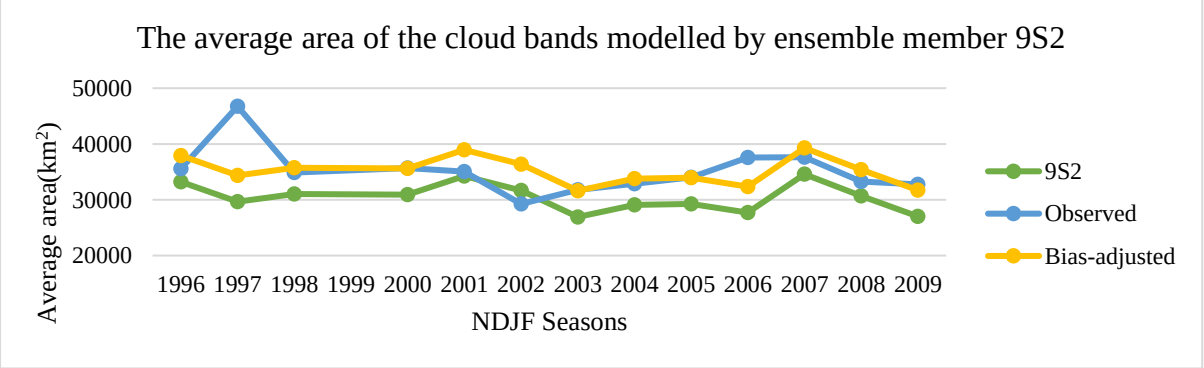

Figure A 5: The average area of the cloud bands for ensemble member 9S2.

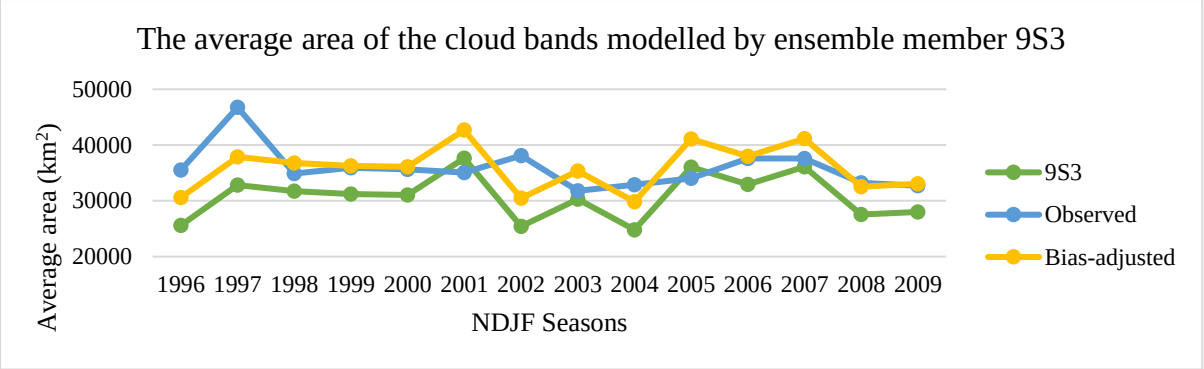

Figure A 6: The average area of the cloud bands for ensemble member 9S3.

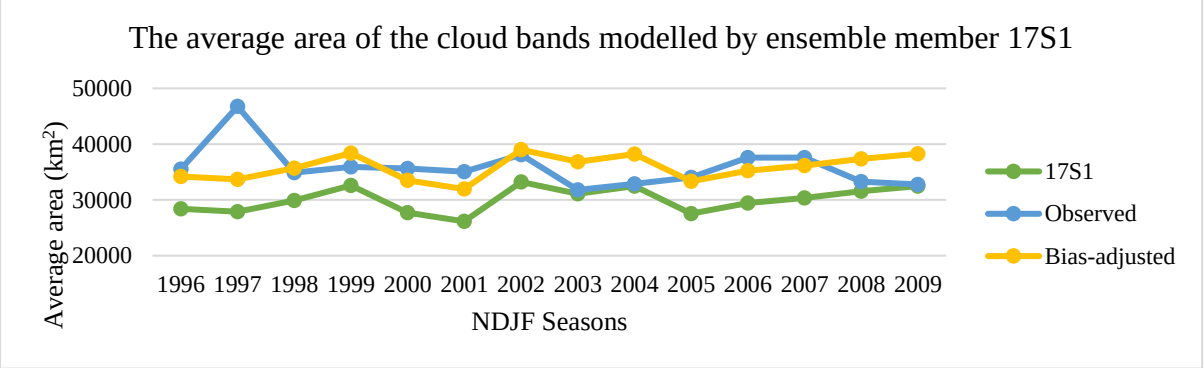

Figure A 7: The average area of the cloud bands for ensemble member 17S1.

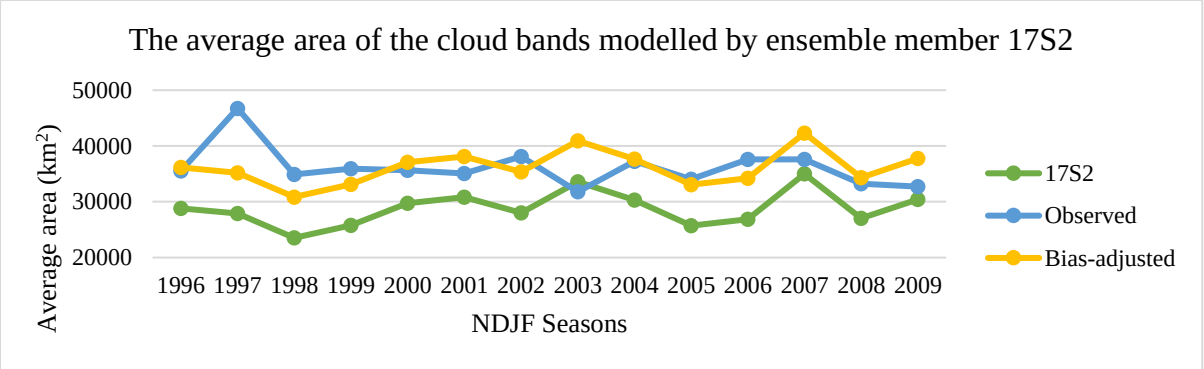

Figure A 8: The average area of the cloud bands for ensemble member 17S2.

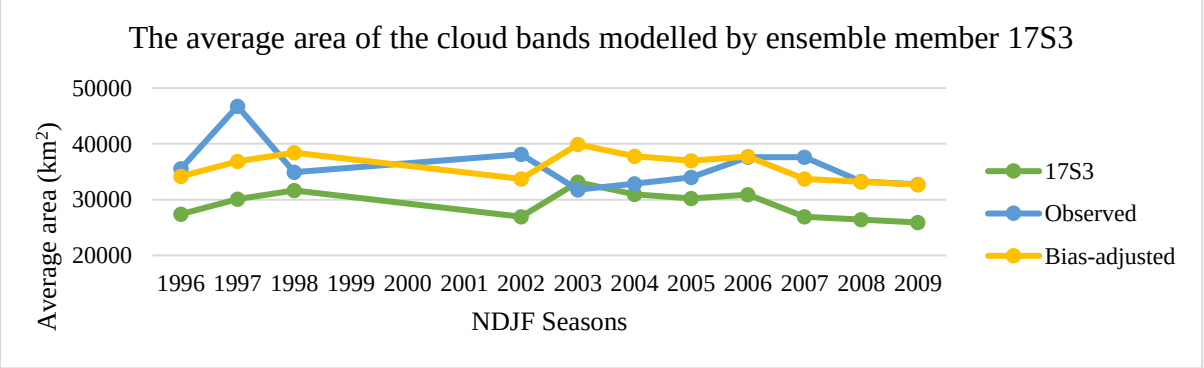

Figure A 9: The average area of the cloud bands for ensemble member 17S3.

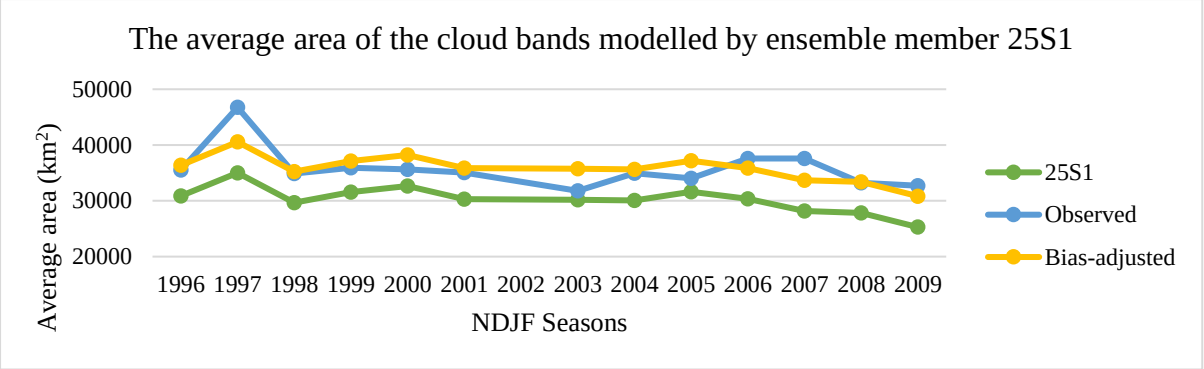

Figure A 10: The average area of the cloud bands for ensemble member 25S1.

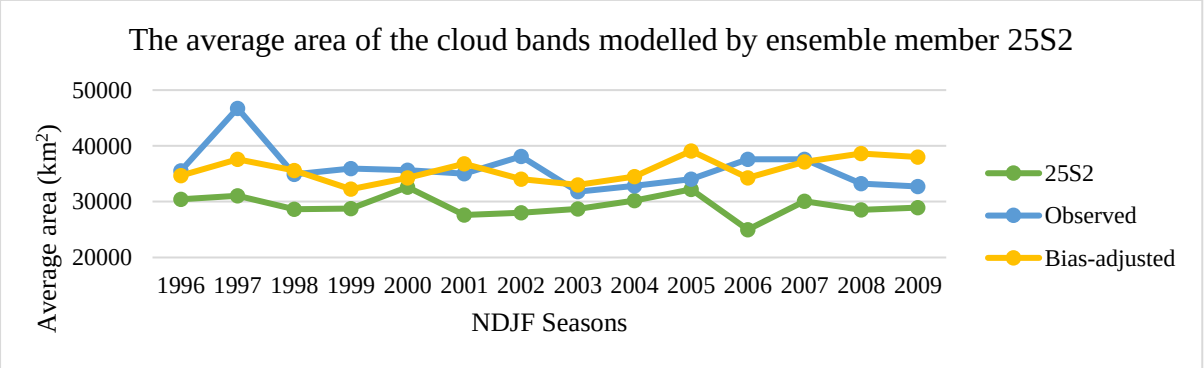

Figure A 11: The average area of the cloud bands for ensemble member 25S2.

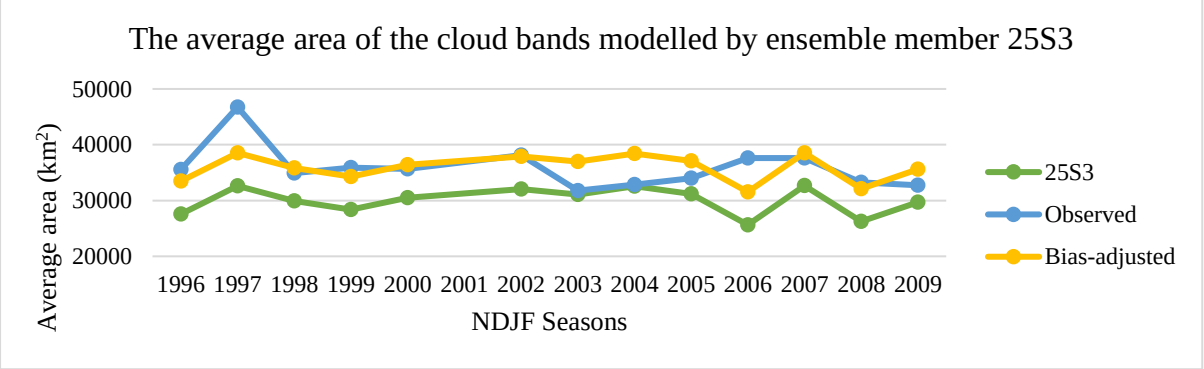

Figure A 12: The average area of the cloud bands for ensemble member 25S3.

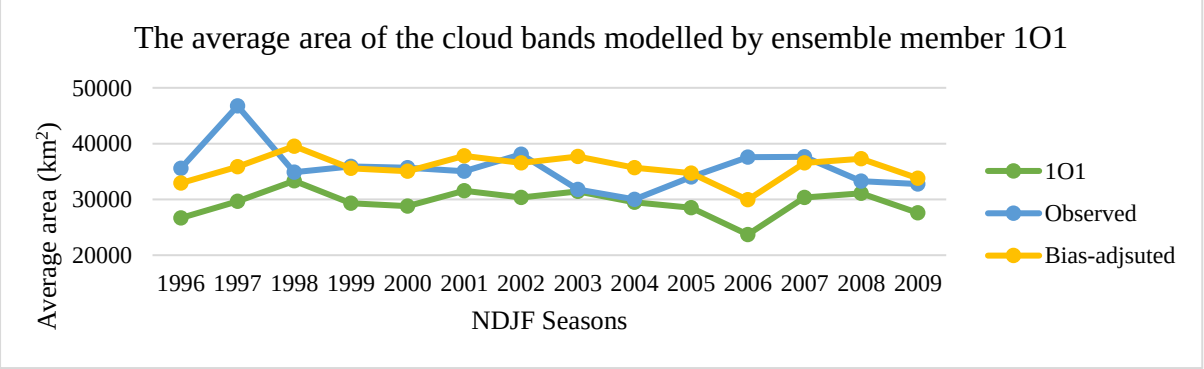

Figure A 13: The average area of the cloud bands for ensemble member 1O1.

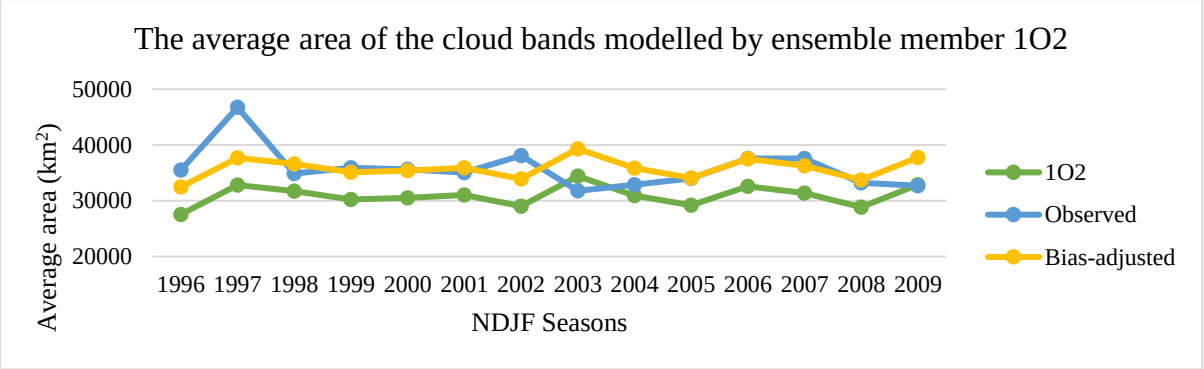

Figure A 14: The average area of the cloud bands for ensemble member 1O2.

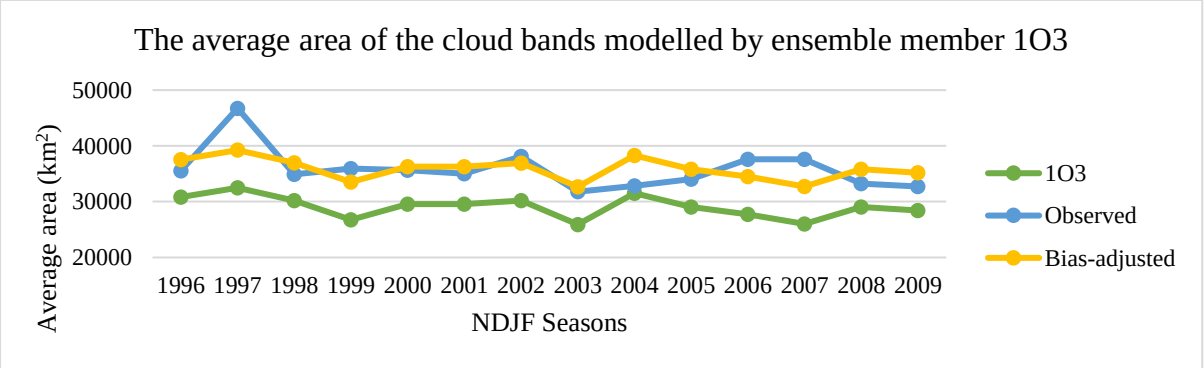

Figure A 15: The average area of the cloud bands for ensemble member 1O3.

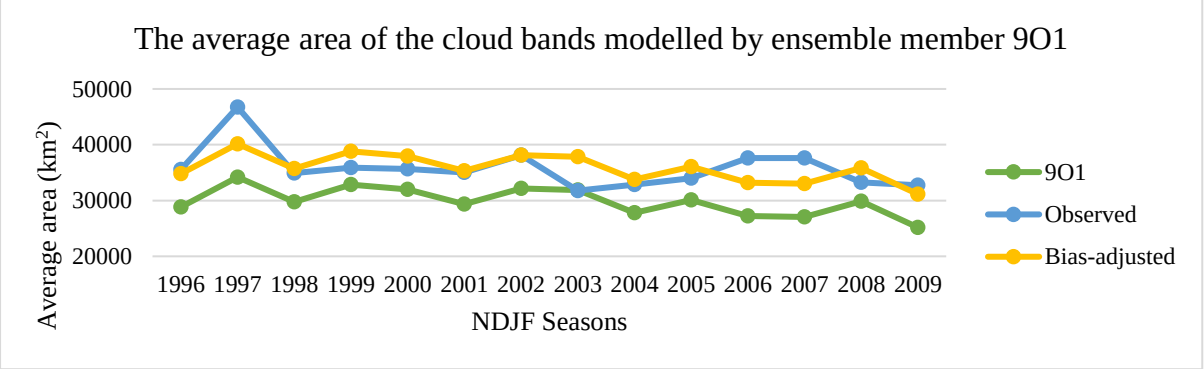

Figure A 16: The average area of the cloud bands for ensemble member 9O1.

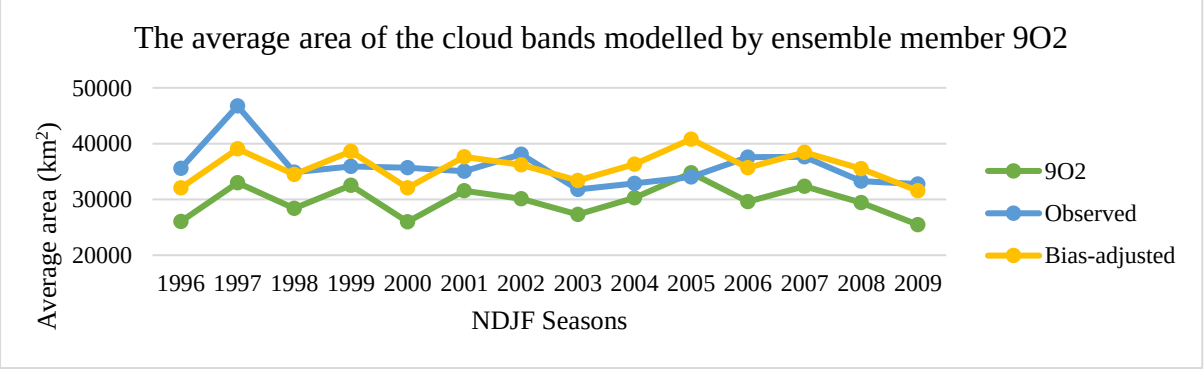

Figure A 17: The average area of the cloud bands for ensemble member 9O2.

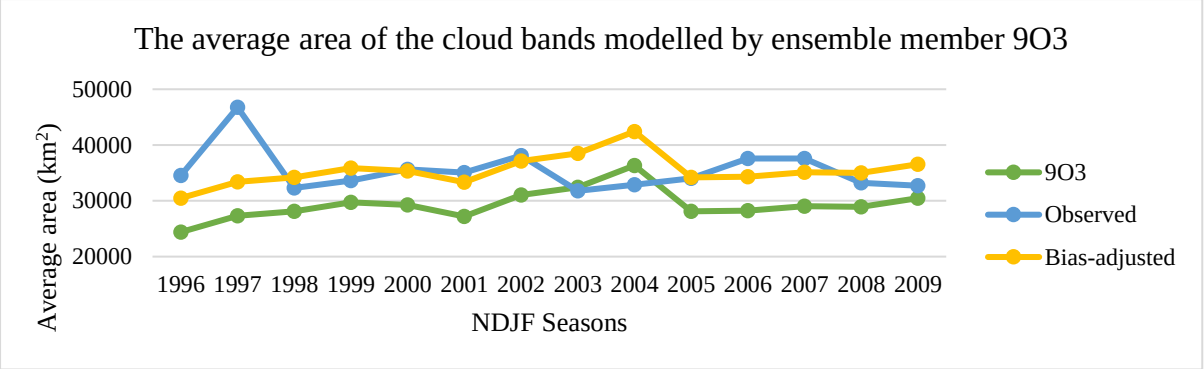

Figure A 18: The average area of the cloud bands for ensemble member 9O3.

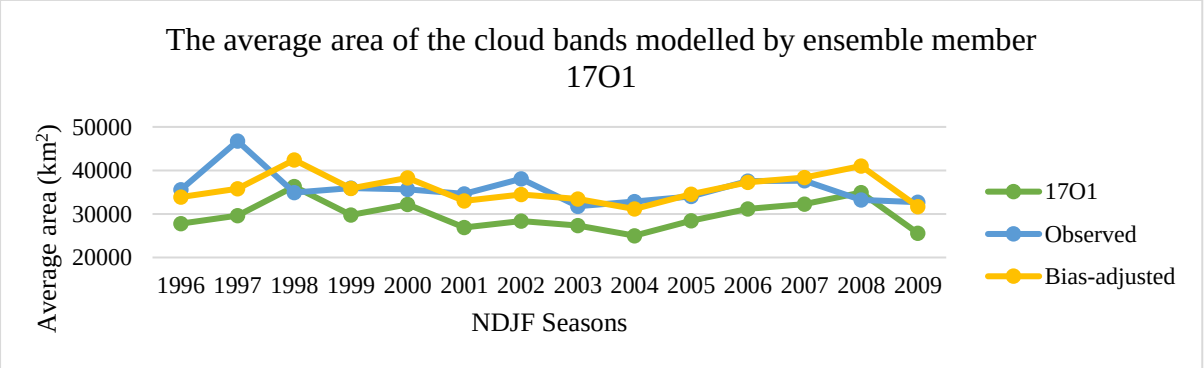

Figure A 19: The average area of the cloud bands for ensemble member 17O1.

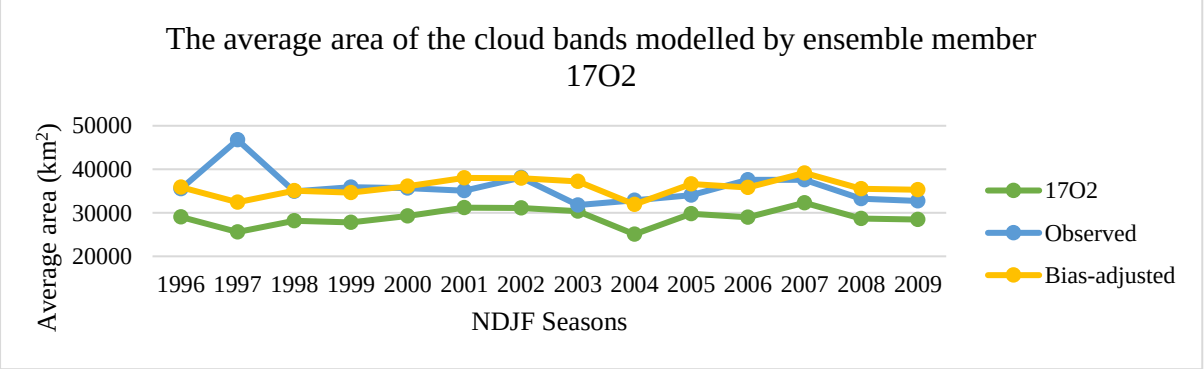

Figure A 20: The average area of the cloud bands for ensemble member 17O2.

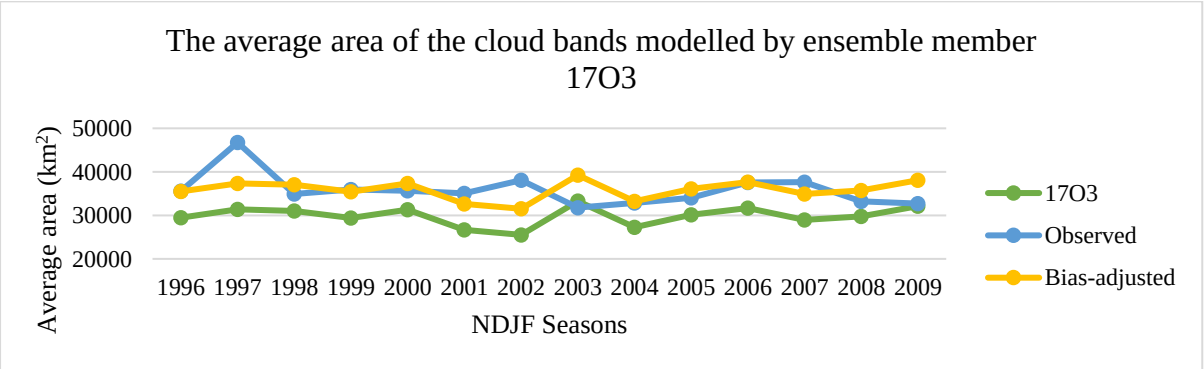

Figure A 21: The average area of the cloud bands for ensemble member 17O3.

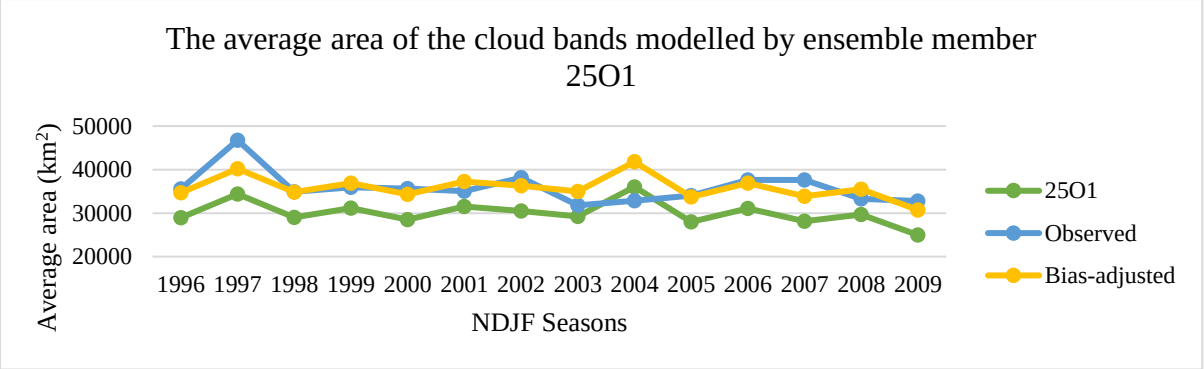

Figure A 22: The average area of the cloud bands for ensemble member 25O1.

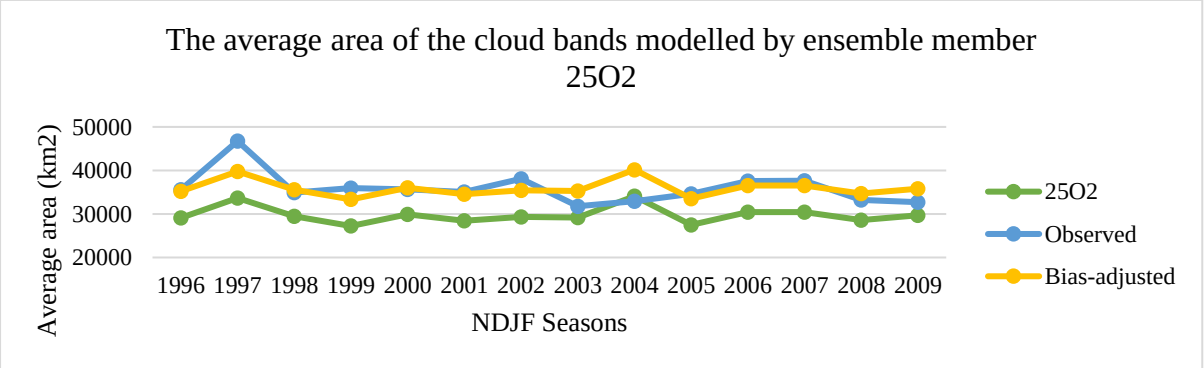

Figure A 23: The average area of the cloud bands for ensemble member 25O2.

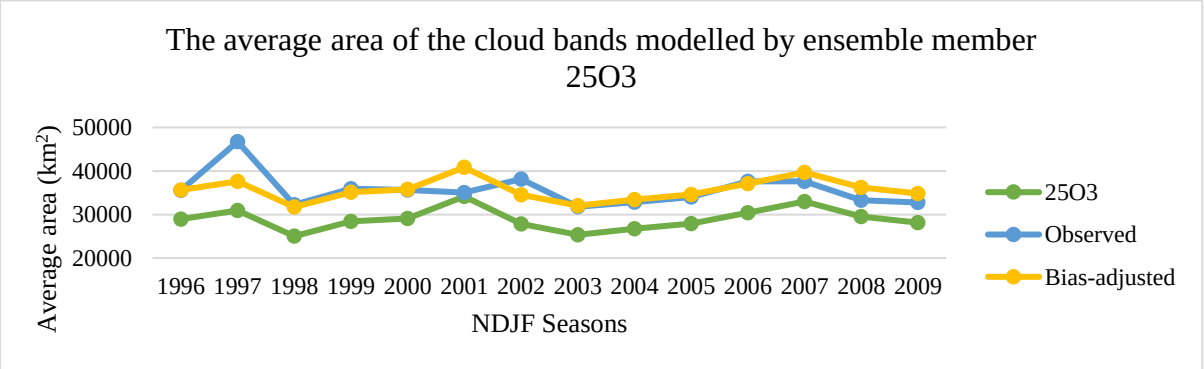

Figure A 24: The average area of the cloud bands for ensemble member 25O3.

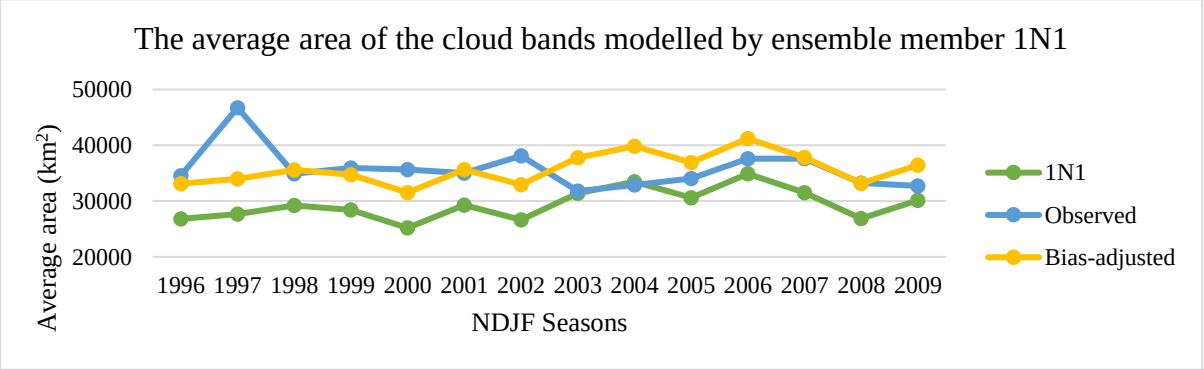

Figure A 25: The average area of the cloud bands for ensemble member 1N1.

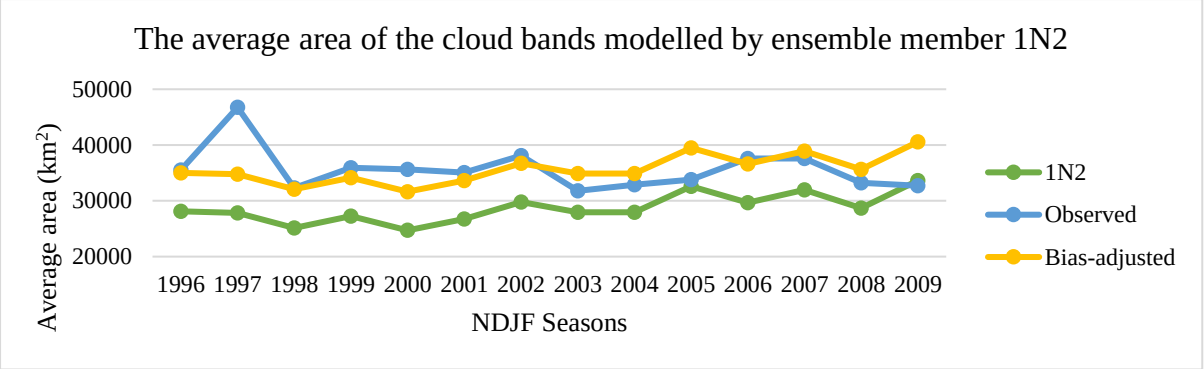

Figure A 26: The average area of the cloud bands for ensemble member 1N2.

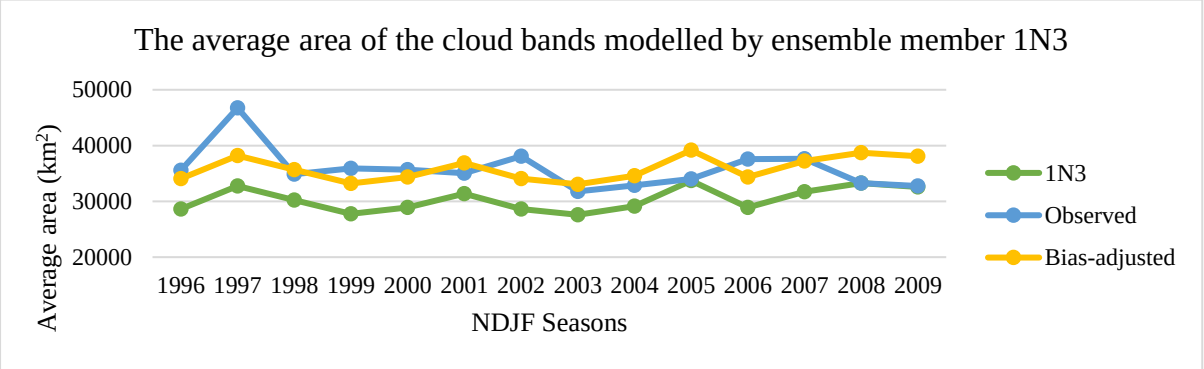

Figure A 27: The average area of the cloud bands for ensemble member 1N3.

APPENDIX B: Anchor points and centroids of the cloud bands

This appendix consists of the combined graphs with the anchor points and the centroids of all the cloud bands modelled by the 27 different ensemble members for the study period November, December, January and February of the years 1996/1997 to 2009/2010. In the figures below the red dots indicate the anchor points and the green dots the centroids. The blue lines divide the geographical domain in the three preferred regions where TTTs tend to develop, i.e. have their anchor points. At the bottom of these three regions (columns), the number of cloud bands, which developed within that region, is displayed (around 35˚S).

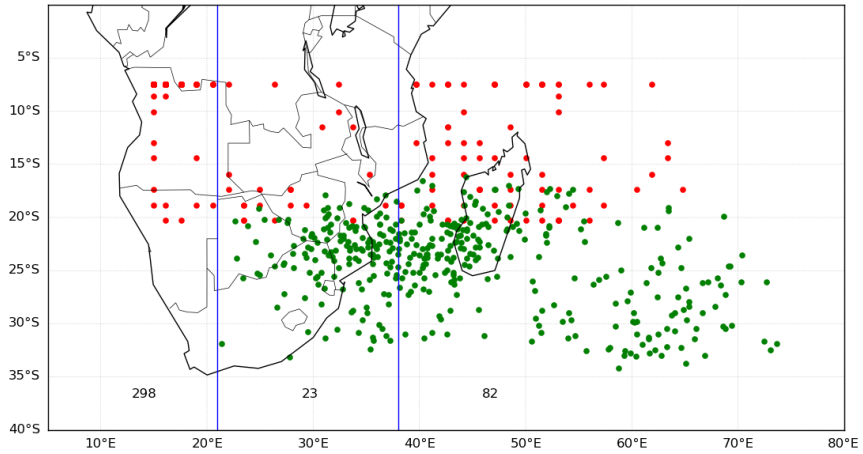

Figure B 1: The anchor points (red dots) and the position of the centroids (green dots) of the cloud bands modelled by ensemble member 1 initiated on 1 September.

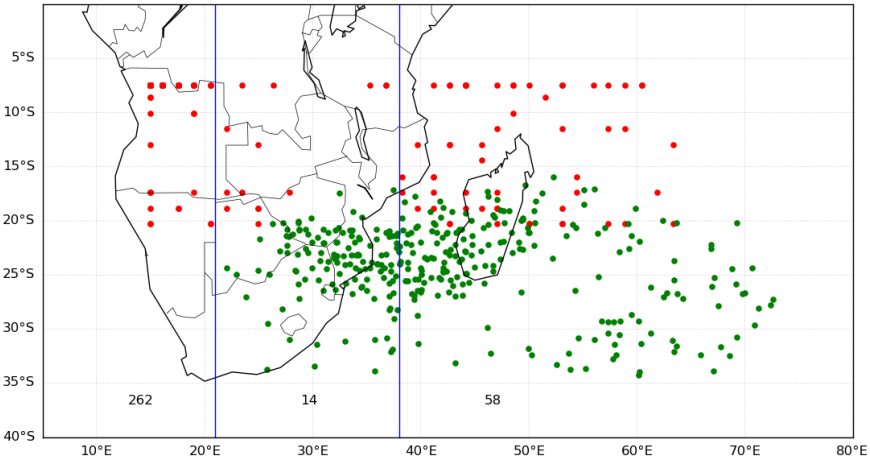

Figure B 2: The anchor points (red dots) and the position of the centroids (green dots) of the cloud bands modelled by ensemble member 2 initiated on 1 September.

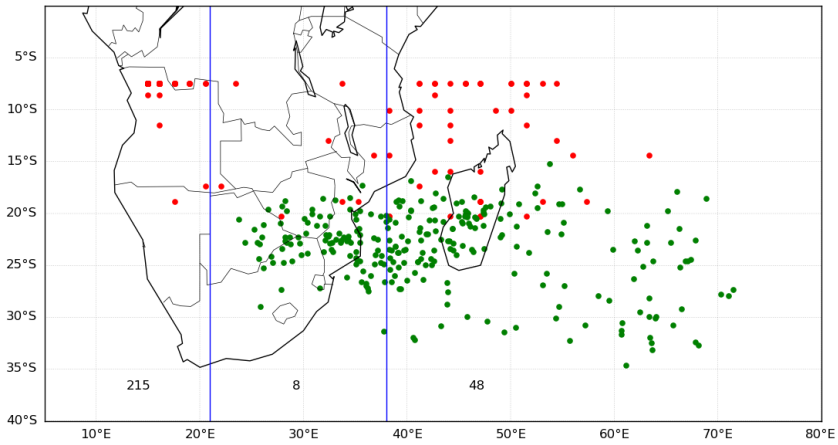

Figure B 3: The anchor points (red dots) and the position of the centroids (green dots) of the cloud bands modelled by ensemble member 3 initiated on 1 September.

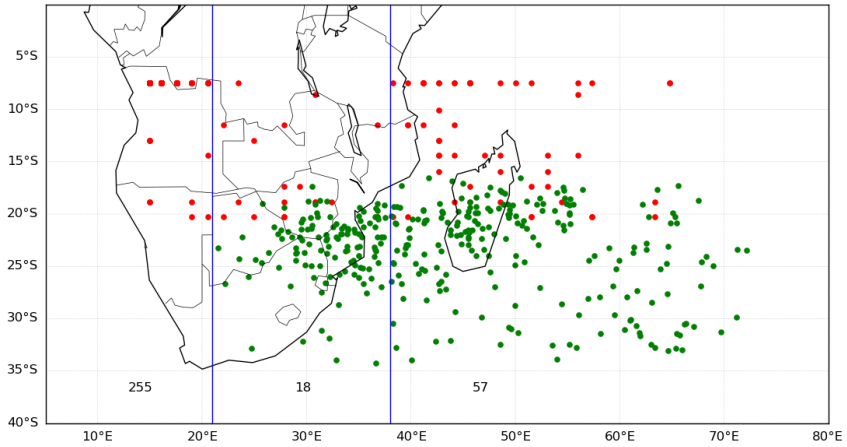

Figure B 4: The anchor points (red dots) and the position of the centroids (green dots) of the cloud bands modelled by ensemble member 1 initiated on 9 September.

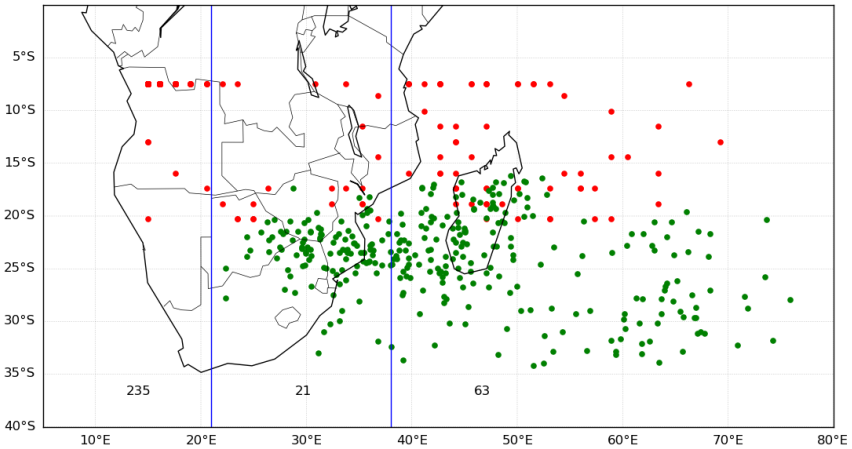

Figure B 5: The anchor points (red dots) and the position of the centroids (green dots) of the cloud bands modelled by ensemble member 2 initiated on 9 September.

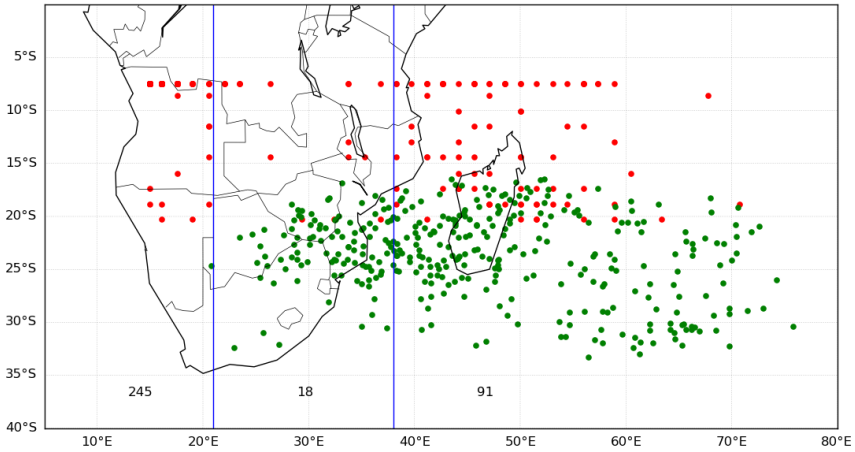

Figure B 6: The anchor points (red dots) and the position of the centroids (green dots) of the cloud bands modelled by ensemble member 3 initiated on 9 September.

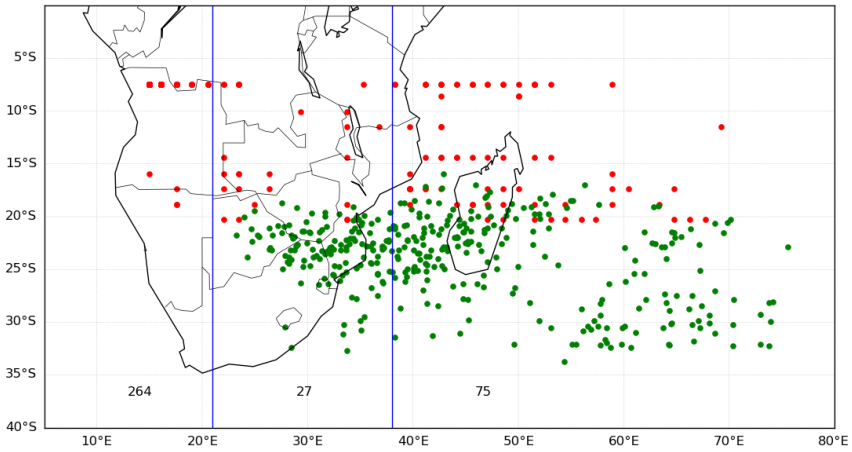

Figure B 7: The anchor points (red dots) and the position of the centroids (green dots) of the cloud bands modelled by ensemble member 1 initiated on 17 September.

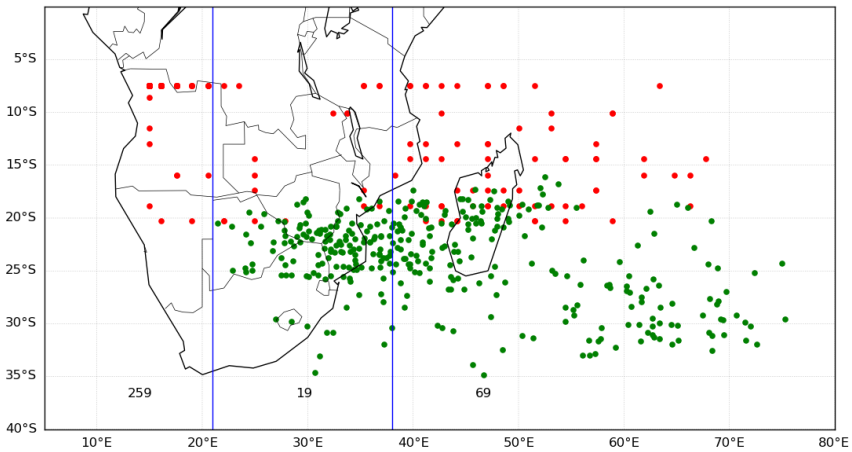

Figure B 8: The anchor points (red dots) and the position of the centroids (green dots) of the cloud bands modelled by ensemble member 2 initiated on 17 September.

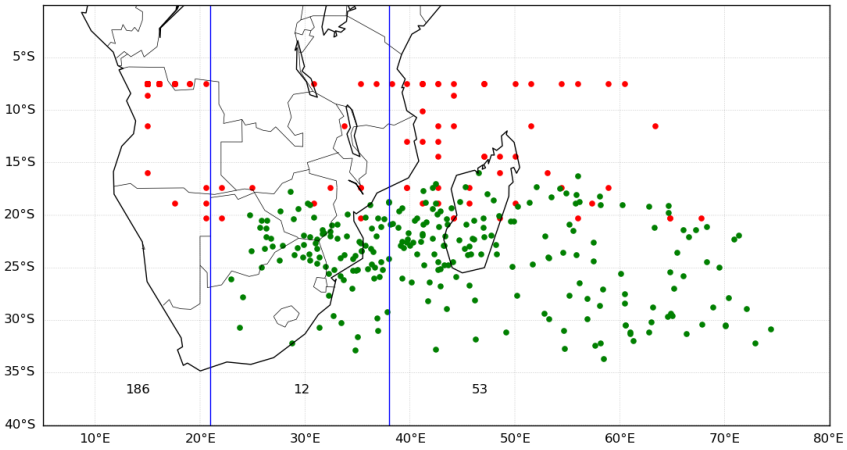

Figure B 9: The anchor points (red dots) and the position of the centroids (green dots) of the cloud bands modelled by ensemble member 3 initiated on 17 September.

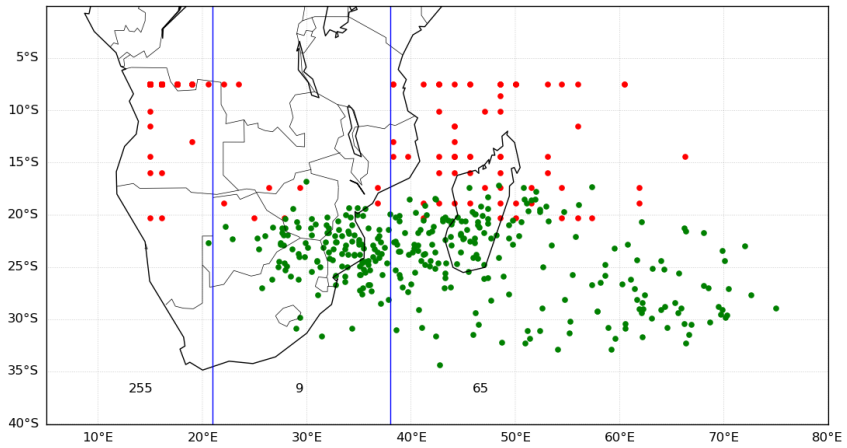

Figure B 10: The anchor points (red dots) and the position of the centroids (green dots) of the cloud bands modelled by ensemble member 1 initiated on 25 September.

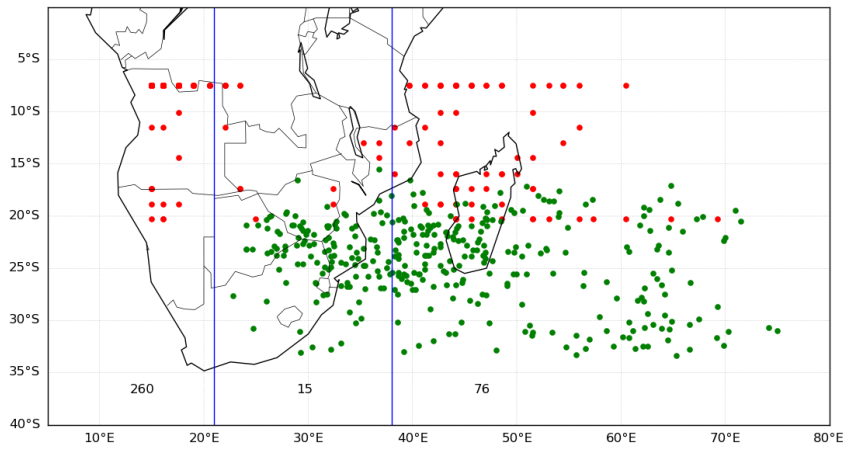

Figure B 11: The anchor points (red dots) and the position of the centroids (green dots) of the cloud bands modelled by ensemble member 2 initiated on 25 September.

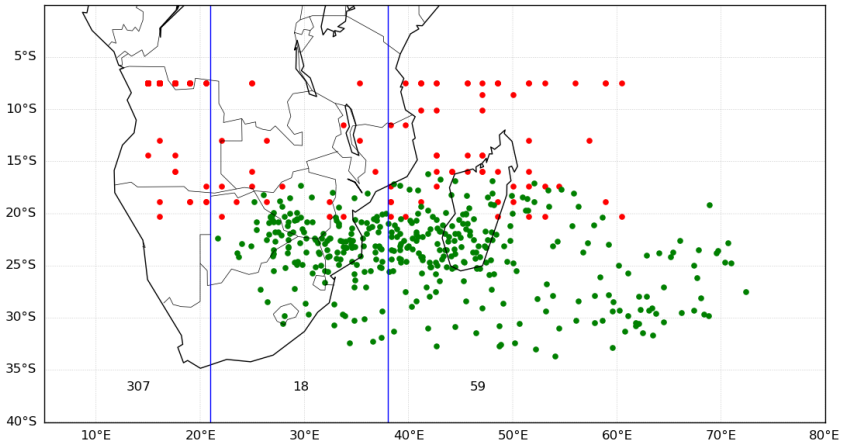

Figure B 12: The anchor points (red dots) and the position of the centroids (green dots) of the cloud bands modelled by ensemble member 3 initiated on 25 September.

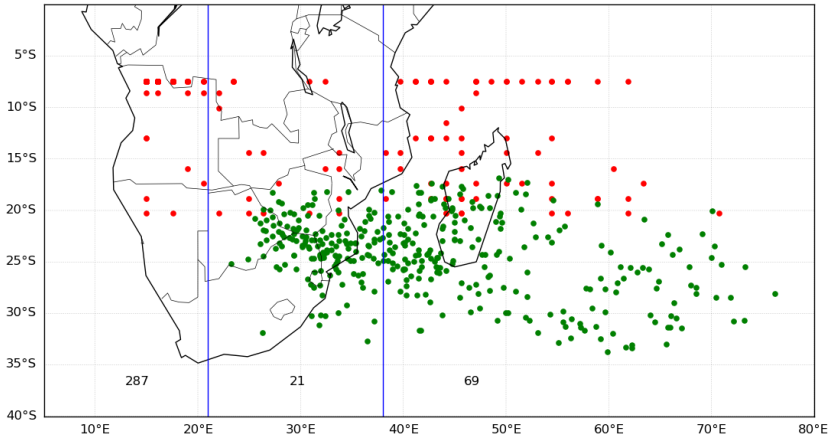

Figure B 13: The anchor points (red dots) and the position of the centroids (green dots) of the cloud bands modelled by ensemble member 1 initiated on 1 October.

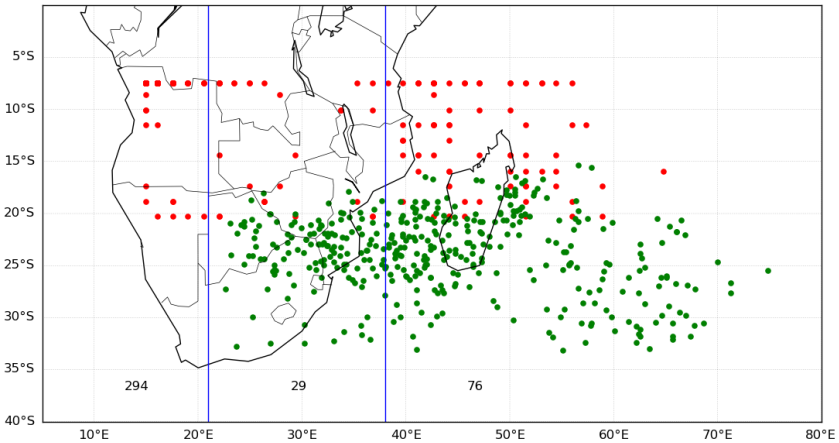

Figure B 14: The anchor points (red dots) and the position of the centroids (green dots) of the cloud bands modelled by ensemble member 2 initiated on 1 October.

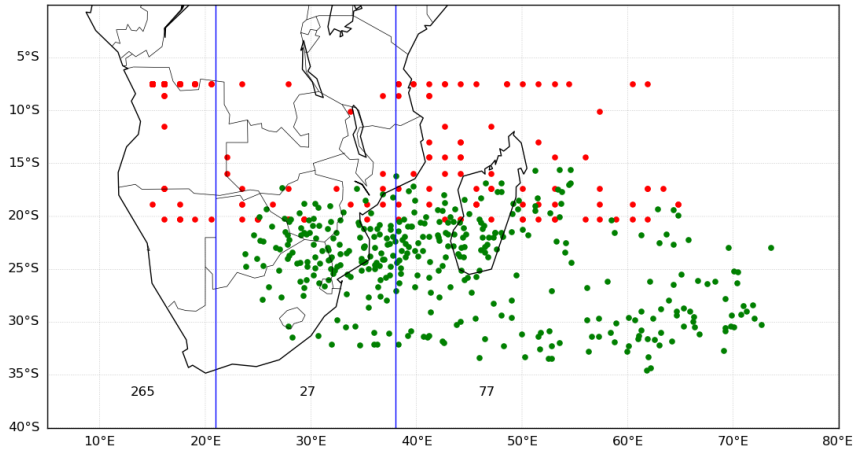

Figure B 15: The anchor points (red dots) and the position of the centroids (green dots) of the cloud bands modelled by ensemble member 3 initiated on 1 October.

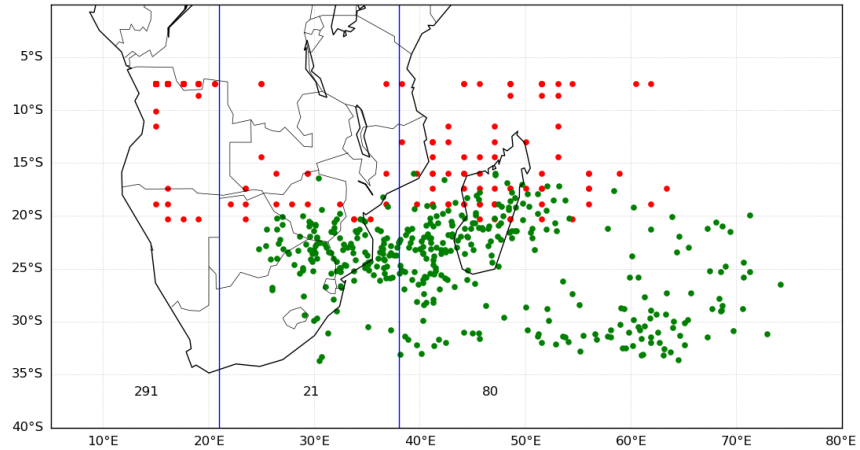

Figure B 16: The anchor points (red dots) and the position of the centroids (green dots) of the cloud bands modelled by ensemble member 1 initiated on 9 October.

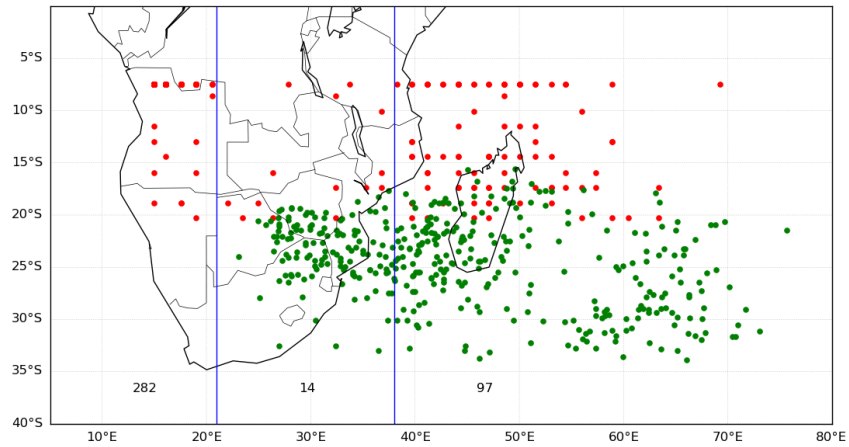

Figure B 17: The anchor points (red dots) and the position of the centroids (green dots) of the cloud bands modelled by ensemble member 2 initiated on 9 October.

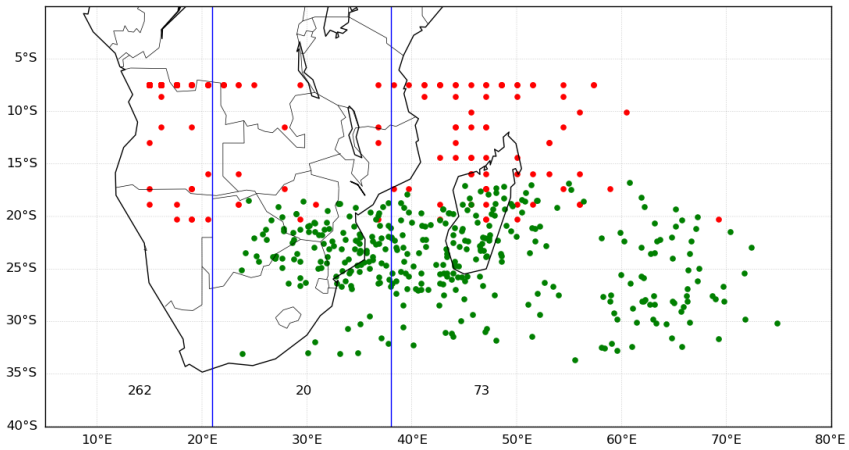

Figure B 18: The anchor points (red dots) and the position of the centroids (green dots) of the cloud bands modelled by ensemble member 3 initiated on 9 October.

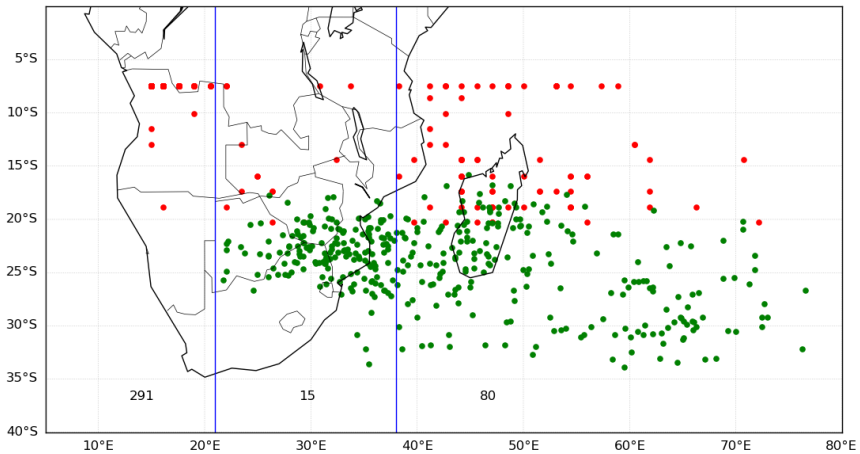

Figure B 19: The anchor points (red dots) and the position of the centroids (green dots) of the cloud bands modelled by ensemble member 1 initiated on 17 October.

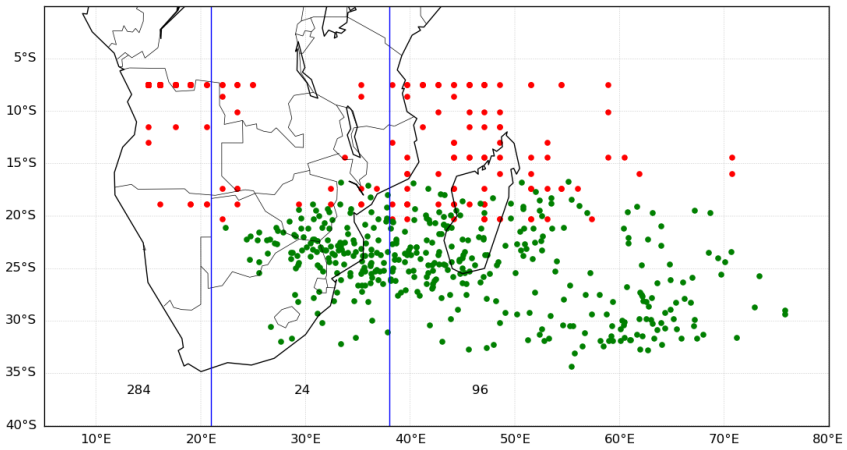

Figure B 20: The anchor points (red dots) and the position of the centroids (green dots) of the cloud bands modelled by ensemble member 2 initiated on 17 October.

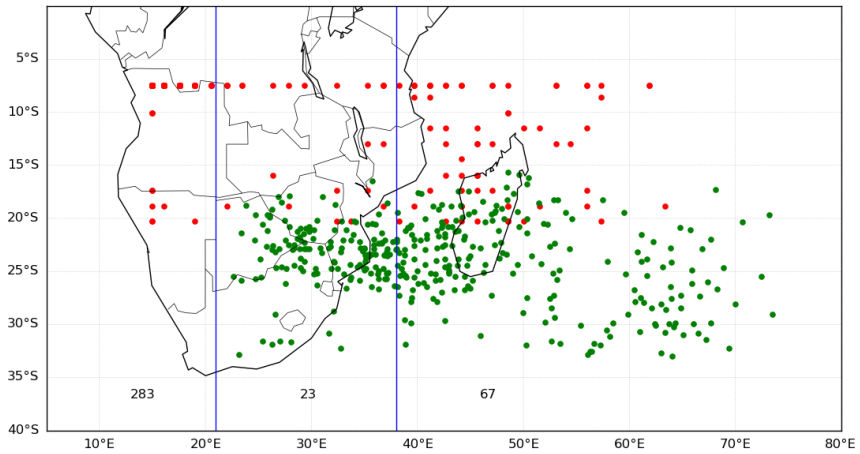

Figure B 21: The anchor points (red dots) and the position of the centroids (green dots) of the cloud bands modelled by ensemble member 3 initiated on 17 October.

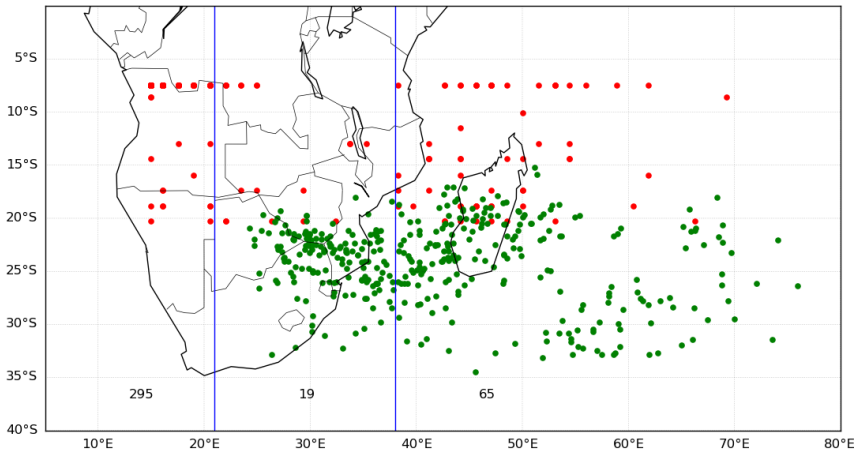

Figure B 22: The anchor points (red dots) and the position of the centroids (green dots) of the cloud bands modelled by ensemble member 1 initiated on 25 October.

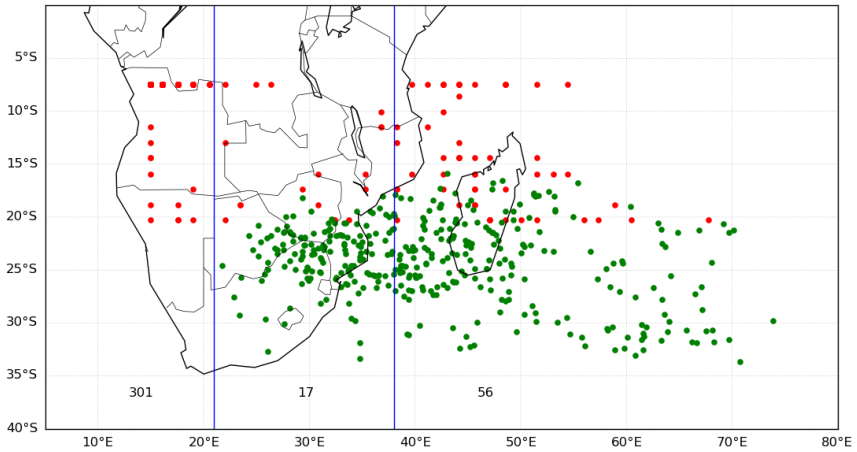

Figure B 23: The anchor points (red dots) and the position of the centroids (green dots) of the cloud bands modelled by ensemble member 2 initiated on 25 October.

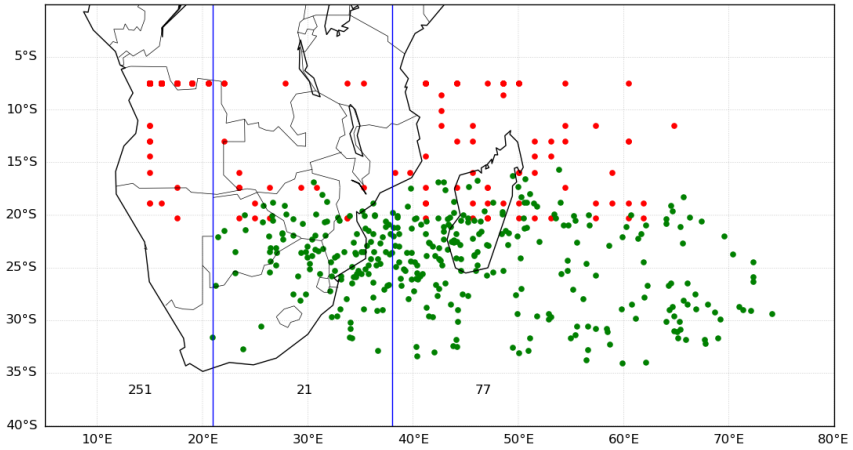

Figure B 24: The anchor points (red dots) and the position of the centroids (green dots) of the cloud bands modelled by ensemble member 3 initiated on 25 October.

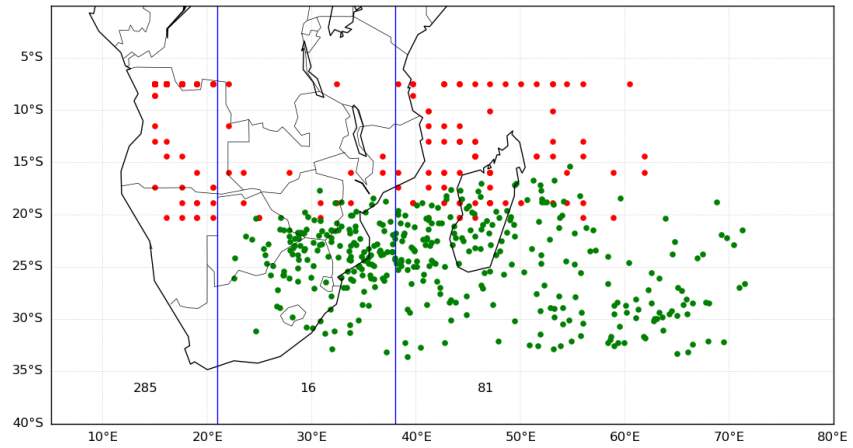

Figure B 25: The anchor points (red dots) and the position of the centroids (green dots) of the cloud bands modelled by ensemble member 1 initiated on 1 November.

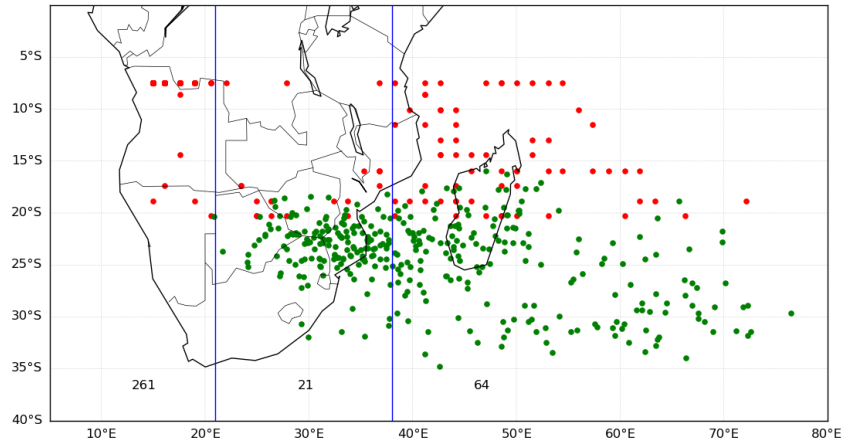

Figure B 26: The anchor points (red dots) and the position of the centroids (green dots) of the cloud bands modelled by ensemble member 2 initiated on 1 November.

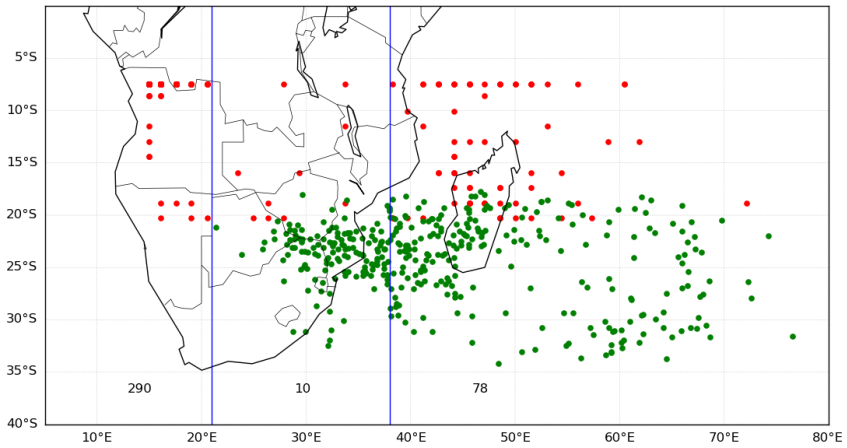

Figure B 27: The anchor points (red dots) and the position of the centroids (green dots) of the cloud bands modelled by ensemble member 3 initiated on 1 November.